PRODUCTION OF TI-6AL-4V ALLOY BY 3D ELECTRON BEAM MELTING
TECHNIQUE AND DEVELOPMENT OF ITS POST TREATMENTS

A THESIS SUBMITTED TO
THE GRADUATE SCHOOL OF NATURAL AND APPLIED SCIENCES
OF
MIDDLE EAST TECHNICAL UNIVERSITY

BY

MERVE NUR DOĞU

IN PARTIAL FULFILLMENT OF THE REQUIREMENTS
FOR
THE DEGREE OF MASTER OF SCIENCE
IN
METALLURGICAL AND MATERIALS ENGINEERING

SEPTEMBER 2019

Approval of the thesis:

PRODUCTION OF TI-6AL-4V ALLOY BY 3D ELECTRON BEAM MELTING TECHNIQUE AND DEVELOPMENT OF ITS POST TREATMENTS

submitted by **MERVE NUR DOĞU** in partial fulfillment of the requirements for the degree of **Master of Science in Metallurgical and Materials Engineering Department, Middle East Technical University** by,

Prof. Dr. Halil Kalıpçılar
Dean, Graduate School of **Natural and Applied Sciences**   _____

Prof. Dr. C. Hakan Gür
Head of Department, **Met. and Mat. Eng.**   _____

Prof. Dr. Arcan Fehmi Dericioğlu
Supervisor, **Met. and Mat. Eng., METU**   _____

Assoc. Prof. Dr. Ziya Esen
Co-Supervisor, **Materials Science and Engineering, Çankaya University**   _____

Examining Committee Members:

Prof. Dr. Kadri Aydınol
Metallurgical and Materials Engineering, METU   _____

Prof. Dr. Arcan Fehmi Dericioğlu
Met. and Mat. Eng., METU   _____

Prof. Dr. Caner Durucan
Metallurgical and Materials Engineering, METU   _____

Prof. Dr. Emrah Ünalan
Metallurgical and Materials Engineering, METU   _____

Assist. Prof. Dr. Kemal Davut
Metallurgical and Materials Engineering, Atılım University   _____

Date: 03.09.2019

I hereby declare that all information in this document has been obtained and presented in accordance with academic rules and ethical conduct. I also declare that, as required by these rules and conduct, I have fully cited and referenced all material and results that are not original to this work.

Name, Surname: Merve Nur Doğu

Signature:

ABSTRACT

PRODUCTION OF TI-6AL-4V ALLOY BY 3D ELECTRON BEAM MELTING TECHNIQUE AND DEVELOPMENT OF ITS POST TREATMENTS

Doğu, Merve Nur
Master of Science, Metallurgical and Materials Engineering
Supervisor: Prof. Dr. Arcan Fehmi Dericioğlu
Co-Supervisor: Assoc. Prof. Dr. Ziya Esen

September 2019, 142 pages

In this thesis, the effects of production variables in electron beam melting (EBM) and post-processing on the materials' and mechanical properties of Ti-6Al-4V alloy were investigated by considering the microstructural change. Ti-alloy samples were produced at 0°, 45° and 90° with respect to building plate. Surface polishing with HF solution was applied to reduce the surface roughness. On the other hand, post-heat treatments, namely, 2-step thermo-hydrogen processing (THP) and annealing, were conducted to improve the mechanical properties, i.e. hardness and tensile strength, and to increase fatigue life. Production at different angles had no influence on texture formation such that in all samples the texture of α-phase was commonly concentrated in $(10\bar{1}0)$ plane, which was parallel to building direction. The samples produced at 0° had the coarsest and lowest microstructure and hardness value, respectively, possibly due to higher heat input during production; however, they possessed comparatively higher density and lower surface roughness. Therefore, the samples displayed high tensile strength and ductility comparable to standards. Likewise, fatigue life improved by production at 0° due to lower surface roughness and defects. THP refined the microstructure and slightly increased the hardness by altering the texture. Although tensile strength increased, ductility reduced possibly due to oxidation. Annealing

coarsened the microstructure and degraded the mechanical properties. On the other hand, both post heat treatment processes did not influence the fatigue life due to predominant effect of high surface roughness. Despite the reduced surface roughness by surface polishing, fatigue life decreased because of dissolved hydrogen in samples.

Keywords: Ti-6Al-4V Alloy, Additive Manufacturing, Electron Beam Melting, Thermo-hydrogen Processing, Texture

ÖZ

Tİ-6AL-4V ALAŞIMININ 3 BOYUTLU ELEKTRON DEMETİ ERGİTME YÖNTEMİYLE ÜRETİLMESİ VE İKİNCİL İŞLEMLERİN GELİŞTİRİLMESİ

Doğu, Merve Nur
Yüksek Lisans, Metalurji ve Malzeme Mühendisliği
Tez Danışmanı: Prof. Dr. Arcan Fehmi Dericioğlu
Ortak Tez Danışmanı: Doç. Dr. Ziya Esen

Eylül 2019, 142 sayfa

Bu tezde, elektron demeti ergitme (EDE) yönteminde üretim değişkenlerinin ve ikincil işlemlerin Ti-6Al-4V alaşımının malzeme ve mekanik özelliklerine etkisi içyapı değişimleri gözetilerek incelenmiştir. Ti-alaşım numuneleri üretim tablosuna göre 0°, 45° and 90° açılarda üretilmiştir. Yüzey pürüzlülüğünü azaltmak için alaşımlara HF çözeltisi ile yüzey parlatma işlemi uygulanmıştır. Diğer yandan, sertlik ve çekme dayancı gibi mekanik özellikleri geliştirmek ve yorulma ömrünü arttırmak için 2-basamaklı termo-hidrojenleme prosesi (THP) ile tavlama işlemi ikincil ısıl işlem olarak uygulanmıştır. Farklı açılarda üretimin doku oluşumuna bir etkisi olmamış ve tüm numunelerde α fazı dokulanması üretim yönüne paralel olan $(10\bar{1}0)$ düzleminde yoğunlaşmıştır. 0°'lik açı ile üretilen numunelerde, muhtemelen üretim sırasında yüksek ısı girdisi nedeniyle en kaba içyapı ve en düşük sertlik değerleri bulunmasına karşın numunelerin yüksek yoğunluğa ve düşük yüzey pürüzlülüğüne sahip oldukları görülmüştür. Bu yüzden, numuneler standartlarla karşılaştırabilecek çekme dayancı ve süneklik değerleri göstermişlerdir. Ayrıca, 0° açı ile üretilen numunelerin düşük yüzey pürüzlülüğüne ve hata miktarına sahip olmaları nedeniyle numunelerin yorulma ömrü artmıştır. THP işlemi numunelerde dokulanma yapısını değiştirerek içyapıyı inceltmiş ve sertliği arttırmıştır. Çekme dayancı artmasına rağmen muhtemel

oksitlenme yüzünden süneklik aynı numunelerde düşmüştür. Tavlama ise içyapıyı kabalaştırmış ve mekanik özellikleri kötüleştirmiştir. Diğer yandan, yüksek yüzey pürüzlülüğünün baskın etkisi yüzünden ikincil ısıl işlemlerin yorulma ömrü üzerinde bir etkisi olmamıştır. Yüzey pürüzlülüğü yüzey parlatma işlemi ile azalmasına rağmen, yorulma ömrü numunelerde çözünen hidrojen nedeniyle düşmüştür.

Anahtar Kelimeler: Ti-6Al-4V alaşımı, Katmanlı İmalat, Elektron Demeti Ergitme, Termo-hidrojenleme prosesi, Dokulanma

To My Beloved Family

ACKNOWLEDGEMENTS

TABLE OF CONTENTS

LIST OF TABLES

TABLES

LIST OF FIGURES

FIGURES

CHAPTER 1

INTRODUCTION

Ti-6Al-4V alloy (in the class of α+β alloys) has been extensively used for the aerospace, defense, automotive, petro-chemical, biomedical, architecture, and sports industries due its high specific strength (especially for higher temperatures), excellent corrosion resistance, comparatively high temperature resistance, high cycle fatigue strength and low density. Ti-6Al-4V is one of the most preferred alloy in the aerospace industry such as gas turbine engines and helicopters, where weight reduction is crucial. Additionally, Ti-6Al-4V alloy has been also utilized in the biomedical industry as bio-inert materials in hip and knee joints, and dental implants due to its high corrosion resistance, biocompatibility, bio-adhesion (osseointegration), processability, availability (relatively low prices) and suitable mechanical properties (e.g. similar Young's Modulus with bone).

In order to manufacture Ti-6Al-4V alloy parts in any industry, more than one type conventional fabrication techniques such as powder metallurgy, casting, welding/joining, machining, etc. are generally used together to produce only one part although they are suitable for continuous production. Additionally, fabrication of very complex geometries is not possible with conventional fabrication techniques. Moreover, if thousands of samples are not produced at a time and design of parts changes constantly, they do not become cost effective. In contrast to conventional fabrication techniques, additive manufacturing (AM) techniques make possible fabrication of parts with complex geometries in one step by eliminating excess raw material usage and providing energy and time savings for limited number of Ti-6Al-4V alloy parts production. AM techniques are divided mainly into groups depending on the feeding of raw materials, namely, powder bed fusion (PBF) and directed energy deposition (DED).

1

Among the PBF techniques, selective laser sintering (SLS), selective laser melting (SLM) and electron beam melting (EBM) are some of the common methods used for Ti-alloys part production. Although the surface finish of SLM produced samples are better, high residual stress and martensitic microstructure formed due to rapid cooling are the drawbacks of the technique. On the other hand, SLS technique is suitable for porous material production. EBM technique, created by ARCAM AB (Sweden), is capable of producing complex geometries with relative densities over 99% and with comparatively lower residual stresses due to higher energy input and slow cooling rate. However, surfaces having high roughness should be treated to improve mechanical properties of the parts.

Nowadays, EBM is widely used to fabricate complicated Ti-6Al-4V alloy parts. During the production with EBM, Ti-6Al-4V alloy parts are produced layer by layer by feeding micron-sized Ti-6Al-4V alloy powders on building stage and melting them by electron beam using high vacuum (around 10^{-4} torr). Application of pre-heating during the production eliminates high residual stresses and prevent martensitic phase formation due to slow cooling of the components down to pre-heating temperature, which is above martensitic start temperature. Therefore, EBM produced Ti-6Al-4V parts' microstructure consists of α plates and small amount of β inside Widmanstätten structure grown along the build direction. In addition, comparatively denser parts can be produced via optimizing process parameters such as layer thickness, e-beam current, line offset, focus offset, and line energy.

Although EBM technique has many advantages, the high surface roughness due to partially melted powders on the surfaces, internal stresses developed during the production due to temperature gradient, presence of defects (e.g. lack of fusion of layers, porosity, delamination and balling) after the production are common drawbacks of the technique. Moreover, building direction of the part may cause anisotropic mechanical properties and the density may be different depending on its place and position on production plate.

Additionally, some of Al and V elements within Ti-6Al-4V alloy may be lost during production due to high vacuum in production chamber. Therefore, reused powder (with low Al and V content) should be mixed with virgin powder before each production step. All of these drawbacks cause deterioration of mechanical properties of Ti-6Al-4V alloy parts produced by EBM. Accordingly, processing parameters need to be optimized and post processes should be applied to increase parts' density, refine its microstructure and reduce surface roughness at least.

In Ti-6Al-4V alloys, which are produced conventional techniques, in order to enhance mechanical properties, the alloy is plastically deformed above the recrystallization temperature for grain refinement by dynamic recovery and recrystallization. However, dynamic recovery and recrystallization is not suitable for EBM produced parts since the part cannot preserve its geometry due to hot working. Therefore, there are several post-processing techniques applied to EBM samples. For example, high surface roughness can be improved by machining, blasting (i.e. with Al_2O_3), milling, chemical polishing. On the other hand, for removal of residual stress, various heat treatments such as conventional annealing and hot isostatic pressing (HIP) which is conducted to decrease porosity and to obtain parts with 100% relative density are applied. However, conventional annealing treatment reduces the strength of the alloy although it increases the ductility. Although it is not possible to refine the grain structure by heat treatment, it is possible to obtain finer microstructures. In this thesis, thermo-hydrogen processing (THP), which enables refinement of the microstructure in powder metallurgy and cast titanium and titanium alloys produced by conventional methods without use of deformation, was used to Ti-6Al-4V alloy parts produced by EBM. The purpose of THP is to enhance the mechanical properties of EBM produced Ti-6Al-4V alloy by refining the microstructure without deformation, which causes dimensional and shape changes. THP is based on alloying and dealloying of titanium and titanium alloys with hydrogen. Hydrogen having high diffusivity in titanium can be taken away easily by vacuum annealing (reversible reaction) thanks to positive enthalpy of solution in titanium.

Microstructural refinement in THP depends on phase transformation during alloying and dealloying with hydrogen. An EBM produced Ti-6Al-4V alloy is consisted of lamellar structure containing α and β phases. During alloying with hydrogen, when solubility limits of α and β is exceeded new δ (TiH_2)-phase forms along the interface region of α and β-phases. During dealloying, excess hydrogen is removed from α and β-phases and δ-phase is transformed to fine α by preserving its phase boundary.

Therefore, THP is an alternative post heat treatment process to enhance mechanical properties (increasing strength without reducing the ductility too much) because it refines the microstructure and the alloy shape is preserved since the process includes no plastic deformation. Hydrogen which is a unique alloying interstitial element for titanium and titanium alloys stabilizes the β phase (more ductile high-temperature bcc phase) and destabilizes the α phase (low-temperature hcp phase), and hence increases the α+β phase range. Therefore, the β-transus temperature and martensite transformation temperatures reduces by hydrogen alloying. For example, 39 at. % hydrogen reduces the β-transus temperature from 882 °C to 300 °C for pure titanium. Accordingly, heat treatment around β-phase region can be conducted at lower temperatures. Also, diffusion coefficients of the alloying elements in the β phase are reduced with hydrogen addition, thereby causing slower transformation from β to α. Recently, THP was performed to Ti-6Al-4V alloy produced by selective laser melting (SLM). To the best of author's knowledge, 2-step THP (alloying and dealloying under β-transus temperature) has not been applied for Ti-6Al-4V alloy parts produced by EBM. Accordingly, in this thesis, 2-step THP process will be applied to EBM produced parts for improving mechanical properties (hardness, tensile and fatigue properties) by refining the microstructure at relatively lower temperatures. Determination of the success of THP process by comparison the mechanical results obtained from conventional annealing treatment is another target of the study. As a post-processing technique, the effect of surface chemical polishing on surface roughness and mechanical properties was also studied.

Moreover, parts manufactured at different building angles, i.e. 0º, 45º and 90º, were also examined microstructurally and tested mechanically to reveal texture formation and differences in microstructures, and tensile and fatigue properties.

In this thesis, the topics covered in the study are given into five main chapters. Chapter 2 involves the literature review, which gives detailed information about titanium and its alloys, i.e. application areas, chemical compositions, types of heat treatments applied and microstructure-mechanical property relations. AM techniques and post processes applied to AM parts are also presented in this chapter. Chapter 3 covers the experimental procedure used for production of EBM Ti-6Al-4V alloy parts, their post-processing and testing. Experimental results about structural, microstructural and mechanical tests and discussions on each result are given in Chapter 4. Finally, Chapter 5 presents the important conclusions drawn at the end if study. Future works, which are thought to be helpful in other works and thesis that will be conducted on similar subject, are added to end of the thesis as well.

CHAPTER 2

LITERATURE REVIEW

2.1. General Information

Titanium was explored as an unknown metallic element by William Gregor in 1791, and Martin Heinrich Klappoth entitled it as "Titanium" in 1795. Wilhelm Justin Kroll developed commercial process, today known as "Kroll Process" for production of titanium in 1932. Titanium can be classified as nonferrous and the heaviest light metal due to its density (4.51 g/cm^3) shown in Figure 2.1. Titanium is commonly preferred for the aerospace and non-aerospace (chemical, medical, automotive, architecture, sports and etc.) industries thanks to its most attractive properties such as high specific strength (especially for higher temperatures, Figure 2.2) and excellent corrosion resistance [1, 2] .
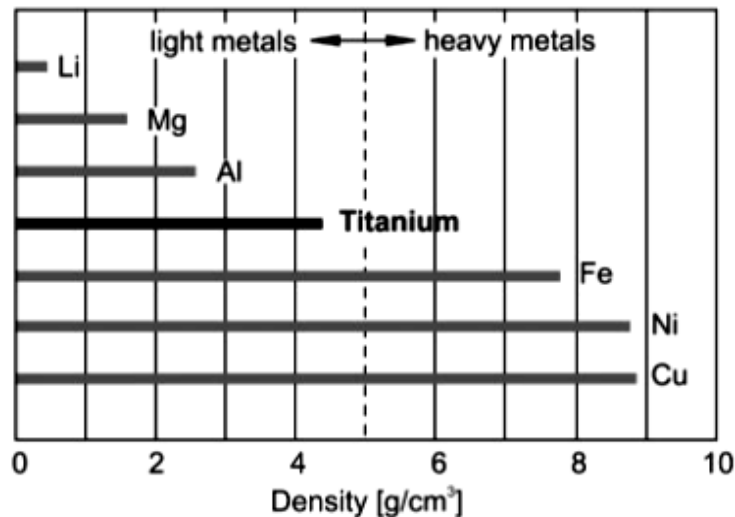
Figure 2.1. Densities of some metals [1].
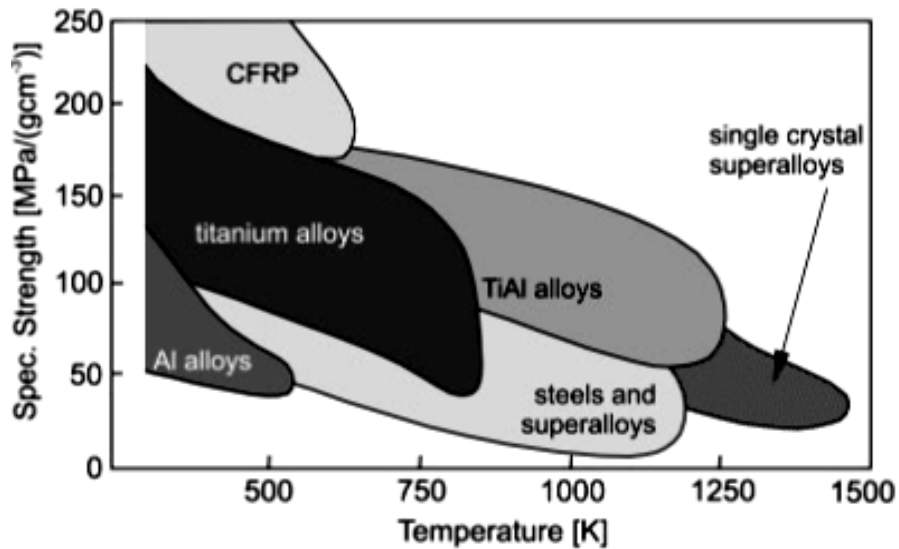
Figure 2.2. Specific strength versus temperature graph for various metals [1].

In 1940s, titanium and titanium alloys were particularly enhanced for aerospace industry in the United States, and worldwide titanium consumption is now around 50% for aerospace market. For the aerospace industry (e.g. airframe, gas turbine engines, helicopters etc.), the weight reduction is crucial when compared to automotive industry. For instance, while one kg weight reduction in aerospace industry causes about €1000 cost savings, the automobile industry cannot cost more than €10. Titanium and its alloys are used for the aerospace industry due to significant weight reduction (substitute for steels and Ni-based superalloys), corrosion resistance (substitute for Al-alloys and low-alloyed steels), comparatively high temperature resistance (substitute for Al alloys, Ni-based superalloys, and steels), galvanic compatibility with polymer matrix composites (substitute for Al alloys) [3].

Nowadays, titanium and titanium alloys are also commonly employed for other industries (chemical, biomedical, automotive and etc.) in addition to aerospace industry. Among them, medical industry is the most widely utilized area for titanium and titanium alloys.

Especially, titanium and titanium alloys meet the biomaterials' requirements and preferred in load bearing applications such as hip and knee joints, dental implants because of their high corrosion resistance, processability (powder metallurgy, casting, deformation, and etc.), biocompatibility, bio-adhesion (osseointegration), and suitable mechanical properties (e.g. bone-like Young's Modulus) [4,5].

2.2. Crystal Structure of Titanium

Titanium possesses two different crystal structure according to the temperature which is called α/β transus temperature which is 882 ± 2 °C for pure titanium and affected by substitutional and interstitial elements. The α phase having hexagonal close packed structure (hcp) is stable below β-transus temperature while the β phase having body centered cubic structure (bcc) is stable at higher temperatures (Figure 2.3). The relative amounts of α and β phases in the structure determines the final performance of titanium as crystal structure affects properties [1].
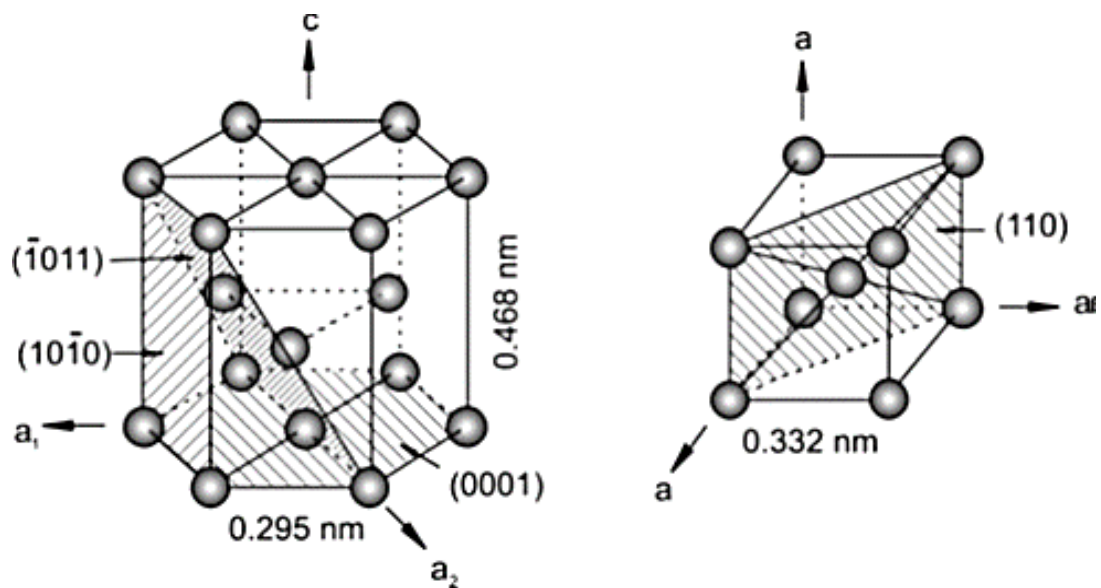
Figure 2.3. Crystal structure of hcp (α phase) and bcc (β phase) with their most densely packed directions and planes [1].

2.3. Phase Transformations in Titanium and Ti-Alloys

Microstructural development during production or post processing of titanium parts plays a critical role in determining the desired properties. In addition to non-equilibrium phases, α and β phases are the common equilibrium phases encountered in most of the titanium products. The shape, distribution and relative amounts of equilibrium phases are adjusted using different processes commonly to reach desired mechanical property.

The β phase is more ductile according to α phase because of having 12 possible slip systems. For α titanium (hcp structure), lattice parameters are a=0.295 nm and c=0.468 nm with the ratio c/a=1.587, but c/a ratio is 1.633 for an ideal hcp lattice structure. When substitutional or interstitial atoms (lesser atomic radii than titanium) are dissolved in α titanium, they enlarge the c/a ratio of the α titanium resulting in increased strength and reduced ductility. Therefore, relative amounts of each phases determine the final mechanical property. In addition to relative quantity, fineness of the phases alter strength and the ductility of the alloy. Because of that transformation of each phases to each other should be controlled carefully. The transformation of β titanium (bcc slip planes) to α titanium (hcp basal planes) during cooling occurs according to Burgers relationship (Figure 2.4) in which bcc can transform to maximum 12 hexagonal variants: $\{0001\}_{\alpha}//\{110\}_{\beta}$ and $\langle11\bar{2}0\rangle_{\alpha}//\langle111\rangle_{\beta}$. During cooling from β phase to α phase, {110} plane (bcc most densely packed planes) transforms to {0001} plane (hcp basal planes). As demonstrated in Figure 2.5, basal planes in hcp (α phase) are slightly larger than corresponding distance between {110} planes in bcc (β phase), and this situation causes a slight atomic distortion [1,6]. There are mainly two type of transformations: martensitic, and nucleation and diffusional transformations. Ti and its alloys have two different martensitic crystal structures that are hexagonal and orthorhombic martensite formed by quenching of β phase (bcc) from betatizing temperature below M_s temperatures.

In nucleation and diffusional growth transformations, Ti-alloys are cooled from single β region with slow rates into α+β phase region, and then the nucleation of α phase at β grain boundaries occurs by decomposition of β phase. The final microstructure consists of α colonies with the retained β, which is called "basket-weave" structure [7].
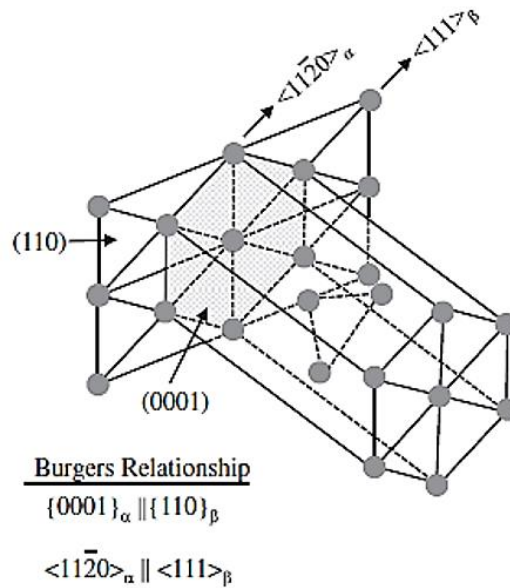
Figure 2.4. Burgers relationship during β/α phase transformation (Schematic) [8].
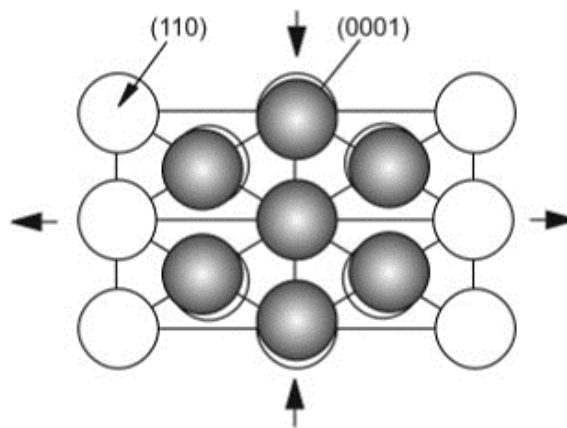
Figure 2.5. The transformation from β to α according to Burgers relationship [1].

2.4. Classification of Titanium Alloys

Titanium alloys are categorized according to types of equilibrium phases present in the microstructure which actually depends on alloying elements present in the alloy. The alloying elements of titanium alloys can be categorized as neutral, α-stabilizers, or β-stabilizers according to their effects on β-transus temperature (Figure 2.6).

The α-stabilizing elements (carbon, oxygen, nitrogen and aluminum) broaden the α phase field to higher temperatures and develop two phase (α+β) region, so α phase can be stable even at higher temperatures and among them, aluminum is the most significant alloying element thanks to its high solubility in both α and β phases. On the other hand, β-stabilizing elements which are subdivided into β-isomorphous (e.g. Ta, Mo and V) and β-eutectic elements (e.g. Co, Ni, Fe, Mn, Cr, Cu, Si, and H) cause to shift β phase field to lower temperatures. Among the interstitial elements, hydrogen is only one β-stabilizing element, and it lowers the β-transus temperature. Additionally, the effects of neutral elements on the β-transus temperature is negligible since they don't change the phase boundary. But if strength is considered, neutral elements (Sn and Zr) strengthen the α-phase [9].
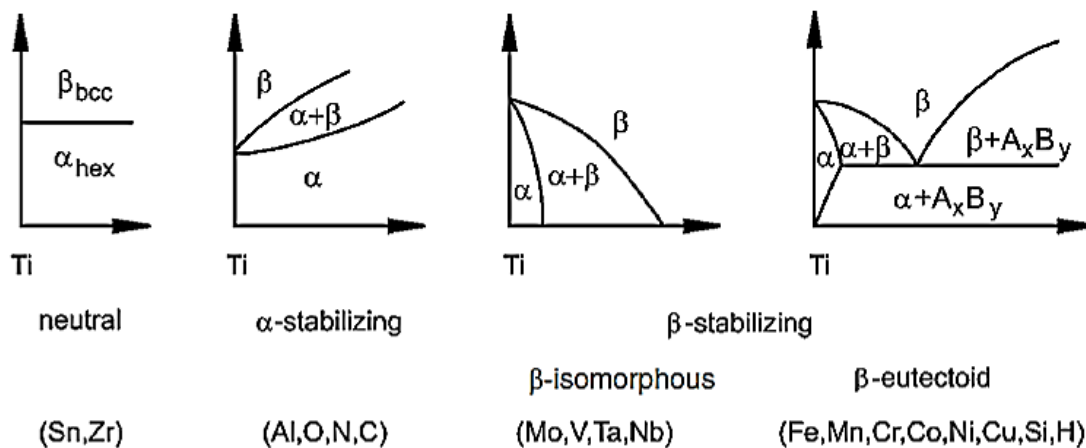
Figure 2.6. The effects of alloying elements on phase diagrams [1].

12

By considering the effect of alloying elements mentioned above, titanium alloys can be classified as near-α, α, α+β, metastable-β and β alloys according to their position in a pseudo-binary section through a β isomorphous phase diagram as schematically demonstrated in Figure 2.7. Some common titanium alloys which belong to each group are listed with their critical mechanical properties in Table 2.1.
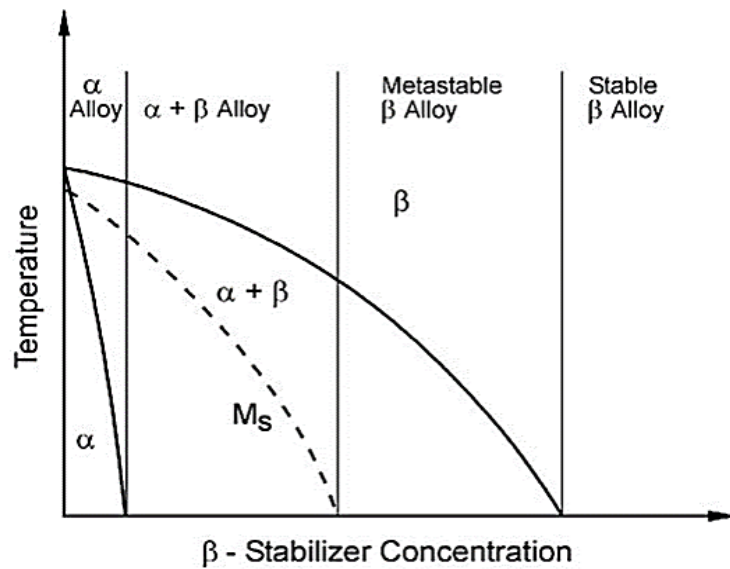
Figure 2.7. Schematic binary section through isomorphous phase diagram to categorize Ti-alloys [10].

Table 2.1. Mechanical properties of some titanium alloys [11].

Alloy	T_β [ºC]	Hardness [HV]	E [GPa]	YS [MPa]	TS [MPa]	% El
α Alloys						
high purity Ti	882	100	100-145	140	235	50
Grade 1	890	120		170-310	>240	24
Grade 4	950	260	100-120	480-655	>550	15
Near-α Alloys						
Ti-6-2-4-2-S	995	340	114	990	1010	13
TIMETAL 1100	1010		112	900-950	1010-1050	10-16
TIMETAL 834	1045	350	120	910	1030	6-12
α+β Alloys						
Ti-6-4	995	300-400	110-140	800-1100	900-1200	13-16
Ti-6-6-2	945	300-400	110-117	950-1050	1000-1100	10-19
Ti-6-2-2-2-2			110-120	1000-1200	1100-1300	8-15
Ti-6-2-4-6	940	330-400	114	1000-1100	1100-1200	13-16
Ti-17	890	400	112	1050	1100-1250	8-15
Metastable-β Alloys						
SP700	900	300-500	110	900	960	8-20
Beta III	760	250-450	83-103	800-1200	900-1300	8-20
Beta C	795	300-450	86-115	800-1200	900-1300	6-16
Ti-10-2-3	800	300-470	110	1000-1200	10001400	6-16
Ti-15-3	76	300-450	80-10	800-1000	800-1100	10-20

2.4.1. α and Near-α Alloys

Commercially pure (CP) titanium can take a position in the region of α-alloy because they are alloyed with α-stabilizing or neutral elements, and they can maintain their hcp crystal structures at room temperature. Among titanium alloys, α and near-α alloys are the most corrosion-resistant but the weakest alloys. In order to increase strength of the alloys, oxygen and nitrogen which are interstitial elements are used, and according to oxygen content in the alloy, grade of CP titanium has been determined.

The tensile strength of CP titanium changes between 240 and 740 MPa, and the lowest strength and excellent cold formability belongs to Grade 1 while the highest strength value is observed in Grade 4. α and near-α alloys display good weldability and excellent creep resistant, but they cannot be strengthened with heat treatments [12].

2.4.2. α+β Alloys

This group of Ti-alloy contains mixture of α favoring (i.e. Al) and β favoring (i.e. V and Mo) elements. α+β alloys are used when the balanced desired properties such as high tensile strength vs fracture toughness, good creep resistance vs low cycle fatigue and high tensile strength vs high cycle fatigue are required. Although the name of this group contain α and β phases, the microstructure can be changed and non-equilibrium phases can be obtained with the help of heat treatments (e.g. solution treatment). In addition to changing types of phases, heat treatment can be used to alter the morphology, relative quantity and distribution of phases and lamellar, equiaxed and bi-modal (duplex) microstructures can be obtained by changing thermomechanical treatment which will be discussed in the following sections. Among the α+β alloys, Ti-6Al-4V alloy is the most commonly used titanium alloy, and today more than 50% of titanium alloy parts are based on Ti-6Al-4V alloy [10,13].

2.4.3. Metastable-β and β Alloys

Metastable-β and β alloys enable the highest specific strength and very attractive combinations of fatigue resistance, strength and toughness at large cross sections, thus these alloys are the most versatile class of titanium alloys. However, according to α+β alloys, β alloys have higher density, moderate weldability, poor oxidation behavior, high formulation cost and etc. [14].

2.5. Ti-6Al-4V Alloy

Ti-6Al-4V alloy is the most commonly used α+β alloys, and it has 6 wt. % Al and 4 wt. % V. Elemental compositions of cast Ti-6Al-4V alloy defined by ASTM F1108-14 standard are demonstrated in Table 2.2.

Table 2.2. Chemical compositions determined by ASTM F1108-14 standard for cast Ti-6Al-4V alloy [15].

Element	Chemical Composition (wt.%)
Al	5.50 to 6.75
V	3.50 to 4.50
Fe	0.30 max.
O	0.20 max.
C	0.10 max.
N	0.05 max.
H	0.015 max.
Titanium	Balance

Ti-6Al-4V alloy has been extensively utilized in different fields such as aircraft gas turbine disks, surgical implants, cases and compressor blades, and pressure vessels due to its attractive properties such as low density, high specific strength, high corrosion resistance, high cycle fatigue strength.

The properties of the alloy change according to microstructure. The microstructure of the α+β titanium alloys changes according to applied thermomechanical processes which are complex sequence of deformation, solution heat treatment, aging, recrystallization, and annealing for stress relief, and it is possible to obtain different microstructures by tailoring the applied processes.

The arrangement and size of the α and β phases formed according to cooling rate from β phase region affect the microstructures such as lamellar, equiaxed, bi-modal, martensite and Widmanstätten of the Ti-6Al-4V alloy demonstrated in Figure 2.8, and hence mechanical properties are affected from the Ti-6Al-4V alloy's microstructure. The lamellar microstructure having more oriented colonies with a greater α/β surface area is formed when the homogenization treatment in β phase region, and subsequently a stress relieving heat treatment (which is performed for relieving

internal stresses occurred during rolling, welding etc. and it is a low-temperature treatment (482 to 704 $^\circ$C)) are applied to the alloy. Moreover, thermo-mechanical process (i.e. rolling in β phase or α+β phases regions) is applied as an additional process prior to the homogenization treatment for reducing the average β grain size, and the cooling rate during the homogenization treatment is significant because the lamellae size (α plates), the α colony size (effective for determination of slip length) and the thickness of α phase at grain boundaries are determined by cooling rate. The equiaxed microstructure having a uniform structure consisted of α grains and β grain boundaries is generated after a recrystallization process (firstly deformed into α+β phase field, and then solution heat treated at α+β phase region in order to recrystallize microstructure). When the mechanical properties of the lamellar and equiaxed microstructures are compared, lamellar microstructure has lower tensile ductility, lower strength, superior fracture toughness and better fatigue propagation resistance, and equiaxed microstructure has better fatigue initiation resistance and poorer fatigue propagation resistance. The bimodal (duplex) microstructure having equiaxed (primary) α in lamellar α+β matrix is obtained by solution heat treatment (just below the β-transus temperature), and it is actually a combination of equiaxed and lamellar microstructures. Therefore, the well-balanced fatigue properties such as higher fatigue crack initiation resistance and higher fatigue propagation resistance are observed for the bimodal (duplex) microstructure because it combines the advantages of both equiaxed and lamellar microstructures. The martensitic microstructure (hexagonal, α′, or orthorhombic, α″, with small amount of β) is formed through the rapid quenching alloy from above the β-transus temperature. At the end of the rapid quenching, hard and brittle alloy is obtained, and when the aging is applied at temperatures higher 400 $^\circ$C, hardness of the alloy increases through the formation of Ti_3Al ($α_2$) phase precipitates [3,10,13,16].

17
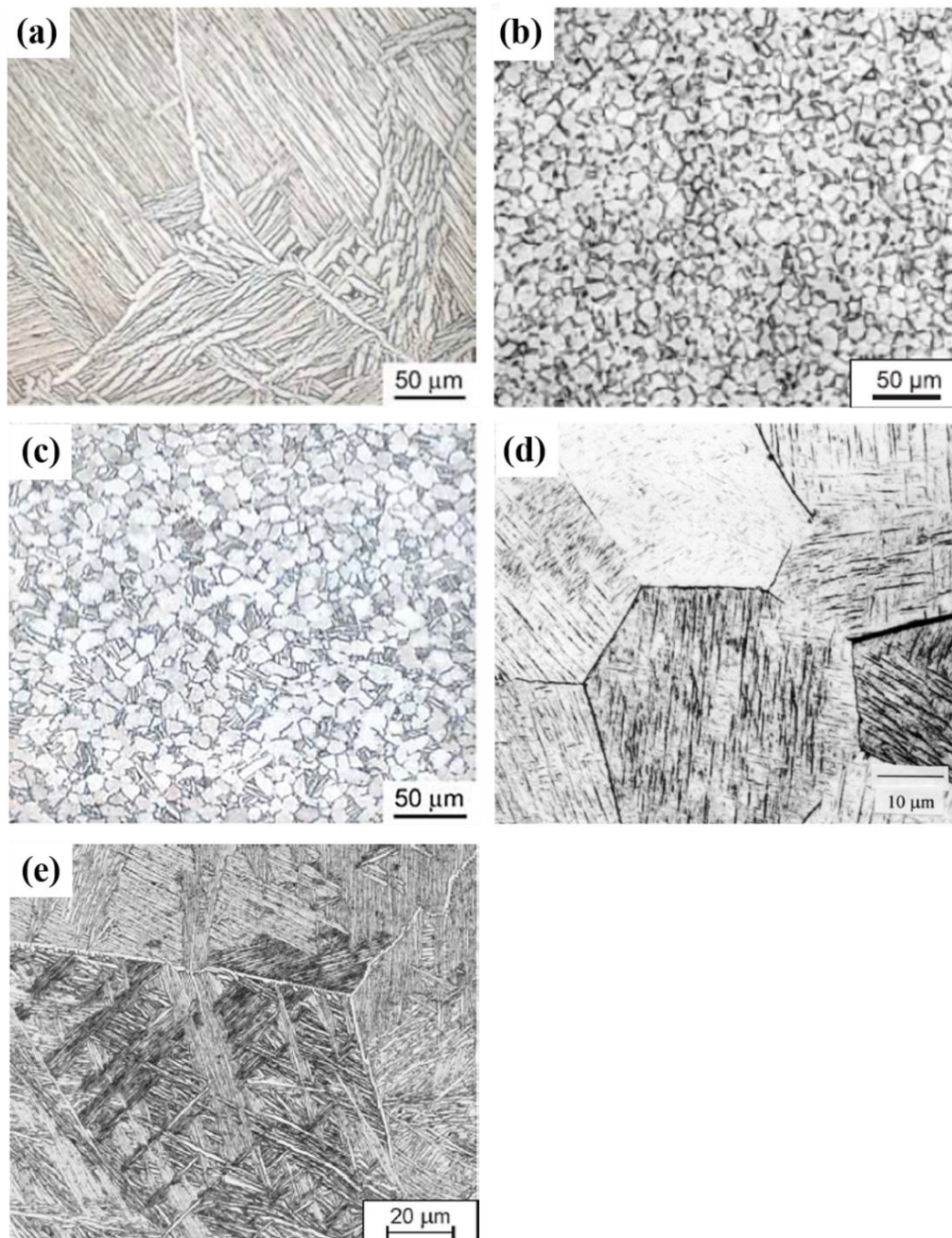
Figure 2.8. Optical micrographs of Ti-6Al-4V alloy where (a) lamellar [17], (b) equiaxed [18], (c) bimodal (duplex) [17], (d) martensitic [19] and (e) Widmanstätten/basket weave [20] microstructures.

In addition to these microstructures, the Widmanstätten also called basket weave microstructure which can be thought as a special type of lamellar microstructure (parallel plates of α crossed out by the β phase between them) is observed when the alloy cooled from extremely high temperature with critical cooling rate.

Figure 2.9 shows the formation of Widmanstätten microstructure obtained through slowly cooling from the β region to α region [1,19,21,22]. Additionally, the microstructural changes of Ti-6Al-4V alloy obtained by annealing at different temperatures with different cooling rates are illustrated in Figure 2.10.
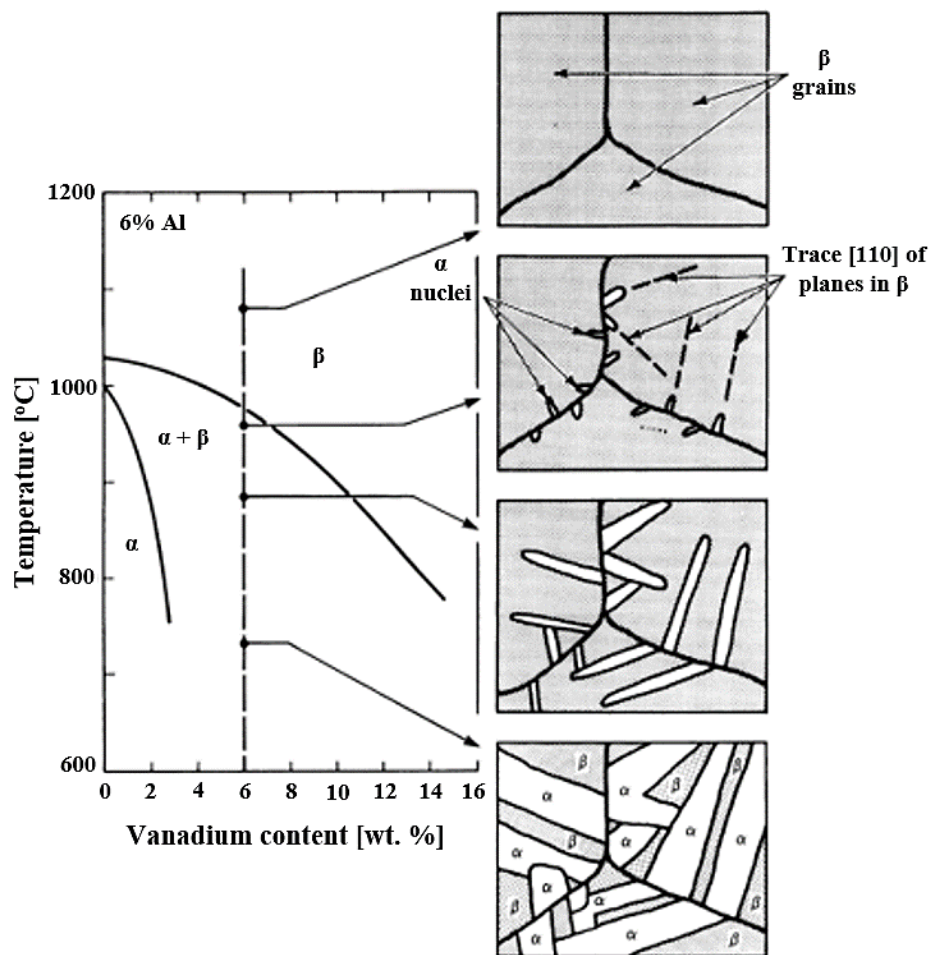
Figure 2.9. Schematic representation of Widmanstätten microstructure formation in an α+β alloy (Ti-6Al-4V) [12].

19

The lamellar microstructure, the thickness of α lamellae and diameter of α lamellae colonies strongly affect the mechanical properties of the α+β titanium alloys, and stereological parameters of lamellar microstructure are demonstrated in Figure 2.11 (a). Especially, the α colony size is significant for the mechanical properties because the size of α colonies influences the α and β phase thicknesses, and the slip lengths are affected by α colony size, so mechanical properties vary depending on α colony size (Figure 2.11 (b)). When the cooling rate increases, the α colony size (also slip length) decreases, and yield strength and high cycle fatigue (HCF) strength which is resistance to crack nucleation increase.

On the other hand, the reduced slip length or colony size decreases the rate of microcrack propagation and increases the material resistance against microcrack propagation, and hence low cycle fatigue (LCF) strength also increases. Although, the increment in ductility is observed with the reduction of colony size, in fact, this increment is resulted from the reduction in the amount of primary α phase formed at the grain boundaries through with more rapid cooling. Additionally, ductility again decreases when the martensitic microstructure having smaller α colonies are formed by rapid cooling. Also, the fracture toughness of the alloy changes directly proportional to the colony size [10,16,23].
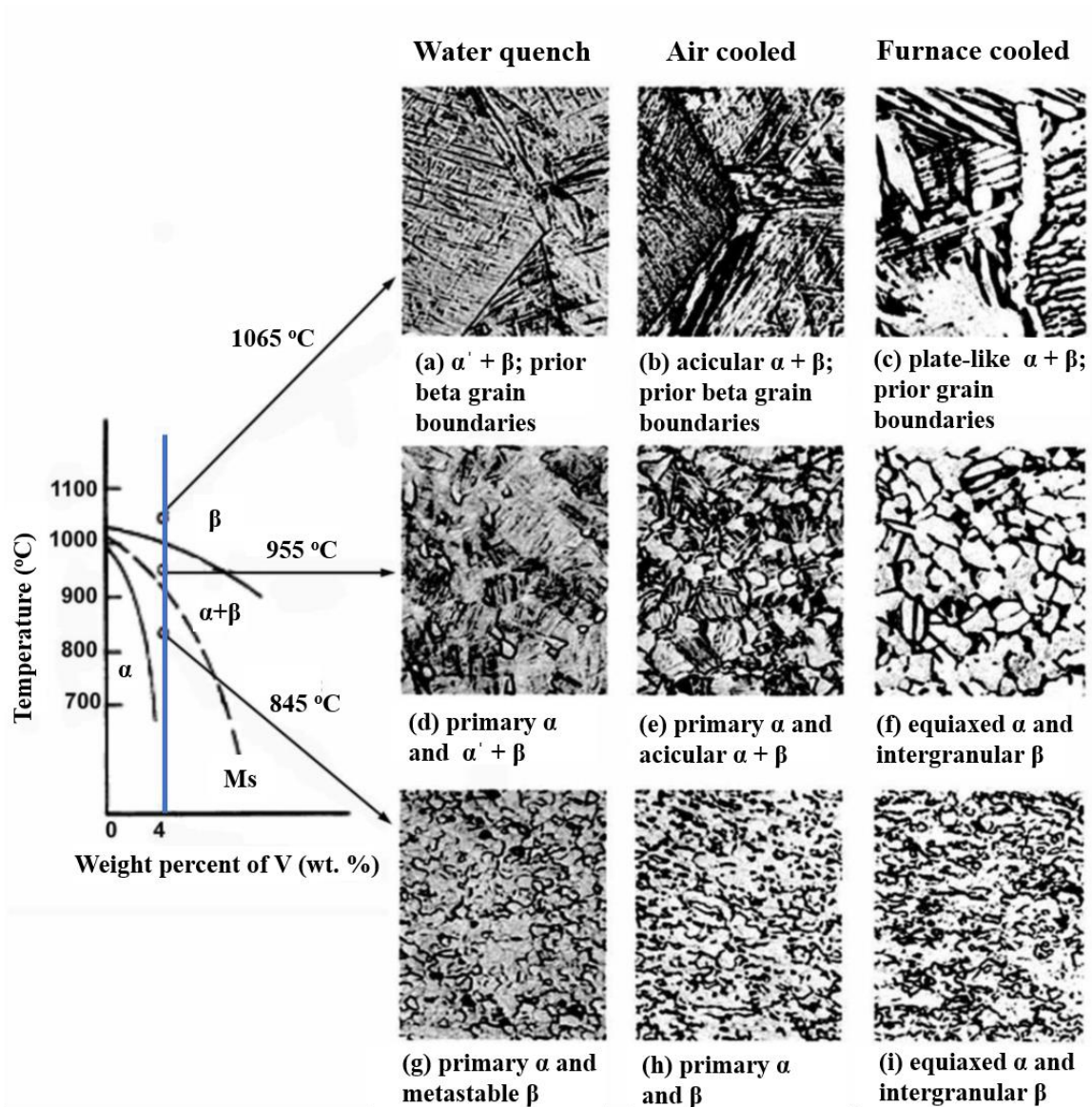
Figure 2.10. Microstructures of Ti-6Al-4V alloy formed by annealing at 1065 ℃, 955 ℃, 845 ℃ with different cooling rates (water quench, air cool, furnace cool). Vertical section of Ti-6Al-4V phase diagram (schematic). Etchant: 10HF, 5HNO$_3$, 85H$_2$O. 250x [12].
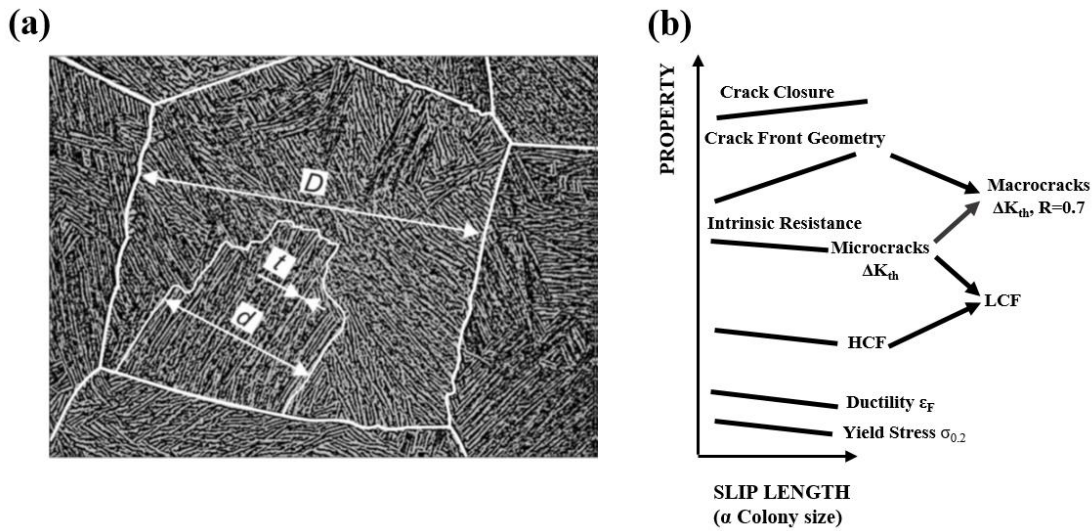
Figure 2.11. (a) Primary β phase (stereological parameters): grain size (D), parallel α-lamellae colony size (d), and α-lamellae thickness (t), and (b) Effect of slip length (a colony size) on mechanical properties (schematically) [20,24].

There are some commonly used heat treatments such as duplex annealing, mill annealing, and solution treating and aging for commercial Ti-6Al-4V alloy. In order to obtain relatively soft and machinable conditions, mill annealing process is applied, and the alloy is heated at about 730 °C in the α+β region for 4 hours, and then cooled to room temperature in the furnace for mill annealing process, and after the process, the microstructure comprises of globular crystals of β in an α matrix. Additionally, duplex annealing is also applied with several variants, and the alloy is heated at 955 °C for 10 minutes, then cooled in air, subsequently heated about 675 °C for 4 hours and cooled again to room temperature in air. Another heat treatment applied for Ti-6Al-4V alloy is solution treating and aging, and the alloy is heated at 955 °C for 10 minutes, quenched with water, and then aged for 4 hours between 540 and 675 °C, subsequently, cooled to room temperature in air [12,16].

Ti-6Al-4V alloy parts are mostly produced with conventional techniques (casting, powder metallurgy, welding/joining, forging and etc.) and to fabricate just one part generally more than one conventional technique is used together.

22

Also, production of very complex geometries is not possible in a single step with conventional techniques which are not cost effective if thousands of samples are not produced and design of parts change constantly. In contrast to conventional techniques, additive manufacturing (AM) techniques provide production of parts with complex geometries in one step by minimizing the usage of raw materials and providing energy and time savings for Ti-6Al-4V alloy [25–27].

2.6. Additive Manufacturing

2.6.1. General Information about Additive Manufacturing

Rapid prototyping (RP) was first presented to produce three-dimensional (3D) solid parts from computer-aided design (CAD) in the 1980s. The first additive manufacturing (AM) method was demonstrated at the University of Texas in 1986 with the improvement of RP techniques. AM is defined as "a process of joining materials to make objects from 3D model data, usually layer upon layer, as opposed to subtractive manufacturing methodologies" by ASTM F2792-12a [28], and various synonyms such as additive fabrication, additive processes, additive techniques, additive layer manufacturing, layer manufacturing and freedom fabrication can be used instead of additive manufacturing according to standard. Polymer, ceramic and metal parts can be fabricated with AM, and there are several AM techniques as summarized in Figure 2.12 to produce polymer (e.g. stereolithography and ink jetting), ceramic (e.g. binder jetting, ink jetting and stereolithography), and metal (e.g. directed energy deposition and powder bed fusion) parts [29–31].

AM provides lots of advantages when compared to conventional fabrication techniques. Production of very complex geometries in a single step with near-zero waste material and minimum need for post-processing are possible with AM.

Additive Manufacturing (AM) Processes							
Process	**Laser Based AM Processes**			**Extrusion Thermal**	**Material Jetting**	**Material Adhesion**	**Electron Beam**
	Laser Melting		*Laser Polymerization*				
Process Schematic	Laser source / Powder bed	Laser source / Powder supply	Laser source / Liquid resin	Material melt in nozzle	Material jetting	Laser cutting / Compactor	Electron beam / Powder bed
Name / Material	SLS	DMD	SLA	FDM	3DP	LOM	EBM
	SLM	LENS	SGC	Robocasting	IJP	SFP	
	DMLS	SLC	LTP		MJM		
		LPD	BIS		BPM		
			HIS		Thermojet		

Bulk Material Type	Powder	Liquid	Solid	

SLS: Selective Laser Sintering
SLM: Selective Laser Melting
DMLS: Direct Metal Laser Sintering
DMD: Direct Metal Deposition
LENS: Laser Engineered Net Shaping
SLC: Selective Laser Cladding
LPD: Laser Powder Deposition

SLA: Stereolithography
SGC: Solid Ground Curing
LTP: Liquid Thermal Polymerization
BIS: Beam Interference Solidification
HIS: Holographic Interference Solidification
FDM: Fused Deposition Modelling
3DP: Three-Dimensional Printing

IJP: Inkjet Printing
MJM: Multijet Modelling
BPM: Ballistic Particle Manufacturing
LOM: Laminated Object Manufacturing
SFP: Solid Foil Polymerization
EBM: Electron Beam Melting

Figure 2.12. Categorization of additive manufacturing techniques [26].

This design freedom opportunity allows to create unique products fabricated at low volumes in an economical way. If the cost of the manufacturing is considered, it should be divided into fixed and recurring costs. While fixed costs include tools, dies, buildings, recurring costs are the cost of materials, labor etc. When production volume of the parts is increased, conventional fabrication techniques become more economical way of manufacturing. On the other hand, the usage of AM becomes possible, when production volume is decreased, and the design is changed constantly. Therefore, it can be highly cost-savings, and it has the potential to decrease the cost, and energy associated with the transport, packaging and storage of parts. In addition to these benefits, AM reduces the energy consumption, so it has positive impact on the environment [29,30,32]. AM technologies are utilized for lots of applications such as biomedical, aerospace, automotive, military, sports, chemical, infrastructure and construction industries and etc. due to their benefits.

Biomedical applications (e.g. tools and instruments for medical devices, prosthesis, customized implants, education and training, drug delivery and etc.) need unique requirements such as high complexity, customization and patient-specific necessities, small fabrication quantities. AM provides the design freedom opportunity to create very complex parts, thus new biomedical implants, engineered tissues, extremely complex shapes (e.g. lattice structures with intentional porous structures) can be fabricated in a single step with AM technologies. Additionally, the main profit of AM is freedom for customized and patient-specific implants. Therefore, AM can also be used for improving the effectiveness and efficiency, and it can reduce the requirement of further operations for adapting the implant to the patient [33–35]. Although, AM has lots of benefits, there are a few drawbacks such as void formation between subsequent layer of materials, anisotropic microstructure and mechanical properties due to layer-by layer printing, and layer-by-layer appearance [36].

The aerospace industry accounting for 18.2 % of the total AM market today is the most promising fields in the near future. Aerospace components need some requirements such as complex geometries, difficult-to-machine materials, and high buy-to-fly ratio, customized production. Advanced and expensive materials (e.g. titanium alloys, high-strength steel alloys or ultra-high-temperature ceramics, and nickel-based superalloys,) are used in the aerospace industry, and these materials are very difficult to produce and create a large amount of waste materials (up to 95 %). Additionally, the aerospace industry is characterized by low volume production with constant change in part geometry. AM techniques can reduce waste materials during manufacturing and also enable fabrication of very complex shapes with an economical way [36,37].

The AM market is growing day by day and predicted that AM industry will grow to $21 billion by the year 2020. The industries such as automotive, electronics, and medical are the most rapid growth industries. According to reports, total market of the medical devices will be $1.5 billion by 2026, and also estimated that AM will be utilized for 80% of the implants in the near future [33].

2.6.2. Additive Manufacturing Processing Steps

AM is based on layer by layer production of objects. The process flow of AM is clearly depicted in Figure 2.13. Firstly, Computer Aided Design (CAD) model of the object is created and then, it is converted to Stereolithography (STL) file format. Subsequently, object is produced in AM system layer by layer. After the object is removed from the building platform, various post processes are applied.
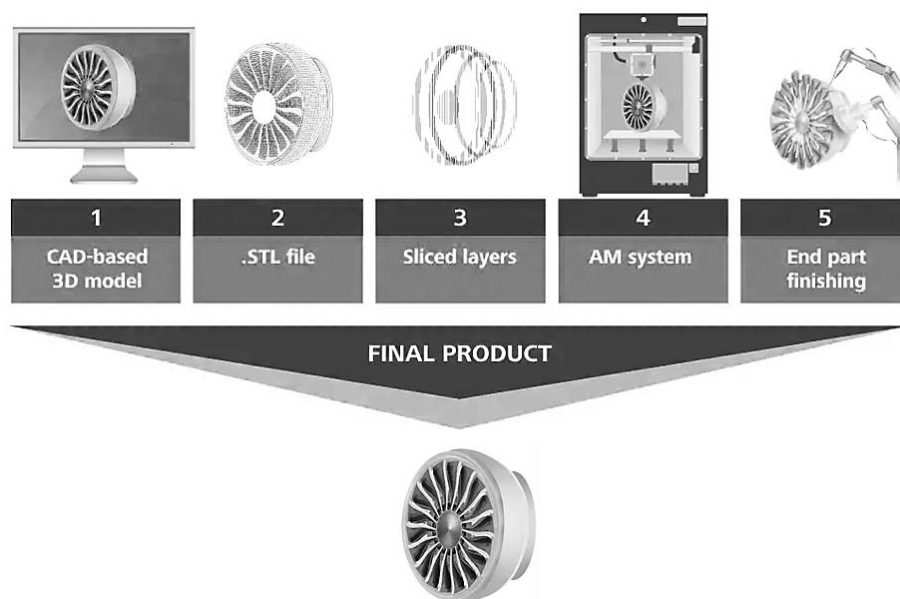
Figure 2.13. AM process flow [38].

2.7. Metal AM Techniques

Metal AM techniques utilize powder or wire as metallic feedstock and electron beam or laser as an energy source. The methods are based on partially or fully melting metallic material to produce fully dense or porous solid parts.

Directed energy deposition (DED) and Powder bed fusion (PBF) are the most commonly utilized metal AM techniques ensuring design freedom for fabrication of complex geometries when compared to conventional manufacturing techniques.

On the other hand, cold spraying, binder jetting, direct metal writing, and friction stir welding are some of other techniques that can be utilized for production of metal parts [36,39,40]. Among the metallic materials, titanium and its alloys (e.g. Ti-6Al-4V alloys), steel alloys (e.g. maraging steels, austenitic stainless steels, tool steels, precipitation hardenable stainless steels, and etc.), a few aluminum alloys (e.g. AlSi10Mg and AlSi12 alloys), nickel alloys (e.g. Inconel 718 and 625 alloys), some cobalt-based (e.g. CoCr alloys) and magnesium alloys have been used as raw materials in AM techniques. In addition to these metal alloys, magnetic alloys, high-entropy alloys, high-strength alloys, bulk metallic glasses (amorphous metals), metal composites and functionally graded materials (FGM) are a few research field for metallic AM techniques [36,41–44].

2.7.1. Directed Energy Deposition (DED) Technique

According to feedstock type, DED technique can be classified as wire feedstock developed from traditional welding and powder flow feedstock developed by Sandia National Laboratory in 1996. Additionally, DED technique uses electron beam or laser as an energy source [45,46]. DED technique mostly utilizes the related alloys for aerospace applications such as Inconel, titanium, aluminum, stainless steel. DED is relatively fast AM technique compared to other AM techniques, and material deposition rates of DED processes are higher than (PBF) processes, so that higher build volumes can be produced with DED systems. The nature of the DED systems is based on adding new materials to the existing parts, so the starting surface of the material doesn't have to be flat. Thus, they can be used to repair damaged parts (e.g. damaged turbine components).

Moreover, CNC machining and DED in a single machine can be combined as hybrid systems that are created by CNC manufacturers such as Matsuura and MAZAK in order to make exact finish in a machine [36,46,47].

Electron beam-based DED systems utilize a metal wire feedstock melted with an electron beam under the vacuum. These systems have the highest deposition rate up to 9 kg/h. The electron beam which has higher energy than laser provides higher accuracy with low deposition rates and thinner layers. NASA developed Electron Beam Freeform Fabrication (EBF) process generally utilized for space-based applications, and instead of powder injection, a metal wire filament is using in this technique [46,48].

Laser-based DED systems firstly developed in 1996 and named as Laser Engineered Net Shaping (LENS) utilize wire or powder feedstock. Laser-based DED technique was schematically demonstrated in Figure 2.14. The powder spray nozzles and the laser can move with together, if needed, and the system can have one or more nozzles. In this method, laser-substrate relative velocity, beam diameter and laser power, hatch spacing, powder feeding rate, and scanning strategy are important process parameters. Additionally, fully inert chamber is required if reactive metals are used [33,49].

Disadvantages of DED Techniques

The shape of the DED produced parts are the near net shapes with low accuracy, lower surface quality and less complexity, hence final machining step is required after the production. Therefore, generally large components with low complexity are produced with DED systems, and also, they are used to repair turbine engines. Additionally, if the fully inert chamber is utilized for the production, large volumes of argon or nitrogen are required, thus it takes time to get away oxygen from the chamber [36,46,50–52].
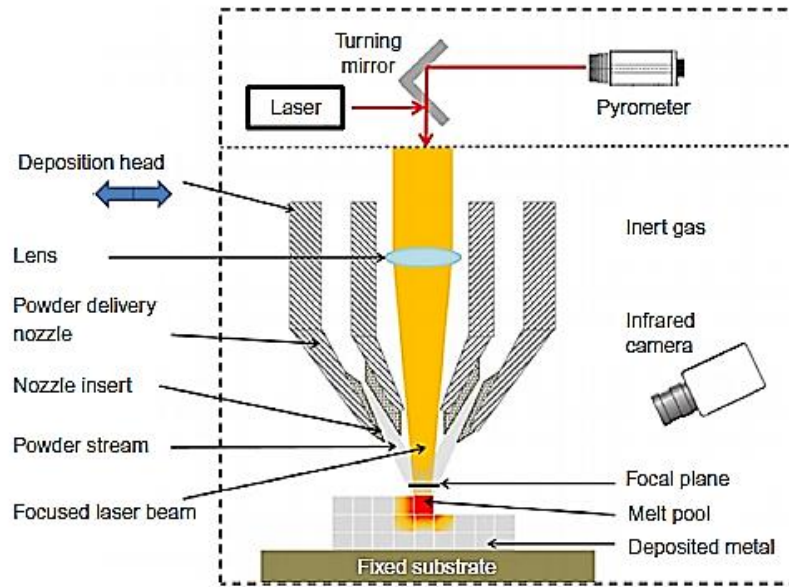
Figure 2.14. Laser-based DED technique [53].

2.7.2. Powder Bed Fusion (PBF) Technique

PBF uses laser (heats the powder bed via photon absorption) and electron beam (heats the powder bed by transferring kinetic energy) as a high energy source for melting or sintering metallic powders. In this technique, firstly thin layer of metal powder is spread onto the build plate, and powders are selectively melted according to CAD data. After that, the build platform is shifted down in the z-direction, and the process is repeated until the 3D part is produced. Each layer of the produced part is welded because of the penetration of power source deeper than a single layer. PBF techniques are categorized as electron beam melting (EBM) and laser powder bed fusion (L-PBF) according to power source used. The metal powders should be spherical, and their particle size distribution should be optimized for better powder flow and packaging. After the production, unfused powders are sieved to eliminate agglomerate particles, and then they can be reused for the other production by mixing with the new powder [46,54].

Laser-PBF AM systems utilize powders (in the range of 15-45 μm) and Nd-YAG fiber or ytterbium lasers as a power source. In addition to these lasers, CO_2 lasers are also used, but they are not suitable for metal AM systems due to need for high powers. In L-PBF systems, laser power ranges change between 50 W and 1000 W, and galvanometers and f-theta or dynamically using mirrors provide the focusing of the lasers. During the production, machine parameters such as scanning strategy, laser scan speed, laser power and the distance between each scan line are important and they should be optimized according to produced materials. In order to prevent contamination of the metals during the production, moisture-free and inert atmosphere (nitrogen or argon) is crucial. Powder recycling in this technique is also possible after sieving the used powders. When compared to other metal AM techniques, this technique is relatively slow. Although base plate is heated up to 200 °C during the process, high-temperature gradients can cause internal stresses induced to cracking or distortion in the produced parts. In order to eliminate internal stresses, heat treatment can be applied. Additionally, the surface of the produced parts is rough so that post treatments (e.g. bead or grit blasting) are required for some applications [41,46,55–59].

EBM-PBF AM systems invented by ARCAM AB (Sweden) are fundamentally a high-powdered scanning electron microscope (SEM) with magnetic coils, a filament, an electron beam column, and these systems utilize powder in the range of 45-105 μm and focused beam electrons as a power source. The production is conducted under vacuum with small amount of helium to eliminate electron deflection due to collision and interaction with gas molecules. In these systems, the powder bed temperature is higher than L-PBF systems and can be up to 1000 °C. Additionally, internal stresses are relatively low due to smaller temperature gradient because of scanning each powder layer by the low power electron beam before they melt. Production in this system is also faster due to faster scan and thicker power layer melting capability.

These systems can be only used for conductive materials, and vapor pressures of the alloying elements (in a heated vacuum) cause the losing of certain alloying elements (e.g. Ti-6Al-4V alloy suffers from losses of V and Al within the allowable specification limits) during the production of some alloys. Thus, reused powder should be mixed with virgin powder before each production [26,36,46,60–63].

Disadvantages of PBF Techniques

- The surface roughness is high due to partially melted or un-melted powders on the surfaces.

- During the production, internal stresses are developed because of temperature gradient differences, and post heat treatments are required to eliminate internal stresses.

- The support structures are added during the production due to the lack of self-supporting structures.

- The build parts can have defects (e.g. lack of fusion of layers, porosity, delamination and balling) after the production [61,63–66].

2.8. AM for Ti-6Al-4V Alloy

Ti-6Al-4V alloy parts are mostly fabricated with conventional fabrication techniques such as forging, powder metallurgy, casting, and etc., and generally more than one technique are used together to fabricate just one part. In addition to this, production of very complex geometries with high precise cannot be possible in a single step with conventional manufacturing techniques which are not cost effective and result large amount of waste material. AM techniques enable fabrication of Ti-6Al-4V alloy parts with complex geometries and near-zero waste material in a single step. In order to produce Ti-6Al-4V alloy parts with high complexity, various metal AM techniques such as PBF and DED have been used, but in this chapter electron beam melting (EBM) and selective laser melting (SLM) techniques are summarized for production of Ti-6Al-4V alloy parts [10,12,31,41,67–71].

31

2.8.1. Electron Beam Melting (EBM)

EBM is a PBF technique, and it was created by ARCAM AB (Sweden) and commercialized in 2001. Although EBM was only suitable for tool steel at the beginning, nowadays many metals that should be conductive such as Ti-based alloys (e.g. TiAl and Ti-6Al-4V alloys), Co-based alloys, Ni-based alloys (e.g. Inconel 625 and 718) and Cu can be produced with EBM technique. ARCAM has different EBM models such as ARCAM Spectra H which enables faster builds and leading high temperature production, ARCAM Q10plus which is for orthopedic implant manufacturing, ARCAM Q20plus which is for aerospace components, ARCAM A2X which is for aerospace production and research and development (R&D) materials.

EBM is also named selective electron beam melting (SEBM) due to selectively melting of metal powder, and the operating system of EBM can be considered as scanning electron microscope. The main components of ARCAM EBM machine are schematically shown in Figure 2.15 [72–75].

In the EBM system, the electron beams created by the electron gun are focused by magnetic lenses and accelerated with acceleration voltage (60 kW). The metal powder which is fed from hopper and distributed by a rake is selectively melted by the accelerated electron beam. The build plate size is typically 200 mm x 200 mm x 350 mm, and the process is performed under vacuum (around 10^{-4} torr) in order to eliminate electron beam and air interaction. Additionally, a small amount of inert He gas is utilized during melting to provide thermal stability of the process and to prevent the build-up electrical charges in the powder. Basically, the production process is depicted in Figure 2.16. The start plate is preheated before the first layer is added. The base part of the final part is obtained by the first powder layers melted which becomes the support structure of the real part [72,73,76–78].
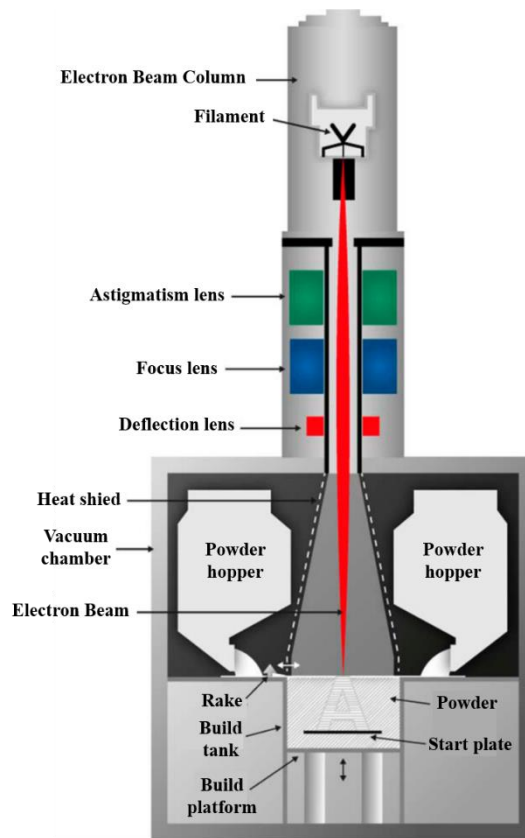
Figure 2.15. EBM system (schematic), courtesy of ARCAM AB [73].
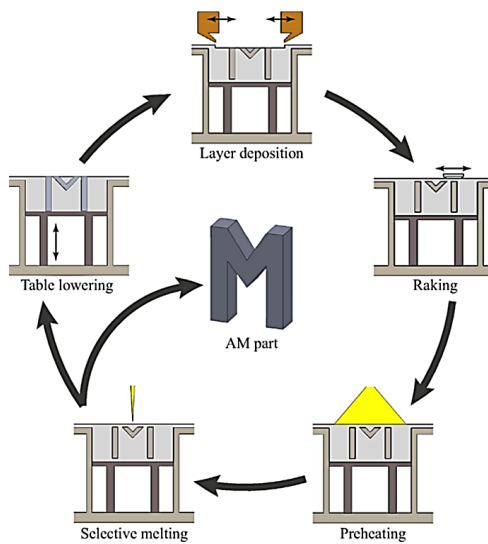
Figure 2.16. EBM build process (schematic) [78].

A series of defocused beam pre-heat the powder bed by scanning several times with high beam current and high scan speed (e.g. up to 30 mA and about 10^4 mm/s) which are lowered subsequent melting step. The metal powders are added when build plate is lowered after melting of one layer of powder. After production is finished, He pressure is increased to cool the build part, so electrical charging of the powder particles is inhibited, and this pressure increase provides heat conduction and cooling of the melt. The cooled build part, which consists of powders adhered to build part is broken by sandblasting. The unused powder is sieved and used several times since contamination is limited due to high vacuum utilized. In addition, more than 99 % density can be obtained with optimized process parameters by EBM [2,32,41,72,76–82].

High surface roughness and internal porosity due to partially melted powders can be reduced by decreasing the layer thickness, focus offset, line offset, beam current, and line energy. However, in most cases a post processing is needed to reduced surface roughness and increase the density of the part. Figure 2.17 demonstrates the external surfaces of the as-produced Ti-6Al-4V alloy parts in vertical and horizontal directions. Partially melted and sintered powders adhering to the external surface creates high surface roughness [2,5,31,59–61].

Since the cooling rate of the part during production is relatively low, equilibrium structure can be found in the alloy. Therefore, mechanical properties of EBM produced alloy is highly different from the alloys which are fabricated by SLM technique. The microstructure of the as-produced EBM Ti-6Al-4V alloy (Figure 2.18) consists of α plates which are in a Widmanstätten structure also called basket-weave structure and small amount of β inside in prior β columnar grains growing along the building direction. Rafi et al. [60] reported that during the production, build chamber is at 650-700 °C, so the build part cools from elevated temperatures down to 650-700 °C which is above the martensite start temperature, thus in contrast to production by SLM, martensite formation is inhibited. However, more primary α is formed along the grain boundaries of prior beta grains [5,83].
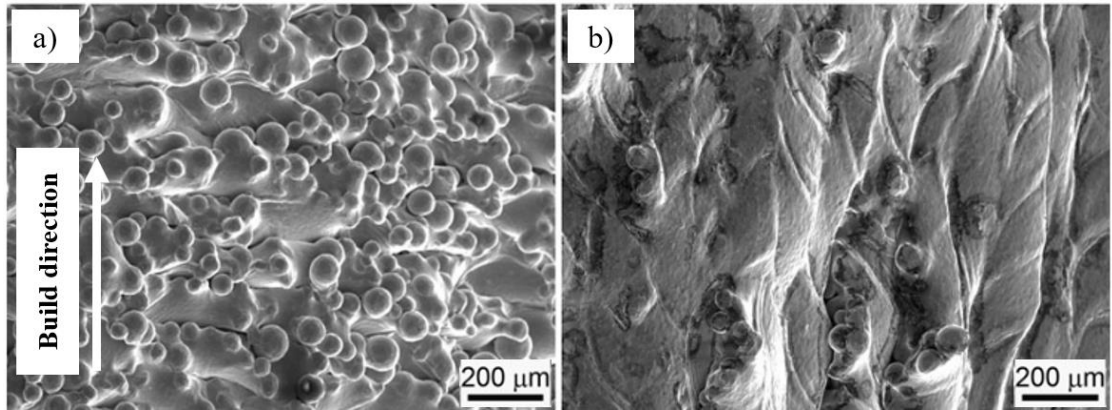
Figure 2.17. SEM images of external surfaces of (a) a vertically built and (b) horizontally built EBM Ti-6Al-4V alloy components [60].
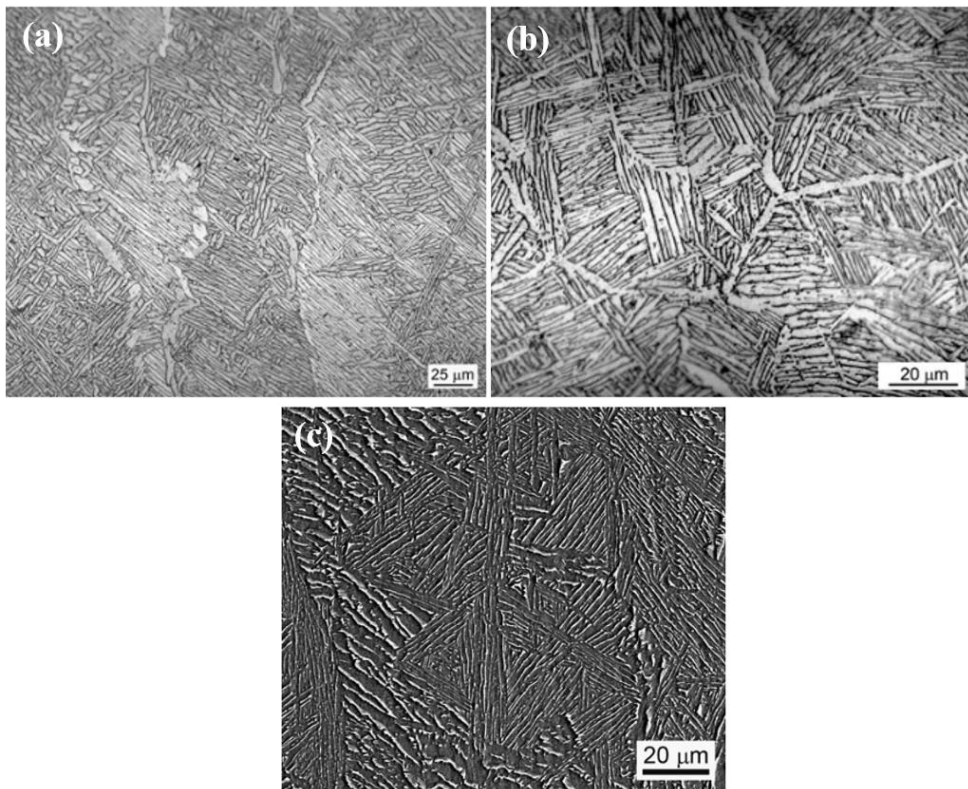
Figure 2.18. Optical micrographs (a, b) and SEM image (c) of the as-produced EBM Ti-6Al-4V alloy samples: (a) longitudinal direction and (b) transverse direction [60].

Liu et al. [31] reviewed tensile properties of as-produced EBM Ti-6Al-4V alloy samples at different conditions shown in Table 2.3. Additionally, ASTM F2924-14 standard [84] determined such as yield strength, ultimate tensile strength and strain at fracture as 825 MPa, 895 MPa and 10 %, respectively, by for the as-built AM Ti-6Al-4V alloy.

The tensile properties of AM Ti-6Al-4V alloy produced in horizontal and longitudinal directions show significant difference due to anisotropy behavior of AM Ti-6Al-4V alloy parts. Figure 2.19 demonstrates the AM Ti-6Al-4V anisotropy behavior when the tension loads applied along the horizontal and longitudinal directions.

Specimens tested perpendicular to columnar grain direction fail much more easily compared to those tested in parallel directions to columnar grains. Because, short axis of β grains is exposed to tension loads and α grain boundary causes separation of adjacent β grains. On the other hand, when the tension loads are applied to longitudinal specimens, columnar β grains and entire grain boundary α are loaded [31,85,86].

Table 2.3. Tensile properties for Ti-6Al-4V alloy produced by EBM in different conditions
[27,31,60,87–92].

Condition	Specimen Direction	UTS [MPa]	YS [MPa]	EL [%]
As-built, not machined	-	960 ± 2	850 ± 6	6.8 ± 0.5
As-built, not machined	Longitudinal	851 ± 19	812 ± 12	3.6 ± 0.9
As-built, not machined	Horizontal	833 ± 22	783 ± 15	2.7 ± 0.4
As-built, machined, interior location	Longitudinal	1032.9 ± 12.9	984.1 ± 8.5	9.0 ± 2.9
As-built, machined, exterior location	Longitudinal	1008.6 ± 15.2	961 ± 7.1	7.1 ± 3.4
As-built, machined, interior location	Horizontal	1029.7 ± 7	982.9 ± 5.7	12.2 ± 0.8
As-built, machined, exterior location	Horizontal	1017.4 ± 4.9	966.5 ± 5.3	12.2 ± 2.0
As-built, machined	Longitudinal	972 ± 14	845 ± 9	14.2 ± 1.5
As-built, machined	Horizontal	976 ± 11	846 ± 7	15.0 ± 2.0
As-built, machined	Longitudinal	1045	970	10.9
As-built, machined	Longitudinal	1073–1116	1001–1051	11–15
As-built, machined	Horizontal	1032–1066	973–1006	12–15
As-built, machined	Longitudinal	928 ± 9.8	869 ± 7.2	9.9 ± 1.7
As-built, machined	Horizontal	978 ± 3.2	899 ± 4.7	9.5 ± 1.2
As-built, not machined	-	790 ± 10	740 ± 10	2.2 ± 0.3
Annealed, machined	-	837–918	741–842	3–9
HIPed, machined	-	817–918	723–817	3–9
Stress relieved, machined	-	885–1015	778–943	3–9
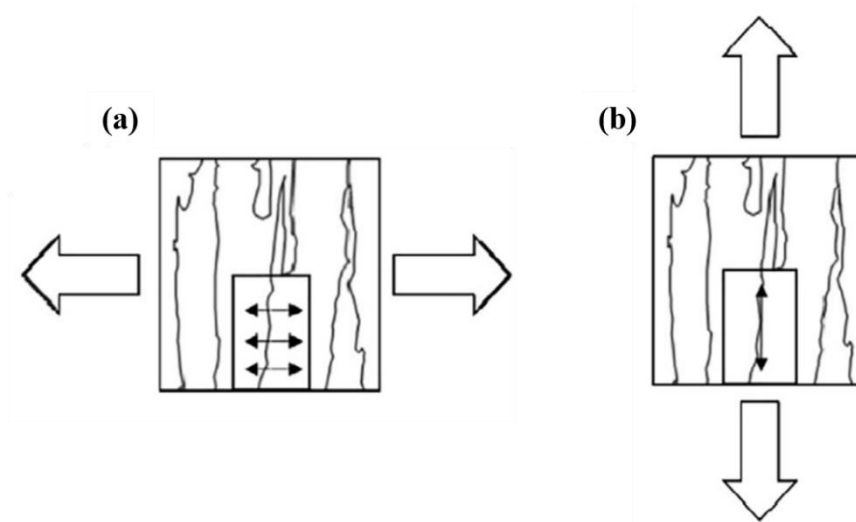
Figure 2.19. Anisotropy behavior of Ti-6Al-4V alloy parts produced by AM in different orientations (a) horizontal and (b) longitudinal under subjected tensile loads [85].

2.8.2. Selective Laser Melting (SLM)

SLM also known as laser beam melting (LBM), laserCUSING, direct metal laser sintering (DMLS), industrial 3D printing or laser metal fusion (LMF) is a PBF technique. In this process, metal powder (thin layer) is laid on a substrate plate in a building chamber which is filled with inert gas (argon or nitrogen) to prevent oxidation, and selective melting is achieved by using laser power sources which are CO_2 or Nd:YAG. Process parameters such as scanning speed, laser power, layer thickness, and hatch spacing, are optimized to produce high density metal. Particle size of the metal powders is relatively smaller, thereby yielding thinner parts with lower surface roughness. Additionally, theoretical density of Ti-6Al-4V alloy components built by SLM (about 99 %) is lower than EBM. Figure 2.20 illustrates the surface of the Ti-6Al-4V alloy component fabricated by SLM [30,31,41,60,66,70,93,94].
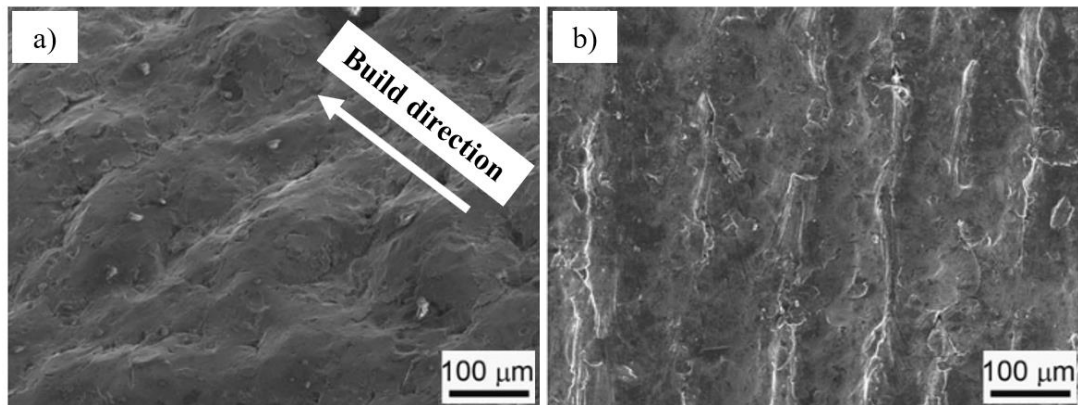
Figure 2.20. SEM images of external surfaces of (a) a vertically built and (b) horizontally built SLM Ti-6Al-4V alloy components [60].

The microstructure of Ti-6Al-4V alloy fabricated by SLM, Figure 2.21, is commonly composed of martensitic (α') microstructure in columnar prior beta grains due to rapid cooling [5,60,93].

The tensile properties of as-produced SLM Ti-6Al-4V alloy samples at different conditions are tabulated and summarized by Liu et al. [31]. SLM produced samples have higher strength and low elongation due to martensitic microstructure seen in built samples. Kasperovich and Hausmann [95] reported that the tensile properties (UTS, YS and EL %) of as-produced and un-machined Ti-6Al-4V alloy samples produced in longitudinal orientation as 1040-1062 MPa, 664-802 MPa, 11.3-12.7 %, respectively. Additionally, Edwards and Ramulu [96] found the tensile properties (UTS, YS and EL %) of as-produced and un-machined Ti-6Al-4V alloy samples produced in horizontal orientation are 1035 ± 29 MPa, 910 ± 9.9 MPa, 3.3 ± 0.76 % respectively. Finally, differences between EBM and SLM are shown in Table 2.4.
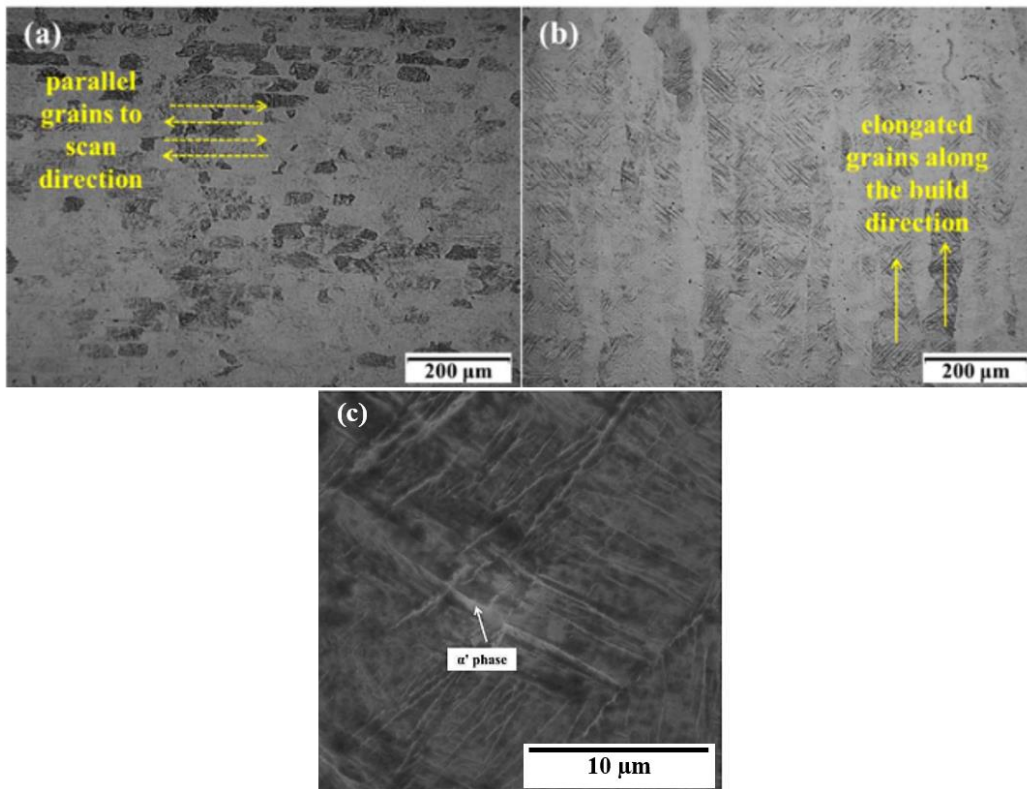
Figure 2.21. Optical micrographs (a, b) and SEM image (c) of the as-produced SLM Ti-6Al-4V alloy sample: (a) transverse direction and (b) longitudinal direction [58,94].

Table 2.4. Differences between EBM and SLM processes [58].

Characteristic	EBM	SLM
Thermal source	Electron beam	Laser
Atmosphere	Vacuum	Inert gas
Scanning	Deflection coils	Galvanometers
Energy Absorption	Conductivity limited	Absorptivity limited
Powder preheating source	Electron beam	Infrared or resistive heater
Scan speed	Very fast	Limited by galvanometer
Cost of energy	Moderate	High
Surface quality	Poor	Moderate
Feature resolution	Moderate	Excellent
Materials	Metal	Polymer, ceramic, metal
Powder particle size	Medium	Fine

2.8.3. Common Defects for AM Ti-6Al-4V Alloy

Spherical gas pores and lack-of-fusion (LOF) defects (Figure 2.22) are the most common defects for Ti-6Al-4V alloy produced by EBM. Argon gas left between the powder layers and entrapped gas in powders during powder production create pores which degrade mechanical properties. Scanning parameters also affect the location of gas pores. The LOF defects called as non-spherical, irregularly shaped voids result from incomplete melting of powders due to non-optimized building parameters. Post-process heat treatments can mitigate spherical gas pores and (LOF) defects. Additionally, melt balling or layer delamination are derived from build failure. EBM produced Ti-6Al-4V alloys' surfaces contain partially melted powders which increase the surface roughness and reduce the parts strength and fatigue strength due to notch effect created on the surface [97,98].
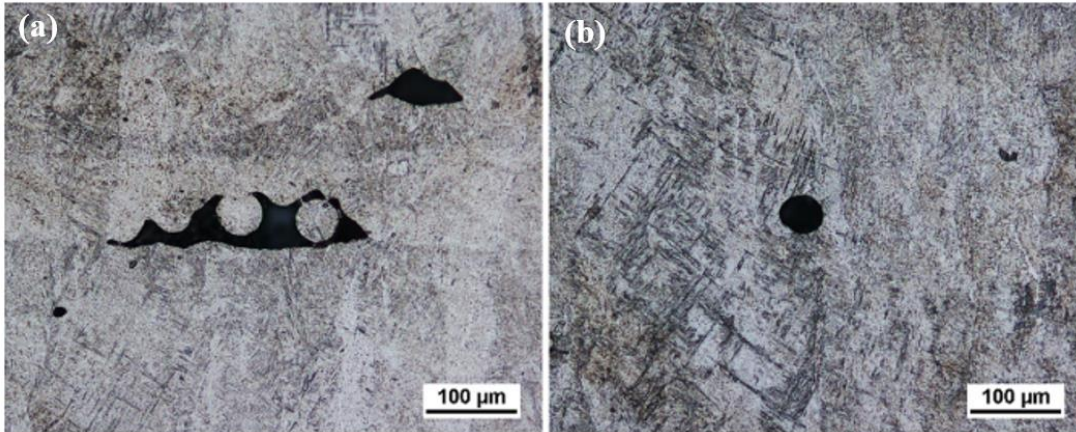
Figure 2.22. Optical images of (a) a lack-of-fusion void and (b) gas porosity [99].

2.8.4. Post Processes Used to Ti-6Al-4V Alloy Produced by AM

High surface roughness causes poor mechanical properties for Ti-6Al-4V alloy parts fabricated by AM due to microcracks initiate from surface defects. Therefore, machining or vibro-abrasive machining, blasting (i.e. with Al_2O_3), milling, chemical etching, chemical polishing, and etc. are mostly used post processes after AM to reduce surface roughness of the AM produced parts, and hence to improve mechanical properties [100–104].

In addition to surface processes, several heat treatments are conducted for Ti-6Al-4V alloy produced by AM to tune the mechanical properties and eliminate the residual stress by changing the microstructure of the as-build part. Generally, three possible forms of post-heat treatments are utilized for Ti-6Al-4V alloy. The first one is a conventional annealing heat treatment applied to remove residual stress above the usual stress-relief cycle temperature (482-704 °C) and below the β-transus temperature to prevent grain coarsening. In the second type of heat treatment, two-stage heat treatment is applied by quenching from above the β-transus temperature which is followed by tempering β-transus temperature. Other type of treatment includes, hot isostatic pressing (HIP) conducted over 900 °C under high pressure to decrease porosity and residual stresses [31,63,97,99,105].

42

In one of the study, Galarraga et al. [99] analyzed the effect of annealing time and temperature by conducting experiments at 600 ºC, 700 ºC, and 800 ºC for 10 and 120 h. They concluded that the increase in temperature and time cause coarsening of α laths. Another study of Galarraga et al. [105] includes the effects of cooling rate of post-heat treatment on the microstructure and mechanical properties of Ti-6Al-4V ELI alloy fabricated by EBM. Firstly, specimens were solution treated at 1100 ºC for 30 minutes, then they were cooled in furnace, air and water to observe the effect of cooling rate. Also, they examined the effect of subsequent aging treatment (925 ºC / 1h solution treatment + air cooling + 450 ºC / 4h aging treatment and 925 ºC / 1h solution treatment + water cooling + 450 ºC / 4h aging treatment) on microstructure and mechanical properties. They concluded that α′ martensite obtained by water-cooling provides 31 % higher UTS and 86 % lower ductility when compared to lamellar α+β phase obtained by furnace-cooling.

Chern et al. [97] examined the fatigue behavior of Ti-6Al-4V alloy built by EBM after different post processes. They compared the effect of annealing and stress-relieving heat treatment on the microstructure and mechanical properties of parts before and after machining and HIP. According to their study, annealing or stress-relief heat treatments lead coarsening of microstructure, so that there was no enhancement of fatigue-limit, and to enhance the fatigue resistance of EBM parts, they offer the HIP and machining together as the most effective method.

2.9. Thermo-Hydrogen Processing (THP)

Conventional post-heat treatments performed to Ti-6Al-4V alloy parts produced by AM discussed in the chapter 2.8.4. There is an alternative heat treatment called thermo-hydrogen processing (THP) which is actually applied powder metallurgy and cast titanium and titanium alloys parts to refine the microstructure [94,106,107].

Bilgin et al. [94] used THP for the first time for AM Ti-6Al-4V alloy parts produced by SLM with the aim of microstructural refinement and improvement of mechanical properties. To the best of author's knowledge, THP has not been applied for Ti-6Al-4V alloy produced by EBM. In this study, unlike the most of the annealing heat treatments, THP was proposed as an alternative heat treatment which increases the ductility of the alloy without degradation of the strength as a result of refined microstructure.

2.9.1. General Information about THP

THP enables refinement of the microstructure in powder metallurgy and cast titanium and titanium alloys fabricated by conventional methods without use of deformation. It is based on alloying and dealloying of titanium and titanium alloys (be able to absorb up to 50 at. % at 600 °C) with hydrogen thanks to its high diffusivity in titanium and reversible reaction of hydrogen with titanium. Hydrogen can be removed easily by vacuum annealing due to positive enthalpy of solution in titanium.

In addition to microstructural refinement, hydrogen alloying is also used in titanium powder production due to hydrogen embrittlement during ball milling which is used to obtain micron sized powders. Additionally, many processing such as working, machining, powder production, sintering, compaction, and etc. can be enhanced with THP since hydrogen dissolved in titanium reduces β-transus temperature, therefore, makes it possible to work at relatively lower temperatures. Basically, THP is composed of hydrogenation and dehydrogenation processes, but there are many different types of THP as listed in the studies [106–109].

2.9.2. Effects of Hydrogen in Titanium Alloys

The β phase (more ductile high-temperature bcc phase) is stabilized and the α phase (low-temperature hcp phase) is destabilized with alloying of hydrogen which is a unique alloying interstitial element in titanium and titanium alloys. The β-transus temperature (e.g. 39 at. % hydrogen decreases the β-transus temperature from 882 °C to 300 °C for pure titanium) and martensite transformation temperature reduce when

the α+β phase range becomes wider. Diffusion coefficient of the alloying elements in the β phase is reduced with hydrogen addition, thereby causing slower transformation from β to α. Additionally, hydrogen atoms occupy tetrahedral interstitial sites, and a new phase called titanium hydride (δ-hydride, TiHx) with fcc lattice structure forms on the free surfaces and at α/β interfaces when hydrogen exceeds its solubility limit in phases. While the stoichiometric ratio, x, of the δ-hydride is 2, the nonstoichiometric ratio, x, changes between 1.5 and 1.9. During the transformation from α phase to δ-hydride phase, volume expansion (about 17.2 %) occurs and creates high internal stresses in the α matrix. In addition to this, when the hydrogen solubility is maximum, the volume expansion for β phase is about 5.35 %. The shear and Young's moduli of the α phase decrease and the properties are enhanced for β phase with hydrogen because the interactions of dislocations with obstacles are affected by hydrogen and results in the strengthening of β phase and softening of α phase [106,108,110–112].

2.9.3. The Hydrogen Absorption Characteristics of Ti-6Al-4V Alloy

The hydrogen concentration, hydrogenation temperature and hydrogen partial pressure affect the hydrogen absorption characteristics of titanium and its alloys. Hydrogen diffusion occurs when the Ti-6Al-4V alloy is heated under hydrogen atmosphere at a certain temperature until the solubility limit of Ti-6Al-4V alloy is reached [58,113].

Zhang and Zhang [114] studied hydrogenation characteristics of cast Ti-6Al-4V alloy, and they concluded that increased hydrogen partial pressure results increasing the hydrogen content of the specimen increases at constant temperature (Figure 2.23 (a)). According to their study, hydrogen absorption which decreases with increasing the temperature strongly depends on hydrogenation temperature (Figure 2.23 (b)), and the temperatures between 400 ºC and 1000 ºC enable the hydrogen absorption of the specimens.
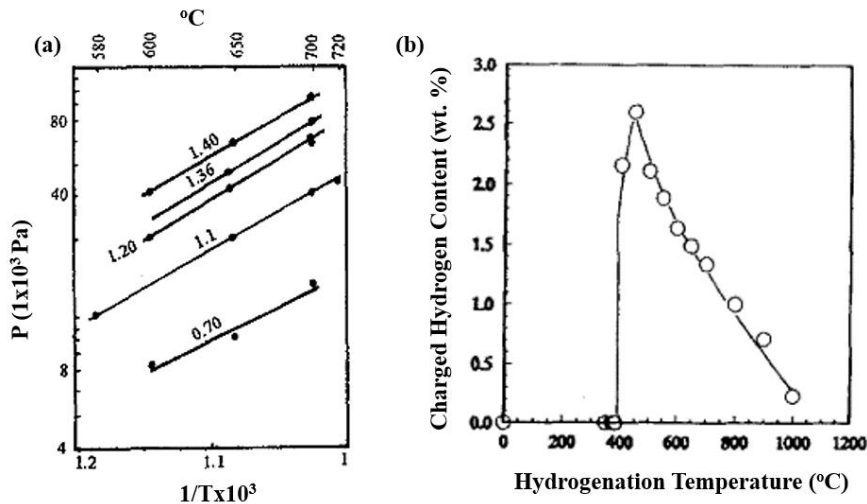
Figure 2.23. Relationship (a) between hydrogen pressure and hydrogenation temperature for various hydrogen contents and (b) between hydrogen content and hydrogenation temperature [114].

Bilgin et al. [94] applied hydrogenation for Ti-6Al-4V alloy built by SLM at different temperatures (550, 600, 650, 700, 750, 800, 850 °C), and found the maximum hydrogen solubility (1.19 wt.%) temperature as 650 °C above which the solubility of hydrogen decreased. In addition to this study, Pushilina et al. [115] reported that the hydrogen solubility for Ti-6Al-4V alloy produced by EBM is about 0.90 wt. % at 650 °C .

2.9.4. Titanium-Hydrogen Phase Diagrams

The simple eutectoid type titanium-hydrogen system is composed of hcp-α, bcc-β and δ-hydride phases (stoichiometric composition TiH_2) as demonstrated in Figure 2.24. The maximum hydrogen concentrations in hcp-α, bcc-β and δ-hydride phases are 6.72 at. %, 39 at. % and 51.9 at. %, respectively, at the eutectoid point. β-transus temperature can be decreased down to 300 °C from 882 °C when hydrogen concentration reaches 39 at. %. The hcp-α phase has 2 octahedral and 4 tetrahedral sites, and the bcc-β phase has 6 octahedral and 12 tetrahedral sites. Hydrogen atoms are predominantly dissolved in bcc-β phase because they prefer to occupy tetrahedral sites, so that hydrogen solubility in β phase is much higher (39 at. %) [108,116].

46
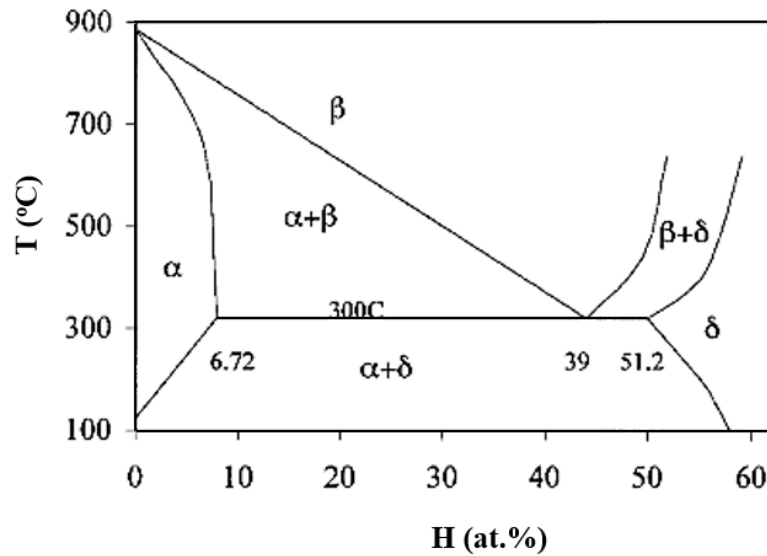
Figure 2.24. Binary phase diagram of Ti-H system [111].

The first phase diagram for Ti-6Al-4V-H system (Figure 2.25 (a)) has been derived by Kerr et al. [117] who have showed that β-transus temperature decreases with increasing hydrogen concentration by using metallographic examination and X-ray diffraction analysis (XRD). According to their study, a three phase region (α+β+δ) was seen below the β-transus temperature which was decreased from 1000 °C to 800 °C when the hydrogen concentration was 20 at. % and more. Additionally, β phase was found to decompose into α+δ phase when the hydrogen concentration is equal or higher than 15 at. % at 800 °C. Ilyan et al. [118], who agreed about hydrogen effect on β-transus temperature with Kerr et al., reported another phase diagram (Figure 2.25 (b)) for Ti-6Al-4V-H system. In this system, β-transus temperature decreases down to 700 °C when the hydrogen concentration is around 32 at. % and unlike the system suggested by Kerr et al., the decomposition of β into α+δ phase occurs at 250 °C (13 at. % hydrogen).

Recently, Qazi et al. [109] expanded the work of Kerr et al. by using XRD, optical-microscopy and transmission electron microscopy (TEM). According to Ti-6Al-4V-H phase diagram created by Qazi et al. (Figure 2.25 (c)), δ-hydride phase is stable at

47

two different phase regions, namely, β+δ and α+β+δ, above 15 at. % hydrogen concentration. Moreover, the diffusion coefficient of alloying elements in β phase is decreased by alloying of hydrogen, thus transformation kinetics of the β to α phase slows [108].
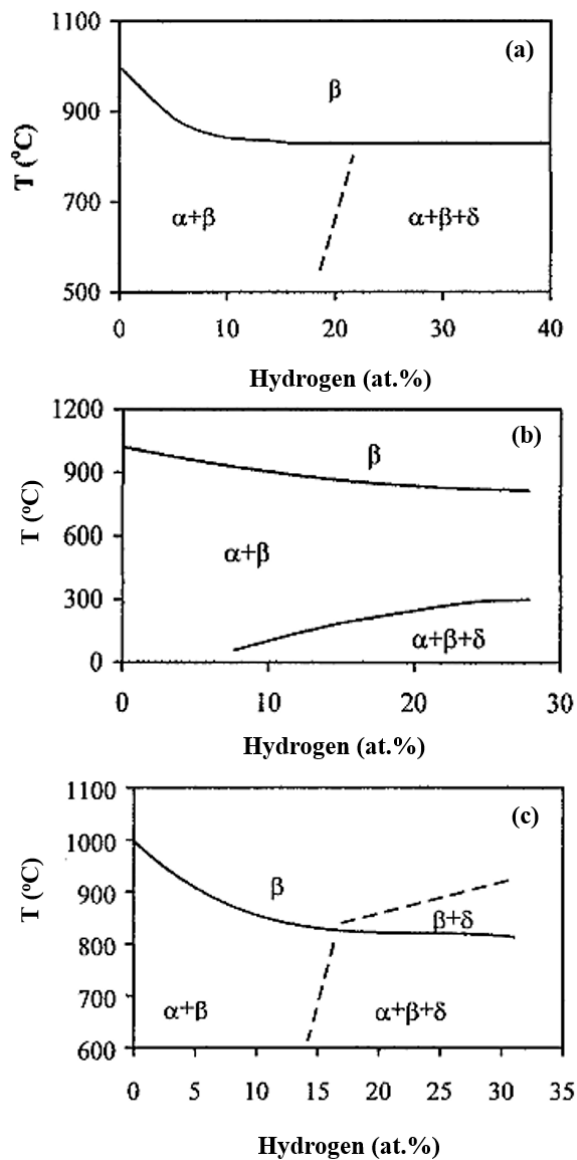
Figure 2.25. Ti-6Al-4V-H alloy phase diagrams suggested by (a) Kerr et al. [117], (b) Ilyn et al. [118] and Qazi et al. [109].

48

2.9.5. Microstructural Evolution during THP

The most common utilized THP consists of 4 steps (hydrogenation, β solution treatment, eutectoid decomposition, and dehydrogenation) as shown in Table 2.7 and Figure 2.26. Firstly, hydrogen is loaded in Ti-6Al-4V alloy under hydrogen or hydrogen + argon atmosphere at temperatures between 500-800 $^{\circ}$C. The lower solubility of hydrogen in α phase due to occupation of tetrahedral interstitial sites (α phase having 4 tetrahedral sites and β phase having 12 tetrahedral sites) causes δ hydride phase precipitation within the α grains. After hydrogenation step, β solution treatment is performed at higher temperatures with the same atmosphere, and α_H (hydrogen loaded α phase) and δ hydride phases dissolve in the β_H matrix (hydrogen loaded β phase) [107,119,120]. Subsequently, specimens are cooled to eutectoid decomposition temperature which is reported as 590 $^{\circ}$C by Fang et al. [119] and 600 $^{\circ}$C by Guitar et al. [121] in the same atmosphere. At this step, essential amount of β_H transforms to α_H and δ hydride phases, and small amount of β_H lefts due to the vanadium element. During the transformation, slow cooling rates cause larger α_H phase. At this step, duration of the eutectoid decomposition is important to obtain fine precipitates of α_H and δ hydride phases. Moreover, this transformation leads to microstructural refinement, and refining mechanism of the cast microstructure (schematically) is demonstrated in Figure 2.27, and also Figure 2.28 shows the refining mechanism of the SLM + HIPed microstructure. Finally, hydrogen is removed at the dehydrogenation step which is conducted under high vacuum. During dehydrogenation step, the δ hydride phase decomposes to fine α phase, and also α_H and β_H phases transforms to fine, equiaxed α and β phases [58,107,116,119,122] which lead to refinement of prior coarse microstructure.
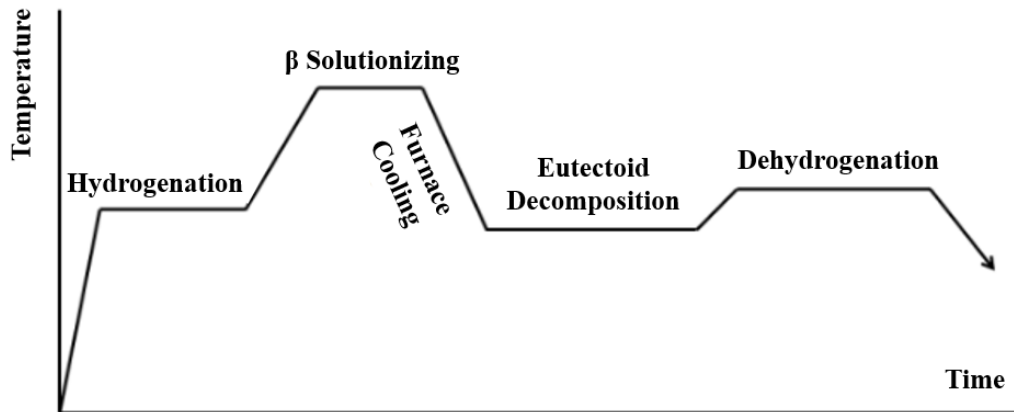
Figure 2.26. 4-step THP.

Recently, Bilgin et al. [94] developed 2-step THP which has only hydrogenation (650 °C for 1 h) and dehydrogenation (700 °C for 18 h) steps for Ti-6Al-4V alloy produced by SLM. They found that, as well as the microstructural refinement, 2-step THP inhibits the formation of grain boundary α phase which may reduce tensile properties and causes excessive grain growth.
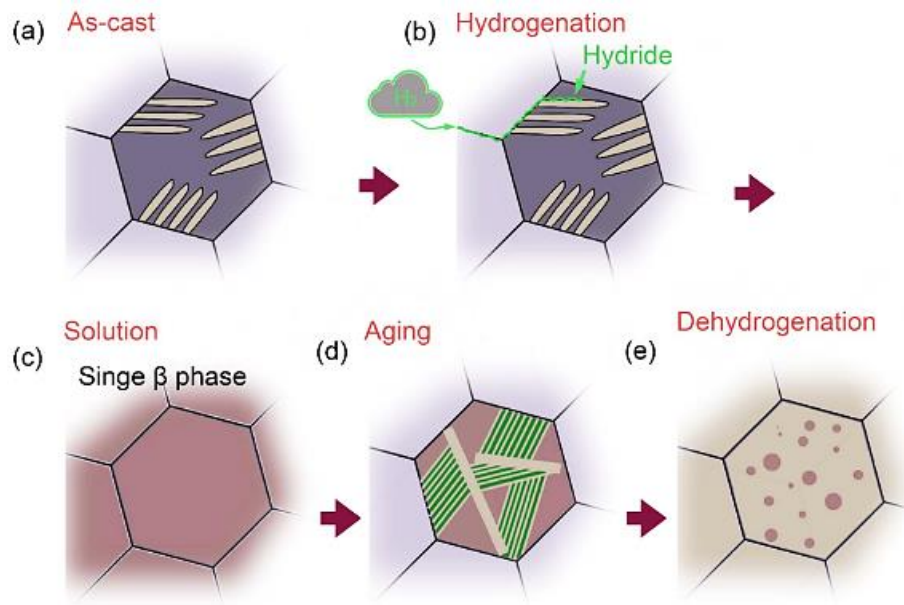
Figure 2.27. Microstructural evolution during THP (a) the as-cast microstructure, (b) hydride formation during hydrogenation, (c) β solution treatment, (d) refined microstructure at the eutectoid decomposition, and (e) removing of hydrogen at the dehydrogenation step [107].
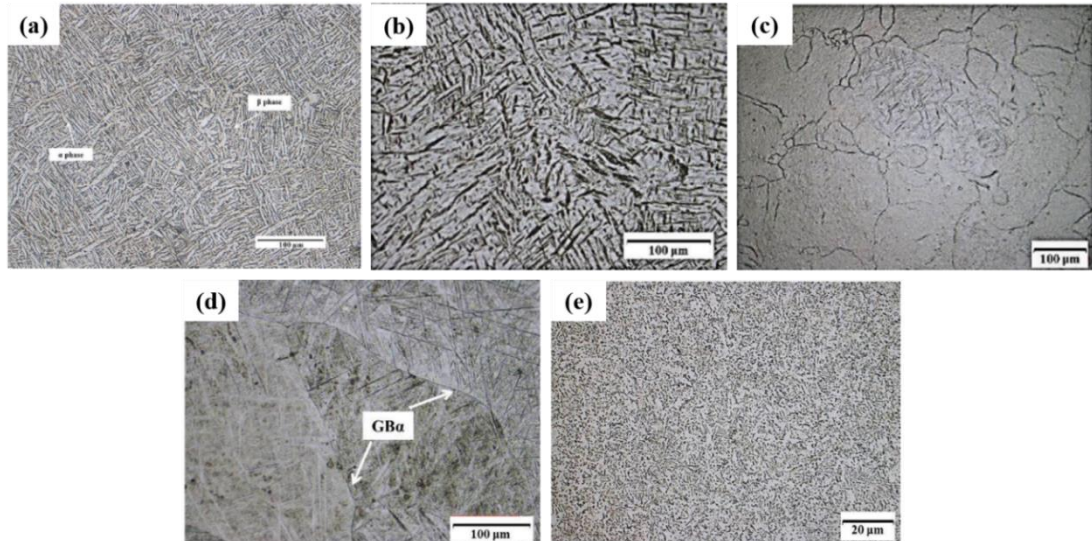
Figure 2.28. Microstructural evolution of Ti-6Al-4V alloy during THP (a) the SLM + HIPed microstructure, (b) hydride formation during hydrogenation (650 °C for 1 h), (c) β solution treatment (850 °C for 15 min), (d) refined microstructure at the eutectoid decomposition (600 °C for 3 h), and (e) removing of hydrogen at the dehydrogenation step (700 °C for 18 h) [58].

CHAPTER 3

EXPERIMENTAL PROCEDURE

3.1. Starting Materials

In the present study, Ti-6Al-4V alloy specimens were produced using gas atomized ARCAM Ti-6Al-4V alloy powders (grade 5) by ARCAM A2X Electron Beam Melting (EBM) machine at ASELSAN A.Ş. Defense System Technologies Division Mechanical Design Department, Turkey. In total, six batches of the specimens for various tests were fabricated in three different angles (90º, 45º and 0º). The tensile and fatigue test samples were built in dog bone shape, while the cylindrical bars were produced for optimization of heat treatment applied after additive manufacturing (Figure 3.1). Chemical composition of the starting alloy powders, which meets ASTM F2924-14 standard [123], and their particle size distribution are given in Table 3.1 and Figure 3.2, respectively. The size of the spherical alloy powders (Figure 3.3) were found to be distributed in the range of 41.6 and 215.6 μm with a mean diameter of 76.6 μm.
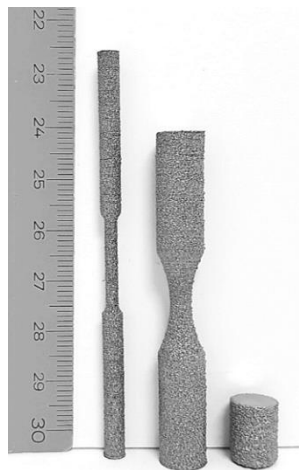
Figure 3.1. EBM produced Ti-6Al-4V alloy specimens.

Table 3.1. Elemental composition analysis of the alloy powders and ASTM F2924-14 Standard Specification defined for Ti-6Al-4V Alloy [105].

Element	Chemical Composition (wt. %)	
	ASTM F2924-14	Arcam Ti-6Al-4V alloy powder
Aluminum	5.50 to 6.75	6.5 ± 0.3
Vanadium	3.50 to 4.50	3.9 ± 0.3
Iron	< 0.30	0.19 ± 0.01
Titanium	Balance	Balance
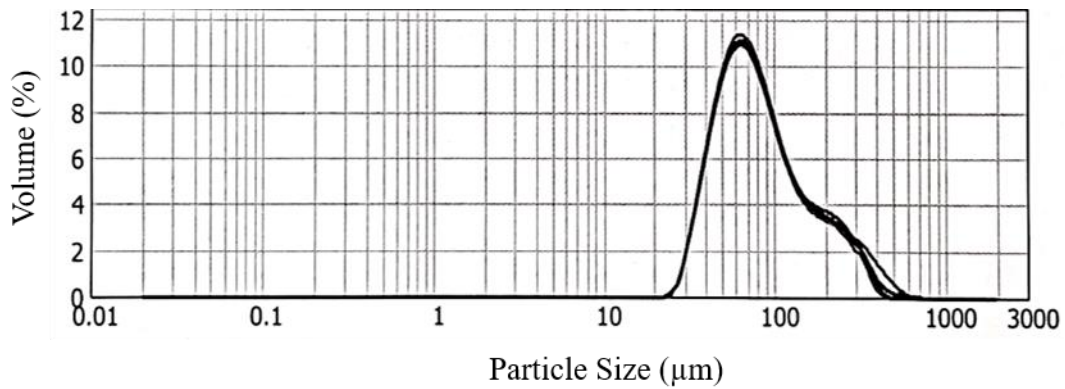
Figure 3.2. Particle size distribution of Arcam Ti-6Al-4V alloy powders.
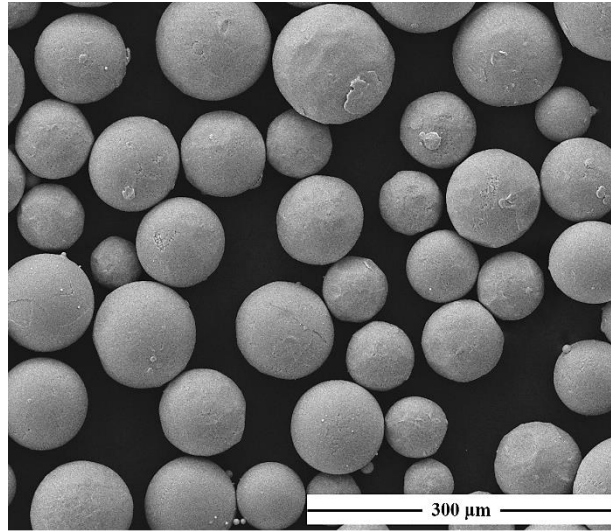
Figure 3.3. SEM images of Ti-6Al-4V alloy powders.

3.2. Experimental Techniques

Ti-6Al-4V alloy samples were produced via EBM. By keeping all the production variables constant, the effects of both building direction and post processing on the mechanical properties and microstructural evolution were investigated. The relationship between building direction and scanning direction for various samples is shown schematically in Figure 3.4. Among the post processes, surface treatment by acid etching was applied to reduce surface roughness and for alleviating the notch effect. On the other hand, thermo-hydrogen processing (THP), which is based on alloying and dealloying with hydrogen, and post annealing treatment around α/β transus temperature were done to reveal the effect of various post processes on the microstructural development and mechanical properties of Ti-6Al-4V alloy specimens. The details of the production variables and applied post processes, and characterization techniques are shown in Table 3.2.
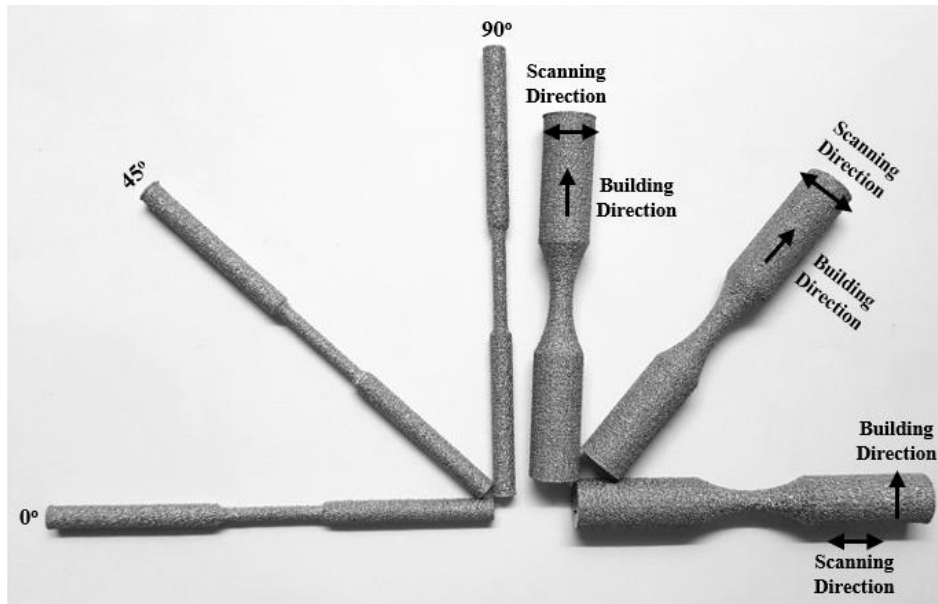
Figure 3.4. As-produced samples produced in different angles; 90º, 45º and 0º.

Table 3.2. Summary of the applied processes and characterization techniques.

Build direction	Surface Treatment (etching)	THP	Annealing	Density Measurement	Microstructural examination	Hardness Test	Tensile Test	Fatigue Test	Phase Analysis (XRD)	Texture Analysis (EBSD)
0º	-	-	-	+	+	+	+	+	+	+
45º	-	-	-	+	+	+	+	+	+	+
90º	+	+	+	+	+	+	+	+	+	+

3.2.1. Thermo-Hydrogen Processing (THP)

Thermo-hydrogen processing has attracted increasing research interest as it is an effective way to modify microstructure and enhance the mechanical properties of titanium alloys without deformation and heat treatment which include recovery and recrystallization. Several types of THP have been used, in general, 4-step THP (hydrogenation, β solution treatment, eutectoid decomposition and dehydrogenation) is commonly utilized for titanium alloys [119].

In the present study, 4-step THP was modified to prevent possible grain coarsening during β solution treatment and eutectoid decomposition steps and 2-step (hydrogenation and dehydrogenation steps below β-transus temperature) THP shown in Figure 3.5 was used as in the study of Bilgin et al. [94].
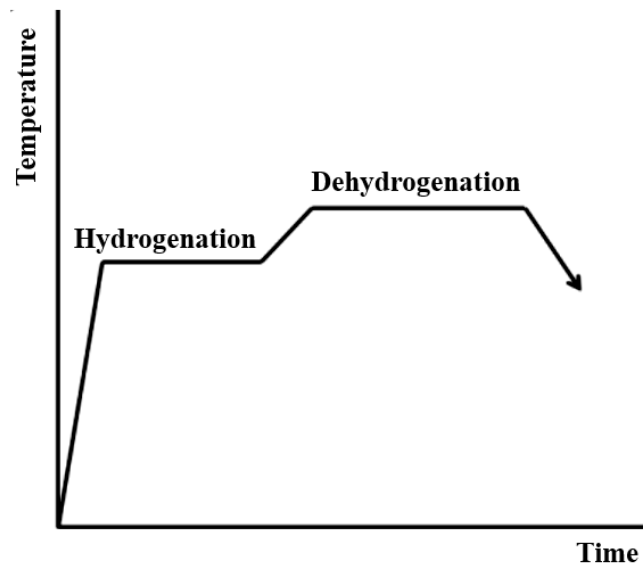
Figure 3.5. Modified 2-step THP.

3.2.1.1. Sample Preparation for THP

Before THP, EBM produced Ti-6Al-4V alloy samples (cylindrical, tensile and fatigue test samples) in 90°, 45° and 0° angles were cleaned in an ultrasonic bath by soaking in acetone for 10 minutes and cleaning with ethanol for 10 minutes. Cleaning in different solutions was finalized by drying in oven at 40 °C for 1 h.

3.2.1.2. Hydrogenation Process

In the first step of THP, samples were loaded with hydrogen to allow δ (TiH_2) phase formation which is the basis for microstructural refinement in THP process. Firstly, cleaned and dried specimens inside an aluminum boat were placed into a horizontal furnace at room temperature. Subsequently, the furnace was vacuumed (about $2x10^{-4}$

torr) with the help of turbo-molecular vacuum pump. Next, the furnace was filled with high purity argon gas (Ar > 99.999 %). After two degassing and purging cycles, the furnace was heated under flowing high purity hydrogen (0.5 lt/min) gas environment up to 650 °C, which was previously determined as optimum hydrogenation temperature for Ti-6Al-4V alloy by Bilgin et al. [58]. When the furnace temperature reached to 650 °C, specimens were held for 1 hour under hydrogen gas atmosphere. The effect of hydrogen loading on the microstructure evolution and mechanical properties, two groups of samples were hydrogenated. First group of samples were cooled directly down to room temperature naturally (10 °C/min) under the high purity hydrogen gas atmosphere. On the other hand, the second group of samples were directly heated to dehydrogenation temperature after they had been hydrogenated as explained in the following part.

3.2.1.3. Dehydrogenation Process

The hydrogen reaction with titanium is reversible, so that hydrogen can be removed at elevated temperatures with increased diffusion rate [58,108]. In this step, the aim was to remove hydrogen in hydrogenated samples to eliminate hydrogen embrittlement and to allow phase transformation from δ phase (formed during hydrogenation) to fine α phase to get finer microstructure composed of $\alpha+\beta$ phases. In addition to phase transformation, dehydrogenation at elevated temperature was used to reduce residual stress of the specimens formed during cooling stage of the additive manufacturing. For this purpose, after hydrogenation of the samples as described above, the samples were directly heated to 700 °C under flowing hydrogen gas, and then they were kept under high vacuum (approximately 2×10^{-4} torr) for 18 hours which was also optimized by Bilgin et al. [58]. In the final step, the furnace was switch off and the samples were cooled down to room temperature under high vacuum.

3.2.2. Conventional Annealing Process

Conventional annealing process is a traditional post heat treatment process usually applied to additive manufactured parts with the aim of eliminating residual stress and

increasing the ductility. In the present study, conventional annealing heat treatment process was conducted to compare and contrast its effects on microstructure, mechanical properties and texture of the samples with respect to THP.

In this step, same cleaning and drying processes were applied to as-produced samples as in the samples used in hydrogenation-dehydrogenation steps. Then, samples were placed into the horizontal furnace at room temperature. Subsequently, the furnace was heated under flowing high purity argon gas (0.5 lt/min) environment up to 840 $^{\circ}$C at which they were held for 2 hours under argon gas atmosphere. Afterwards, the furnace was switched-off, and the samples cooled to down to room temperature naturally (10 $^{\circ}$C/min) under the argon gas atmosphere.

3.2.3. Surface Treatment with Hydrofluoric Acid

EBM technique results in specimen with high surface roughness due to presence of partially melted powders stuck on the sample's surface. To decrease the surface roughness, EBM produced samples were chemically polished in 1% HF acid solution for 1, 3, 5, 15, 30 and 50 minutes. After that, the samples were ultrasonically cleaned with distilled water for 10 minutes and then they were soaked in ethanol for 10 minutes. After ultrasonic cleaning, specimens were dried in an oven at 40 $^{\circ}$C for 1 h.

3.3. Experimental Set-Up

All of the heat treatments (THP and conventional annealing) were performed in the experimental set-up shown in Figure 3.6. In the furnace, 1000 mm long quartz tube having 45 mm internal and 48 mm outer diameters was used to conduct successful heat treatment experiments and alumina crucible was used to place the samples inside the quartz tube. The furnace was sealed using flanges at both sides of the tube, which contained nitrile O-rings. The temperature inside the horizontal furnace was measured with the help of K-type thermocouple. Additionally, hydrogen and argon gas flow rates were controlled with the help of digital flow meters. On the other hand, high vacuum level in the furnace was maintained by a turbo-molecular vacuum pump (Nano-Vak, Turkey).

(1) Hydrogen and Argon Gases
(2) Gas Inlet Valve
(3) RGA
(4) Flow Meter
(5) Gas Outlet
(6) Vacuum Pump
(7) Vacuum Gauge
(8) Cooling Fan
(9) Furnace
(10) Quartz Tube
(11) Sample Holder Enclosure
(12) Thermocouple
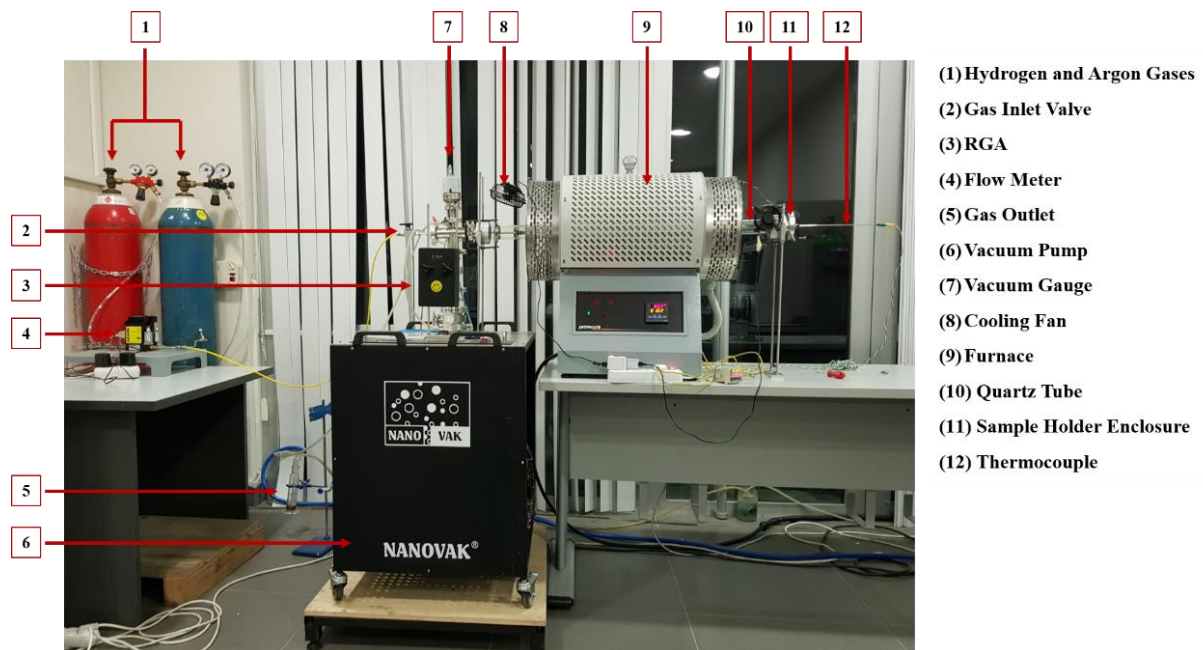
Figure 3.6. Experimental set-up for heat treatments.

3.4. Characterization Techniques

3.4.1. Particle Size

Particle size analyses of the ARCAM Ti-6Al-4V powders (grade 5) was done with Malvern Mastersizer 2000 using red light (Helium neon laser source) for coarser particles and blue light (solid-state light source) for finer particles size measurement.

3.4.2. Chemical Composition Analysis

In order to determine chemical composition of the ARCAM Ti-6Al-4V powders (grade 5) and as-produced Ti-6Al-4V alloy parts, inductively coupled plasma optical emission spectroscopy (ICP-OES) (Perkin Elmer Optima 4300DV) was utilized. The average of three measurements was taken to calculate the average composition.

3.4.3. O, H, C, N Contents

Hydrogen, oxygen and nitrogen contents of EBM produced and post-processed Ti-6Al-4V alloy samples were measured with LECO TCH 600 Simultaneous N, O, H Determinator and C content was detected using LECO CS 230 C, S Determinator. In order to obtain accurate results from the analysis, three measurements were done for each specimen.

3.4.4. X-Ray Diffraction Analysis (XRD)

Phase constituents of as-produced, hydrogenated, dehydrogenated and annealed specimens were measured by X-ray diffraction (XRD) analysis using a conventional X-ray diffractometer (Rigaku D/Max 2200/PC, Rigaku Corporation, Tokyo, Japan) by supplying Cu-Kα radiation at 40 kV via continuous scanning between 30° and 80° 2θ angles with a scan speed of 0.5 °/min.

3.4.5. Microstructural Analysis

For microstructural analysis, specimens were cut at different directions to examine their cross-sections at transverse and longitudinal directions. Initially, samples were mechanically ground using SiC papers up to 2500 grit size to obtain smoother surfaces. After that, they were polished using diamond suspension (3 μm) and etched with Kroll's Reagent (2 ml HF + 8 ml HNO_3 + 92 ml H_2O) for 20-40 seconds. Finally, specimens were rinsed with water and ethanol, and dried with hot air. In addition to this, for Electron Back Scatter Diffraction (EBSD) analysis, specimens with 1 cm^2 cross-sectional area were electropolished using A3 electrolyte (600 ml methanol (100%) + 340 ml butioxyethanol (100%) + 60 ml perchloric acid (70%)) at 50 V for 25 seconds. After electropolishing, samples were firstly rinsed with ethanol, subsequently, they were washed with water and ethanol, and then dried with air.

In order to obtain macro images of the samples, Olympus Stereo Microscope was used. Optical microstructural examination was carried out using Huvitz HDS-5800 digital micrograph and Scanning Electron Microscope studies were performed using FEI 430 Nano Scanning Electron Microscope equipped with an energy dispersive X-ray spectroscopy (EDS) analysis system. In addition to this, EBSD analysis was done with ZEISS Merlin Scanning Electron Microscope.

3.4.6. Mechanical Testing

3.4.6.1. Microhardness Test

The microhardness tests were carried out with Shimadzu HMV-2T microhardness device (1000 g load for 20 seconds) to determine Vickers hardness values of the samples. 10 measurements were performed for each cross-section in every sample.

3.4.6.2. Tensile Test

100 kN capacity Instron 5582 Universal Testing Machine equipped with video extensometer was used to determine the stress-strain behaviors of the EBM produced and post-processed Ti-6Al-4V alloy samples (dimensions shown in Figure 3.7 (a)) at a constant crosshead-speed of 0.5 mm/min.

3.4.6.3. Fatigue Test

SM 1090 Rotating Fatigue Machine (dOtek, Turkey) was used to conduct rotating-bending fatigue tests at different stresses (170-350 MPa) (f= 60 Hz, R= -1) for the EBM produced Ti-6Al-4V alloy samples (Figure 3.7 (b)).
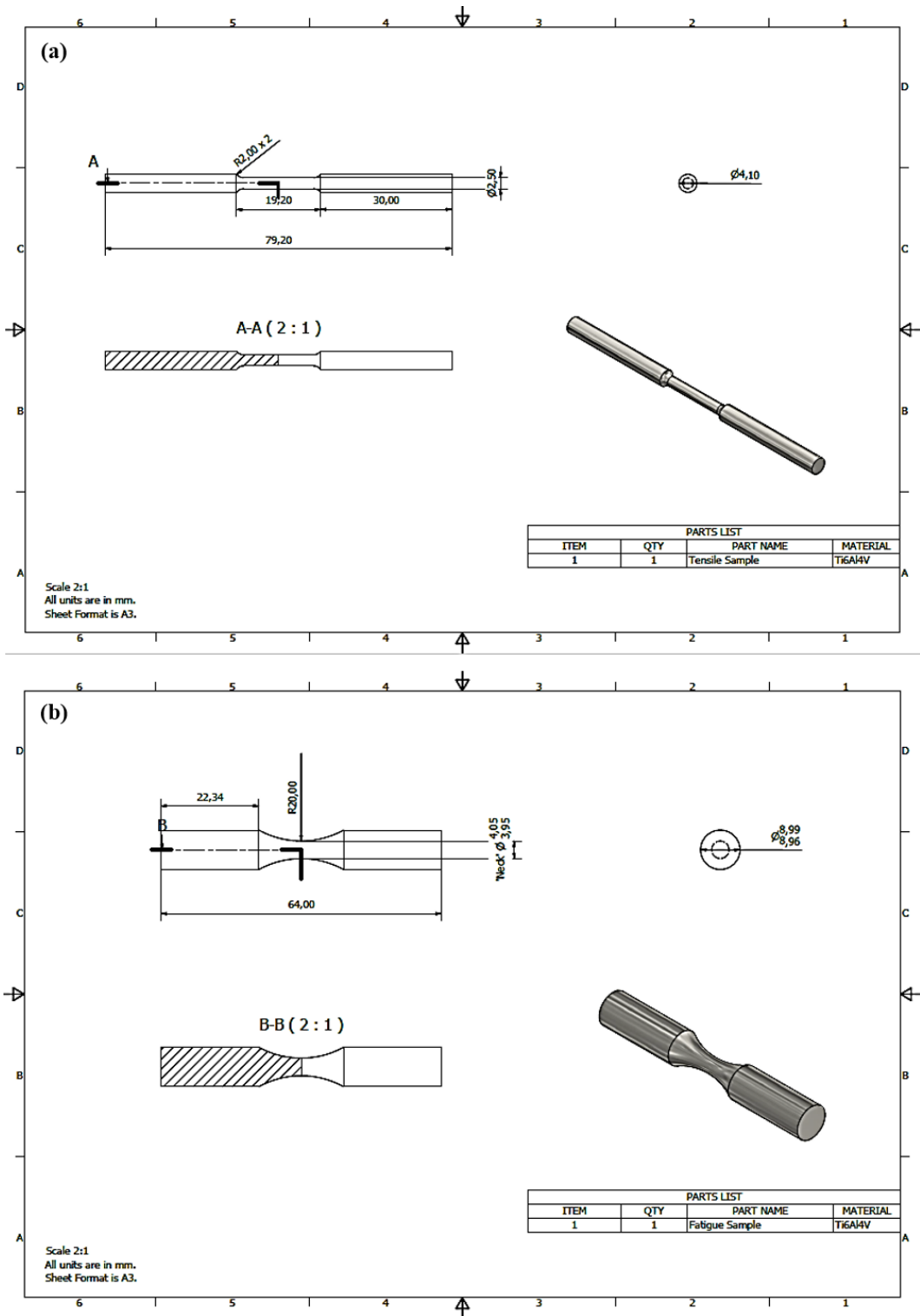
Figure 3.7. Technical drawings of (a) tensile test and (b) fatigue test specimens.

3.4.7. Density Measurement

The density and porosity values of the as-produced samples were measured according to Archimedes' principle using Xylol solution ($CH_3C_6H_4CH_3$) by PRECISA XB220A balance equipped with density determination kit. Firstly, the samples were weighed in air and then, immersed into xylol solution for 1 day in order to allow penetration of xylol into samples. After that, samples were weighed in xylol solution and finally, they were taken out of the solution and the weight of xylol impregnated samples were measured in air. According to equations 3.1-3.3, density and porosity values of the samples were calculated.

$$V_{specimen} = \frac{m_{(a,x)} - m_{(x,x)}}{\rho_{xylol}} \qquad (3.1)$$

$$\rho_{specimen} = \frac{m_{(a)}}{V_{specimen}} \qquad (3.2)$$

$$P_{total}(\%) = 100 - \left(\frac{\rho_{specimen}}{\rho_{Ti6Al4V}} x100\right) \qquad (3.3)$$

Where,

ρ_{xylol}: density of xylol (0.861 g/cm^3),

$\rho_{Ti6Al4V}$: density of the wrought Ti-6Al-4V alloy (4.43 g/cm^3),

$m_{(a)}$: mass of the specimen in air,

$m_{(a,x)}$: mass of xylol impregnated specimen in air,

$m_{(x,x)}$: mass of xylol impregnated specimen in xylol solution,

P_{total} (%): percentage of total porosity.

CHAPTER 4

RESULTS AND DISCUSSION

In this section, surface morphology, density, chemical composition, structural and microstructural analysis and mechanical properties of Ti-6Al-4V alloy produced by EBM are presented. Firstly, the effects of building directions and acid treatment on the surface morphology were examined. Next, the effects of heat treatments, namely, modified 2-step THP and conventional annealing heat treatment, on the microstructure and mechanical properties of EBM produced Ti-6Al-4V alloys were discussed.

4.1. Surface Morphology

The surface roughness of the Ti-6Al-4V alloy produced by EBM is relatively high compared to wrought Ti-6Al-4V alloys due to presence of partially melted powders on the surface. In order to minimize the surface roughness of the specimens produced by EBM, process parameters should be optimized and/or post processing should be applied. Surface treatments (chemical polishing, machining and etc.) are commonly used to reduce the surface roughness of the EBM produced samples. Wysocki et al. [104] reported that chemical polishing with different acids can be used for titanium scaffolds produced by SLM.

4.1.1. Effect of Building Direction

Surface morphologies of Ti-6Al-4V alloy specimens produced at 90°, 45° and 0° are presented in Figure 4.1. All of the specimens had partially sintered powders on the surfaces; however, distribution and density of the partially sintered powders was observed to be dependent on the production angle. The specimens produced at 90° possessed the highest surface roughness with clear appearance of spherical particles stuck on the surface. On the other hand, less amount of partially melted particles were observed on the surface of samples produced at 45°. However, the surface roughness of the specimens produced at 0° was not homogenous such that the surface, which was

lastly exposed to electron beam, had lower surface roughness with smoother surface. It was believed that the high energy input for relatively longer durations due to the horizontal scanning caused nearly complete melting of powders, thereby, resulting in lower surface roughness.
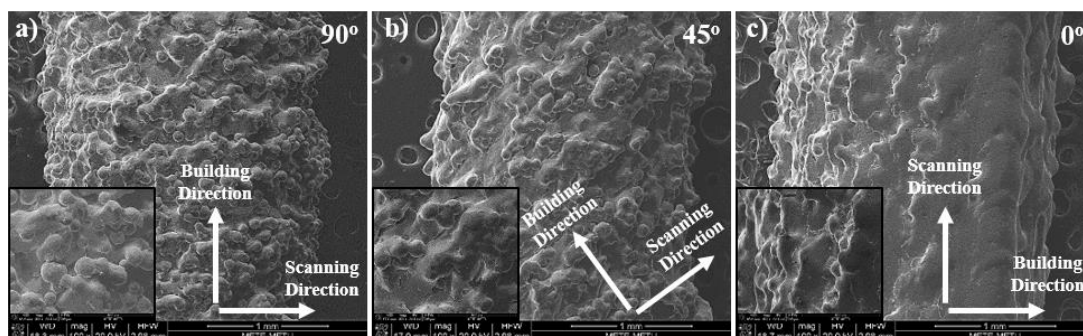
Figure 4.1. Surface morphologies of Ti-6Al-4V alloy specimens produced by EBM at (a) 90°, (b) 45°, and (c) 0°.

4.1.2. Effect of Surface Treatment

High surface roughness in additively manufactured parts deteriorates the mechanical properties due to notch effect created by partially melted powders on the surface. Therefore, in this study, acid treatment was applied to reduce surface roughness by chemical polishing and the specimens produced at 90° were chosen for acid treatment since they had the highest surface roughness. Cylindrical samples were immersed in 1% HF acid solution (balanced with deionized water) for 1, 3, 5, 15, 30 and 50 minutes to reduce the surface roughness (Figure 4.2). Unfortunately, the surface roughness of the samples after treatment couldn't be measured. Therefore, relative comparison was made based on the surface images taken by SEM. Longer exposure to acid solution was observed to reduce surface roughness by dissolution of partially sintered powders on the surface. Although etching time was effective on reducing the surface roughness, higher mass loss occurred in the samples for prolonged exposure to acid solution.

66

Therefore, 30 minutes etching was chosen as the optimal chemical polishing time according to SEM images (Figure 4.2 (e)) and mass loss measurements. The mass losses were 1.48 % $\pm$ 0.02 for 30 minutes etching, and 2.40 % $\pm$ 0.13 for 50 minutes etching.
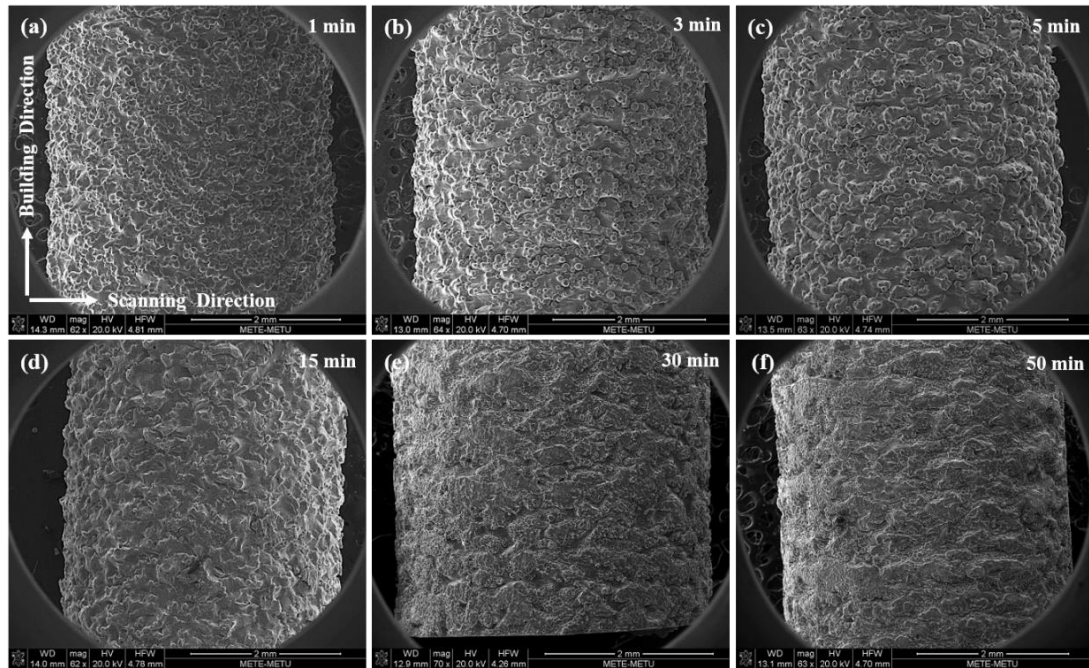
Figure 4.2. SEM images of the samples' surfaces after chemical polishing in 1% HF solution bath for (a) 1 min, (b) 3 min, (c) 5 min, (d) 15 min, (e) 30 min and (f) 50 min.

4.2. Density Measurements

Density measurements after additive manufacturing like EBM and SLM are commonly used to test whether production techniques yield high density products or not. Sometimes density measurements are conducted to determine the total porosity as in the samples produced by SLS technique, which aims to obtain porous or functionally graded samples. There are several density or porosity measurement

techniques such as Archimedes method, microscopic cross-sectional examination, computer tomography and X-ray scanning techniques [95,124–127].

In this study, Archimedes method was used to measure the densities of the specimens produced by EBM due to its simplicity.

4.2.1. Effect of Building Angle

The density, relative density and porosity of the EBM produced specimens at different angles (90º, 45º, and 0º) are shown in Table 4.1. According to literature, EBM technique enables the production of specimens with more than 99 % relative densities. However, the average relative densities of the produced specimens were observed to change between 97.80 % and 98.73 %, which were below 99 %. The difference between the densities of specimens in the current study and literature was attributed to production variables and density measurement technique used in this study. Since the samples' surfaces were highly rough and containing partially sintered powders, more xylol solution penetrated on the rough surface and caused lower density measurement in the present study. On the other hand, process parameters and location of the specimens on the build platform also affect the porosity and density of the produced specimens. Galarraga et al. [99] reported that the porosity of the Ti-6Al-4V ELI alloy produced by EBM is greater in the center of the build platform when compared to those produced at the edge of the build platform (0.25 % porosity for center and 0.09 % porosity for edge). When the building directions of the samples are compared, the relative density of the sample produced 45º was the lowest among the three samples produced at different angles. Exposure of the powder layers with electron beam at each scan has direct effect on the final density. If the exposed area in each scan increases as in the sample produced at 0º, the density of the sample is expected to increase because of higher heat input. Apart from the production angle and the location of the part in building platform, re-usage of powders may also cause lower density because of insufficient melting due to presence of agglomerated powders which are produced at each production cycle.

68

Table 4.1. The density, relative density and porosity values of the EBM produced specimens in 90°, 45°, and 0°.

Sample Angle	Density (g/cm^3)	Relative Density (%)	Porosity (%)
90°	4.343 $\pm$ 0.031	98.04 $\pm$ 0.69	1.96 $\pm$ 0.69
45°	4.335 $\pm$ 0.003	97.86 $\pm$ 0.06	2.14 $\pm$ 0.06
0°	4.345 $\pm$ 0.029	98.07 $\pm$ 0.63	1.93 $\pm$ 0.63

4.2.2. Effect of Surface Treatment

To see the effect of surface roughness on the density measurement, samples' densities were also measured after they have been polished chemically. All other variables were kept constant and the density measurement was conducted on sample produced at 90°. The density, relative density and porosity of the sample before and after chemical polishing are shown in Table 4.2.

The relative density of the specimens was observed to increase from 98.04 % to 99.01 % after surface polishing. Rough surfaces containing partially melted powders on the surface (Figure 4.1) probably caused penetration of more xylol solution on the groovy surface, which caused misleading results. Therefore, the actual part density should be measured after chemical polishing or machining of the EBM produced samples.

Table 4.2. The density, relative density and porosity values of the as-produced and chemically polished specimens in 90°.

Sample	Density (g/cm^3)	Relative Density (%)	Porosity (%)
90°-As-produced	4.343 $\pm$ 0.031	98.04 $\pm$ 0.70	1.96 $\pm$ 0.70
90°-Chemically polished	4.386 $\pm$ 0.002	99.01 $\pm$ 0.05	0.99 $\pm$ 0.05

4.3. Chemical Composition

Titanium and its alloys' properties are highly sensitive to interstitial elements (H, N, O, H) contents. Among them, oxygen has the highest influence on mechanical properties, and it increases the strength; however, the sample's ductility decreases when the dissolved oxygen increases in the sample. The final chemical composition of the sample depends on the additive production technique used. For example, EBM technique yields samples with lower oxygen contents since it uses vacuum during production. Therefore, additively manufactured titanium alloys chemical composition should be compatible with standard (ASTM F2924-14) since each technique may result in different composition. Table 4.3 presents the elemental composition of Ti-6Al-4V alloy defined by ASTM F2924, and produced by EBM in the current study. As can be seen, EBM produced Ti-6Al-4V alloy in the current study meets the chemical requirements defined by the standard.

Table 4.3. Elemental composition analysis of the EBM produced Ti-6Al-4V alloy and ASTM F2924-14 Standard Specification defined for Ti-6Al-4V Alloy [105].

Element	Chemical Composition (wt.%)	
	ASTM F2924-14	EBM produced alloy
Aluminum	5.50 to 6.75	5.8 ± 0.1
Vanadium	3.50 to 4.50	3.9 ± 0.1
Iron	< 0.30	0.19 ± 0.01
Oxygen	< 0.20	0.0027
Carbon	< 0.08	0.01
Hydrogen	< 0.015	0.0014
Titanium	Balance	Balance

4.3.1. Hydrogen Contents of Hydrogenated and Dehydrogenated Specimens

Hydrogenation and dehydrogenation heat treatments were applied to Ti-6Al-4V alloy after production by EBM as a thermochemical treatment so as to refine microstructure. Hydrogenation process was conducted under high purity hydrogen atmosphere at 650 °C for 1 h, while dehydrogenation process was performed under high vacuum (about 2×10^{-4} torr) at 700 °C for 18 h. For thermochemical process, Ti-6Al-4V alloy produced at 90° was chosen. The starting sample's hydrogen content (0.0014 wt. %) was increased to 1.97 wt. % as a result of hydrogenation treatment. Dehydrogenation under high vacuum decreased hydrogen down to 0.0008 wt. %, which was well below the maximum value defined by ASTM F2924-14 (Table 4.4).

Table 4.4. Hydrogen concentrations of the as-produced, hydrogenated and dehydrogenated specimens.

Sample	Hydrogen Concentration (wt.%)
90° as-produced	0.0014
90° hydrogenated	1.97
90° dehydrogenated	0.0008

Loading of Ti-alloy with the highest hydrogen level during hydrogenation is critical to obtain δ (TiH$_2$) phase, which turns into fine α-phase during dehydrogenation and plays a critical role in microstructural refinement. The critical hydrogen content for the formation of δ phase is known to be 0.385 wt. %, below which there is no δ phase formation [109]. Hydrogen solubility of Ti-6Al-4V alloy depends on temperature. Bilgin et al. [94] conducted hydrogenation process for SLM produced Ti-6Al-4V alloy parts at different temperatures such as 550, 600, 650, 700, 750, 800 and 850 °C. According to their study, hydrogen concentration did not change until 650 °C, and maximum hydrogen level, 1.19 wt. %, was observed after holding at 650 °C for 1 h.

However, hydrogen concentration of the samples decreased when the temperature was increased. Therefore, the temperature for hydrogenation process was chosen as 650 ºC in the present study and about 1.97 wt. % hydrogen was loaded in the alloy. In addition, recently, Pushilina et al. [115] investigated that hydrogen-induced phase transformation and microstructure evolution for EBM produced Ti-6Al-4V alloy parts at different hydrogen concentrations such as 0.29, 0.58 and 0.90 wt. % adjusted by gas reaction controller.

The hydrogen concentration of EBM produced Ti-6Al-4V alloy parts has to be lower than 0.015 wt. % according to ASTM F2924 standard to avoid the hydrogen embrittlement. Moreover, as mentioned previously, the transformation from δ hydride phase to fine α phase is important for microstructural refinement. Transformation of δ hydride phase to fine α phase is possible when the hydrogen concentration is minimized by dehydrogenation.

4.4. XRD Analysis

In this section, phase constituents of the specimens produced at different angles and heat treated at different conditions are presented to reveal the effect of different production angles and post-processing on phase evolution in Ti-6Al-4V alloy.

4.4.1. Specimens Produced at Different Angles

The phases present in Ti-6Al-4V alloy specimens produced by EBM at 90º, 45º and 0º angles are given in Figure 4.3. There was no distinct difference between the specimens and all them were observed to contain equilibrium phases composed of hcp-α and bcc-β formed at relatively slower cooling rates during production.
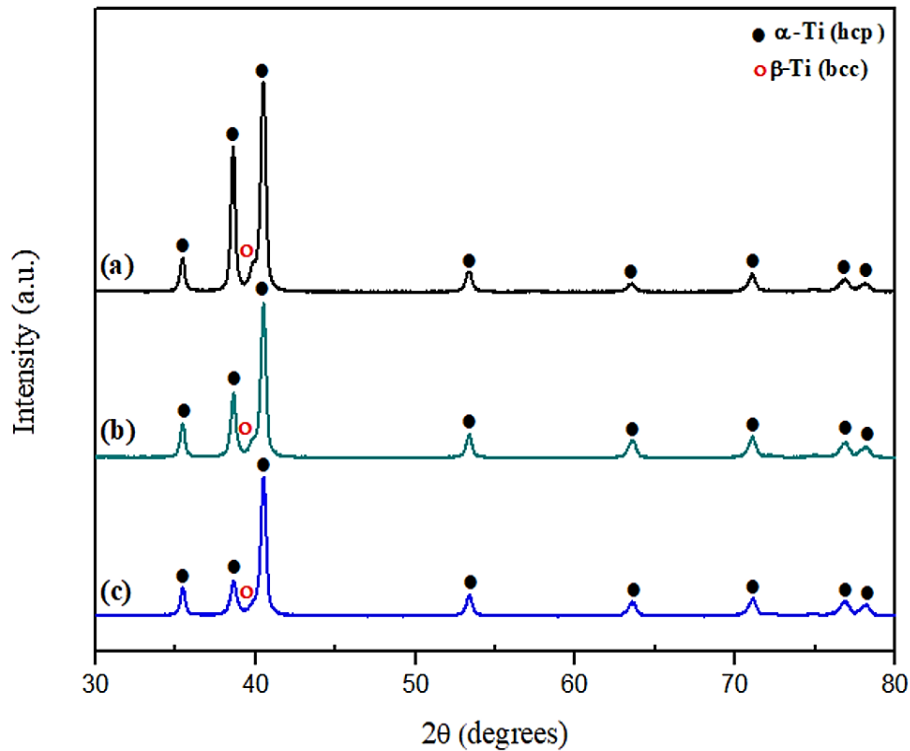
Figure 4.3. The XRD patterns of as-produced Ti-6Al-4V alloy specimens produced by EBM at (a) 90°, (b) 45° and (c) 0°.

4.4.2. Heat Treated Specimens

The phase constituents of as-produced samples at 90° were compared with those heat treated at different conditions to reveal the effect of post annealing, hydrogenation and dehydrogenation treatments. The XRD patterns of as-produced and heat treated Ti-6Al-4V alloy specimens are given in Figure 4.4. The as-produced specimen had only hcp-α and bcc-β phases.

Although post annealing heat treatment conducted at 840 °C for 2h did not alter the phases present in the sample, hydrogenation-dehydrogenation changed the phase constitution in the samples. Annealing only shifted the phase angles slightly to the right. In addition to this, the XRD patterns of the annealed specimen was relatively sharper than that of as-produced specimen mainly due to the grain coarsening effect

of annealing. The hydrogenation process caused formation of δ (TiH$_2$) as expected (Figure 4.4 (c)). The formation of δ (TiH$_2$) phase peak broadening of α phase peaks due to overlap of α and δ phases [106].
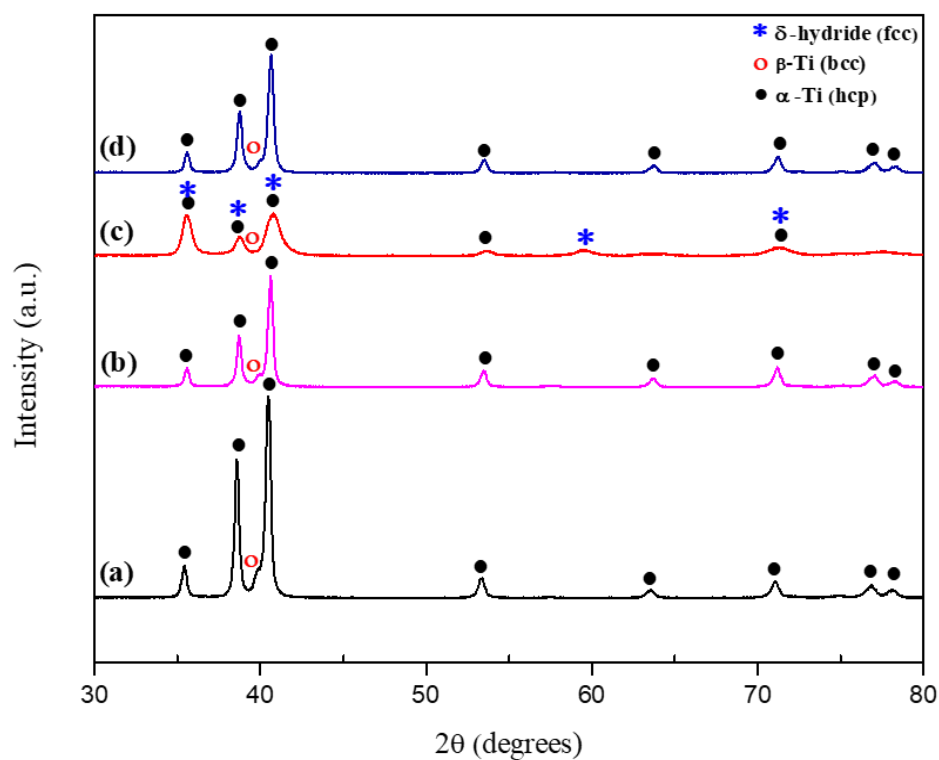
Figure 4.4. The XRD patterns of Ti-6Al-4V alloy specimens produced by EBM at 90º, (a) as-produced sample, (b) annealed at 840 ºC for 2 h, (c) hydrogenated at 650 ºC for 1 h and (d) dehydrogenated at 700 ºC for 18h after hydrogenation.

Additionally, diffraction peaks of the hydrogenated specimen slightly shifted to the right (the most intense peak is around 40.79º), and also some α phase peaks (at 2θ angles of 63.48º, 76.81º and 78.11º) were diminished.

The dehydrogenation process, on the other hand, contained peaks of hcp-α and bcc-β phase like as-produced and annealed samples, and δ phase disappeared possibly due to transformation of δ phase to hcp-α phase since hydrogen is lowered below 0.385 wt. % by keeping the specimens under high vacuum. Although XRD patterns displayed the existence and transformation of δ phase, which was also supported by LECO analysis, detailed TEM studies should be done in order to verify the existence of δ phase.

4.5. Microstructural Examination

Microstructural examinations of Ti-6Al-4V alloys produced at different angles and post-heat treated in different conditions were conducted on cylindrical samples (Ø 10 mm) in transverse and longitudinal directions. Microstructural analysis was carried out by using optical microscope, Scanning Electron Microscope (SEM) and Electron Back Scatter Diffraction (EBSD) techniques which was also used for texture analysis. Before conducting the microstructural examination at higher magnification, the samples were examined under stereo microscope to reveal the relationship between grain orientation, scanning direction and building direction. Building and scanning directions (red lines) of the specimens are shown in Figure 4.5. In all of the samples, elongated grains were observed to form parallel to building direction and perpendicular to scanning direction.
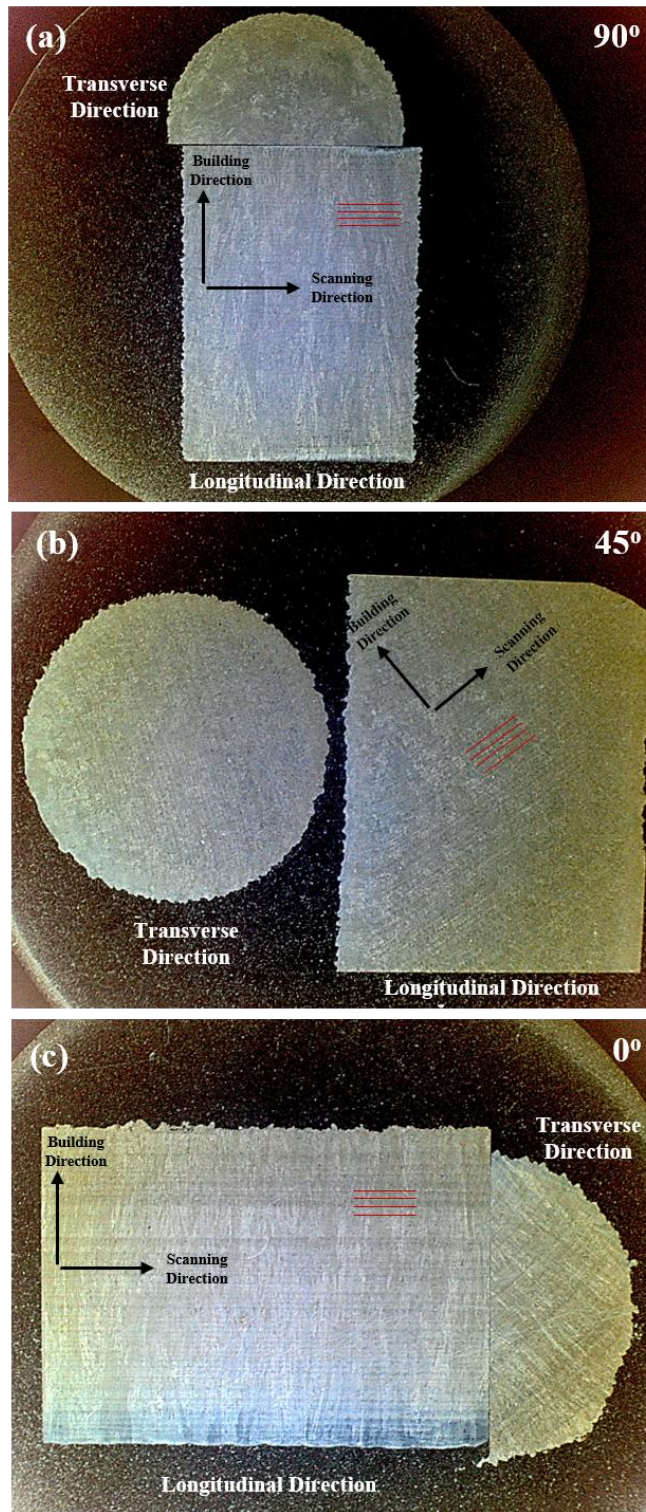
Figure 4.5. Stereo microscope images of the as-produced specimens at different angles: (a) 90º, (b) 45º and (c) 0º.

4.5.1. Specimens Produced at Different Angles

In this section, underlying microstructures of the samples produced at 90°, 45° and 0° have been examined. Moreover, microstructural change in specimen produced at 0° was examined along three different locations, namely, bottom, middle and top portion of the specimen. EBSD analysis was also conducted to reveal the effect of building angle on texture formation. The optical micrographs taken from longitudinal directions are given in Figures 4.6 and 4.7, and those taken from transverse directions are shown in Figures 4.8 and 4.9. According to optical micrographs, the microstructures of the as-produced specimens consisted of α phase (bright regions) and β phase (dark regions) which were also verified by XRD analysis (Figure 4.3). The as-produced alloys had basket-weave (also called Widmanstätten) microstructure containing columnar grains of prior β phase grown parallel to the building direction in which α plates arranged in Widmanstätten structure (Figures 4.6 and 4.7) similar to previous studies [60,83,99,128]. Moreover, the primary α phase was detected along the primary β-grain boundaries of all samples produced in three different angles (90°, 45°, 0°). It has also been determined that the thickness of primary α phase changed in each sample produced at different angles and also it changed in different locations of the same samples. Primary α phase was thickest in 0° specimen, while it was thinnest in specimen produced at 90°. The difference in the thickness of grain boundary or primary alpha was attributed to cooling rate, which was different for each sample. Relatively slower cooling from β phase region during production causes formation of thick grain boundary α in addition to relatively coarse Widmanstätten structure composed of α and β phases. Apart from primary α phase, cooling rate also affected the fineness of the Widmanstätten structure, which is shown in Figures 4.10- 4.13. in which bright and dark regions correspond to β and α phases, respectively. Relatively finer Widmanstätten structure was obtained in sample produced at 90°; however, Widmanstätten structure was coarsest in sample produced at 0°. Accordingly, sample produced at 90° was cooled relatively faster and it received less heat input due to smaller cross-sectional area exposed e-beam during scanning.

77

Therefore, sample produced at 0° was cooled relatively slower and heat input was higher due to higher cross-sectional area interacted with the electron beam. On the other hand, martensitic phase, which is the common phase in SLM produced samples, was not observed in EBM samples due to slower cooling rate of EBM technique. During the production with EBM, Ti-6Al-4V alloy powders are preheated before each scan to approximately 650-700 °C, which is above the martensite start (Ms) temperature of the Ti-6Al-4V alloy. Although the scanned layers rapidly cool down from melting temperature, they don't cool below Ms temperature due to preheating which preclude transformation of β phase to martensitic α' phase. Therefore, EBM samples contained equilibrium α and β phases. Although, EBM yields more ductile samples with lower amount of residual stresses, the formation of grain boundary α, which is deleterious to mechanical properties, cannot be eliminated easily. Apart from the production direction, microstructure was observed to change slightly at different locations of the same sample, for example, primary α phase thickness in bottom to top sections of the sample produced at 0° samples was different (Figures 4.7, 4.9, 4.11 and 4.13). Both microstructure and primary α were relatively coarser at the top section of the specimen. The electron beam provides the heat source from top section of the produced specimen during scanning and both the base of the build plate (lower part of the sample) and deposited powder act as heat sink. Hence, bottom part of the sample cools relatively faster, thereby, resulting finer microstructure, while top portion of the specimen cools at a relatively slower rate.
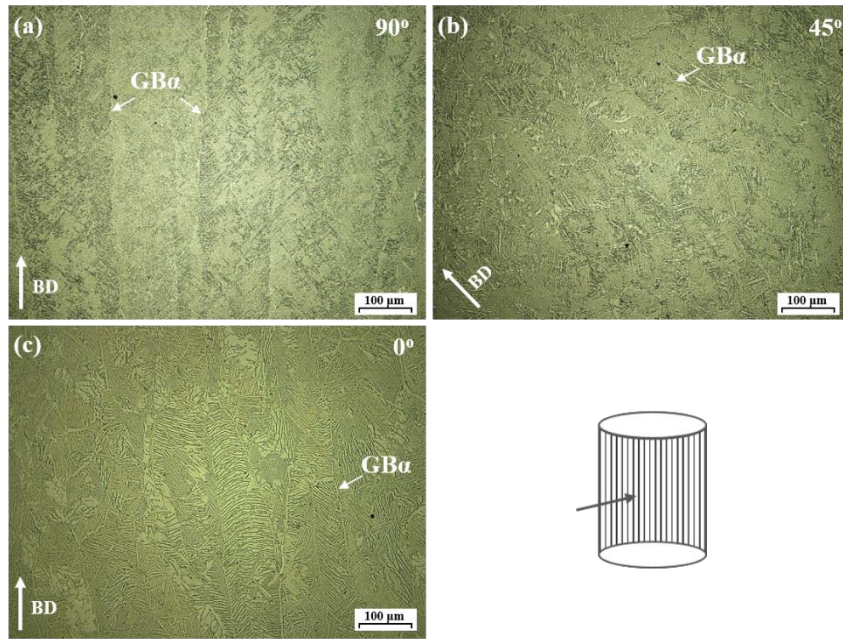
Figure 4.6. Optical micrographs of the as-produced Ti-6Al-4V alloy produced by EBM at different angles; (a) 90º, (b) 45º, (c) 0º (longitudinal direction).
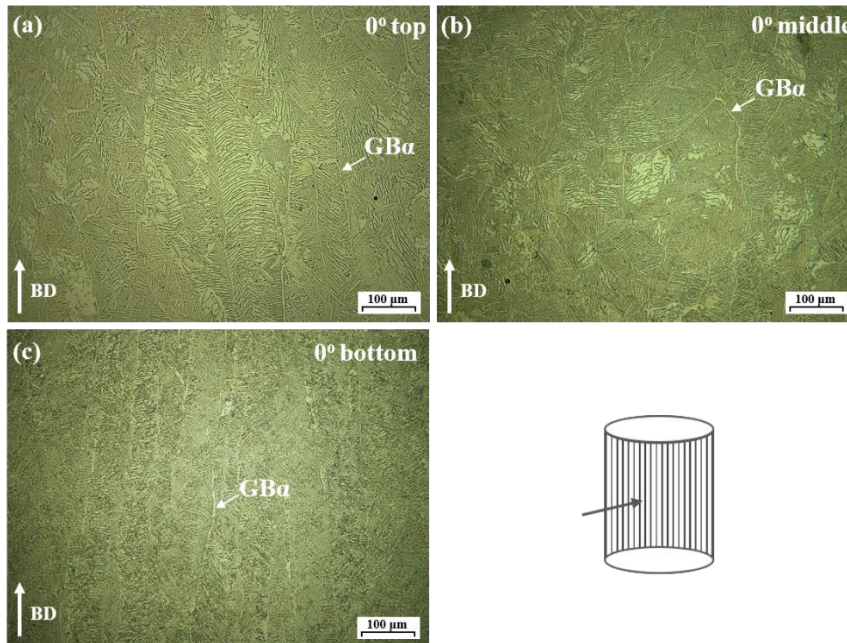
Figure 4.7. Optical micrographs of the as-produced Ti-6Al-4V alloy produced by EBM at different locations; (c) 0º top, (d) 0º middle and (e) 0º bottom (longitudinal direction).
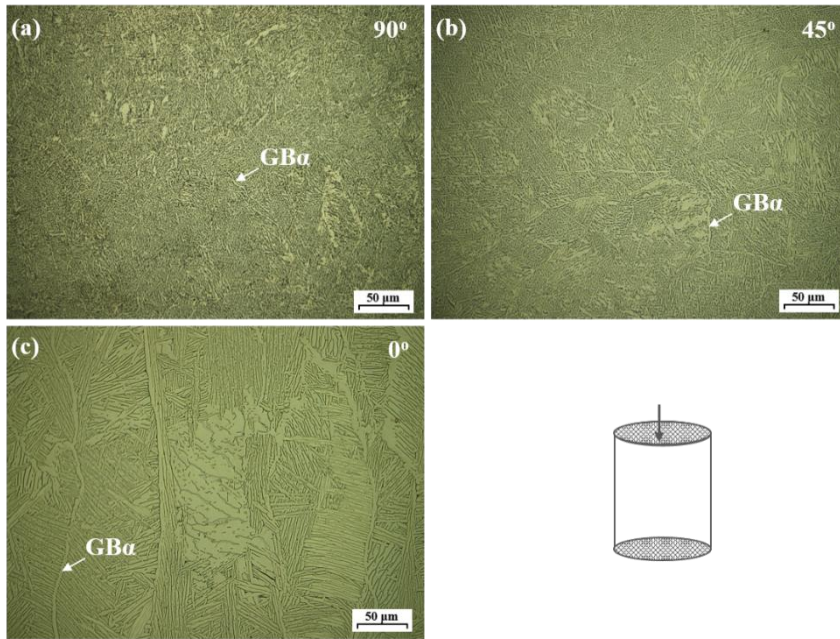
Figure 4.8. Optical micrographs of the as-produced Ti-6Al-4V alloy produced by EBM at different angles; (a) 90º, (b) 45º, (c) 0º (transverse direction).

Figure 4.9. Optical micrographs of the as-produced Ti-6Al-4V alloy produced by EBM at different locations; (c) 0º top, (d) 0º middle and (e) 0º bottom (transverse direction).

Figure 4.10. SEM images of the as-produced Ti-6Al-4V alloy produced by EBM at different angles; (a) 90º, (b) 45º, (c) 0º (longitudinal direction).
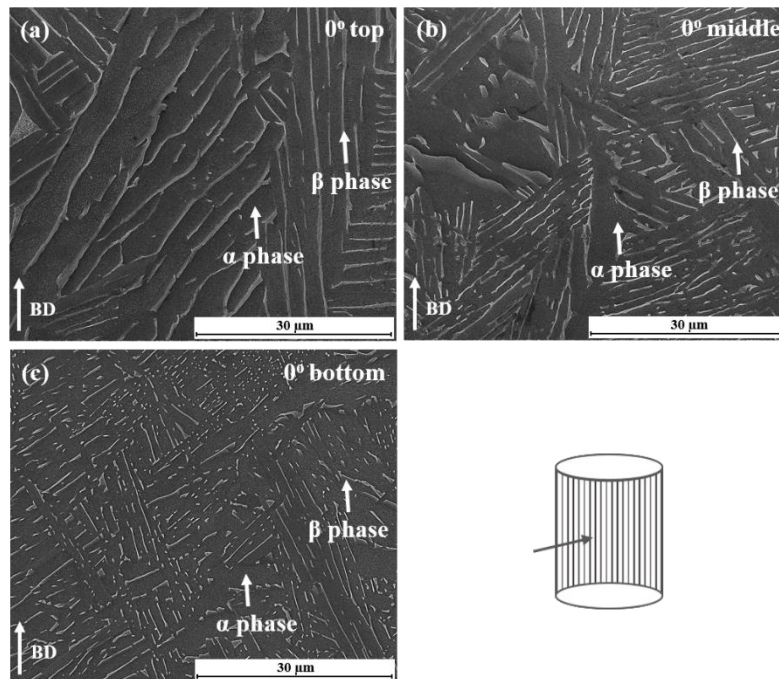
Figure 4.11. SEM images of the as-produced Ti-6Al-4V alloy produced by EBM at different locations; (a) 0º top, (b) 0º middle and (c) 0º bottom (longitudinal direction).

Figure 4.12. SEM images of the as-produced Ti-6Al-4V alloy produced by EBM at different angles; (a) 90°, (b) 45°, (c) 0° (transverse direction).
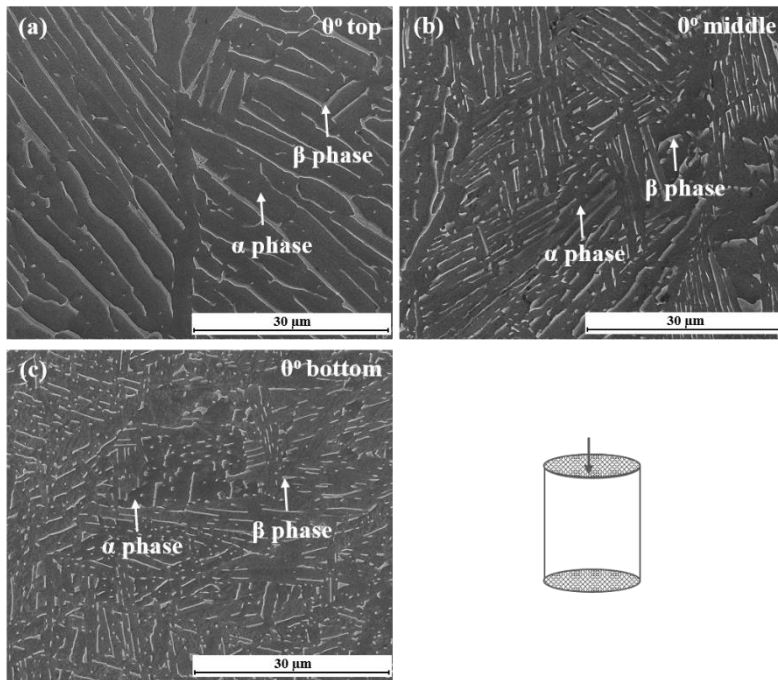
Figure 4.13. SEM images of the as-produced Ti-6Al-4V alloy produced by EBM at different locations; (a) 0° top, (b) 0° middle and (c) 0° bottom (transverse direction).

EBSD studies were done to clarify the microstructural development in longitudinal and transverse directions of the samples produced at 90º, 45º and 0º (Figures 4.14 and 4.15). The inverse pole figure (IPF) maps for the samples in longitudinal and transverse directions are demonstrated in Figures 4.14 (a)-(c) and 4.15 (a)-(c), and the image quality (IQ) maps are given in Figures 4.14 (d)-(f) and 4.15 (d)-(f). IPF and IQ maps revealed the Widmanstätten/basket weave structures clearly, and also columnar and equiaxed structures can be seen distinctly. The colors in IPF maps with respect to building direction display crystal orientations of the grains in the sample, and the normal planes of (0001) represented by red color, ($10\bar{1}0$) represented by blue color, and ($2\bar{1}\bar{1}0$) represented by green color planes are parallel to building direction. IPF maps of samples produced at 90º, 45º and 0º show that spatial distribution of grains was random, and there was no distinct preferred orientation for the grains due to the Widmanstätten/basket weave microstructure and three colors were shown randomly. On the other hand, β phase was not detected exactly using the phase maps shown in Figures 4.14 (g)-(i) and 4.15 (g)-(i) since determination of β phase in Widmanstätten/basket weave microstructure is difficult due to its relatively lower amount. The red color represents the α phase, green color represents the β phase and black lines represent the grain boundaries in the phase maps. When the phase maps were examined, nearly green color was not observed due to the reason mentioned above, and phase fractions of β phase shown in phase map indexes were too low, e.g., 0.008 for 90º, 0.006 for 45º and 0.007 for 0º.
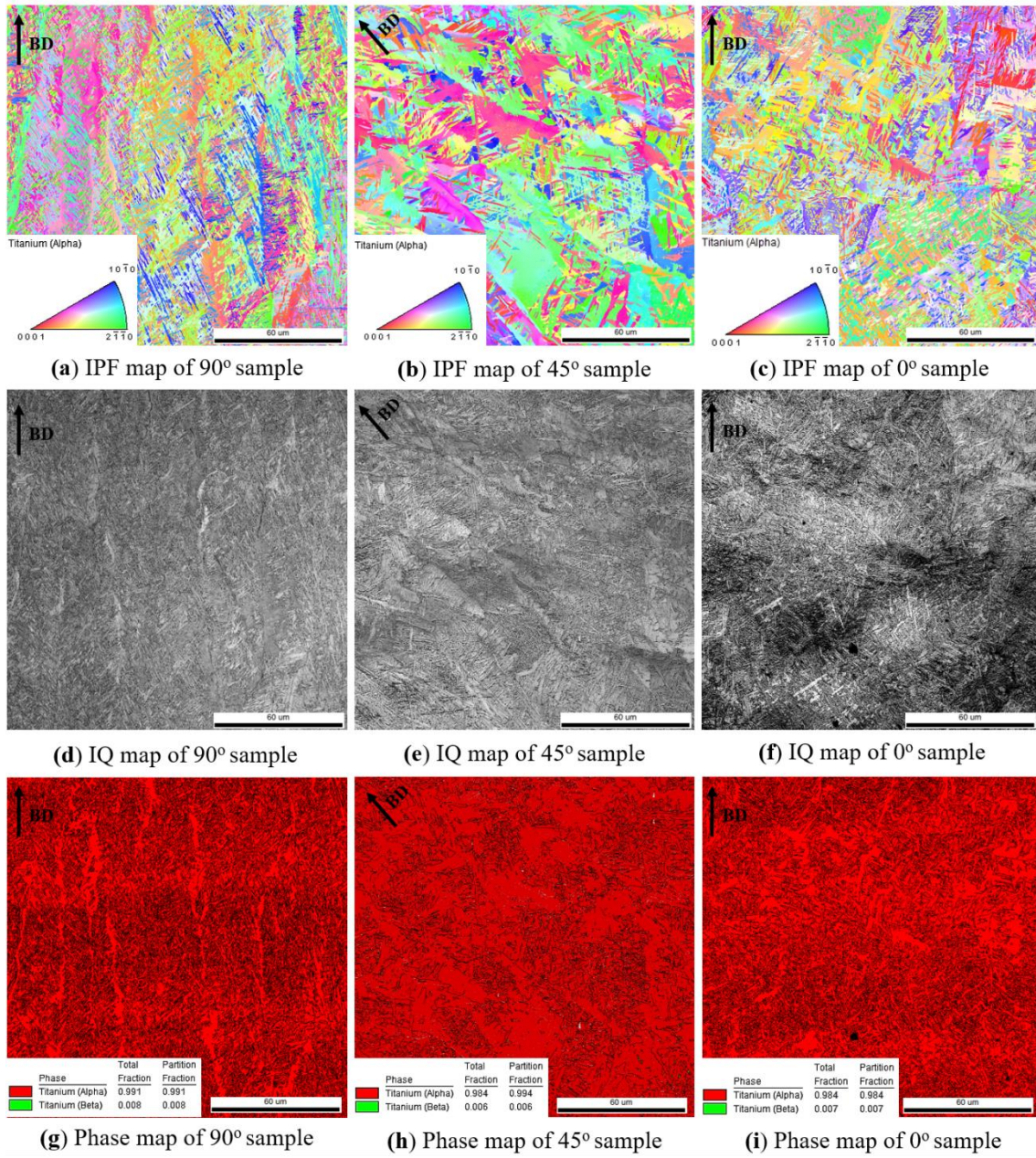
Figure 4.14. EBSD maps for the as-produced Ti-6Al-4V alloy produced by EBM at different angles;
(a-c) IPF maps with respect to building direction, (d-f) IQ maps, (g-i) phase maps (longitudinal
direction).

(a) IPF map of 90° sample   **(b)** IPF map of 45° sample   **(c)** IPF map of 0° sample

(d) IQ map of 90° sample   **(e)** IQ map of 45° sample   **(f)** IQ map of 0° sample

(g) Phase map of 90° sample   **(h)** Phase map of 45° sample   **(i)** Phase map of 0° sample
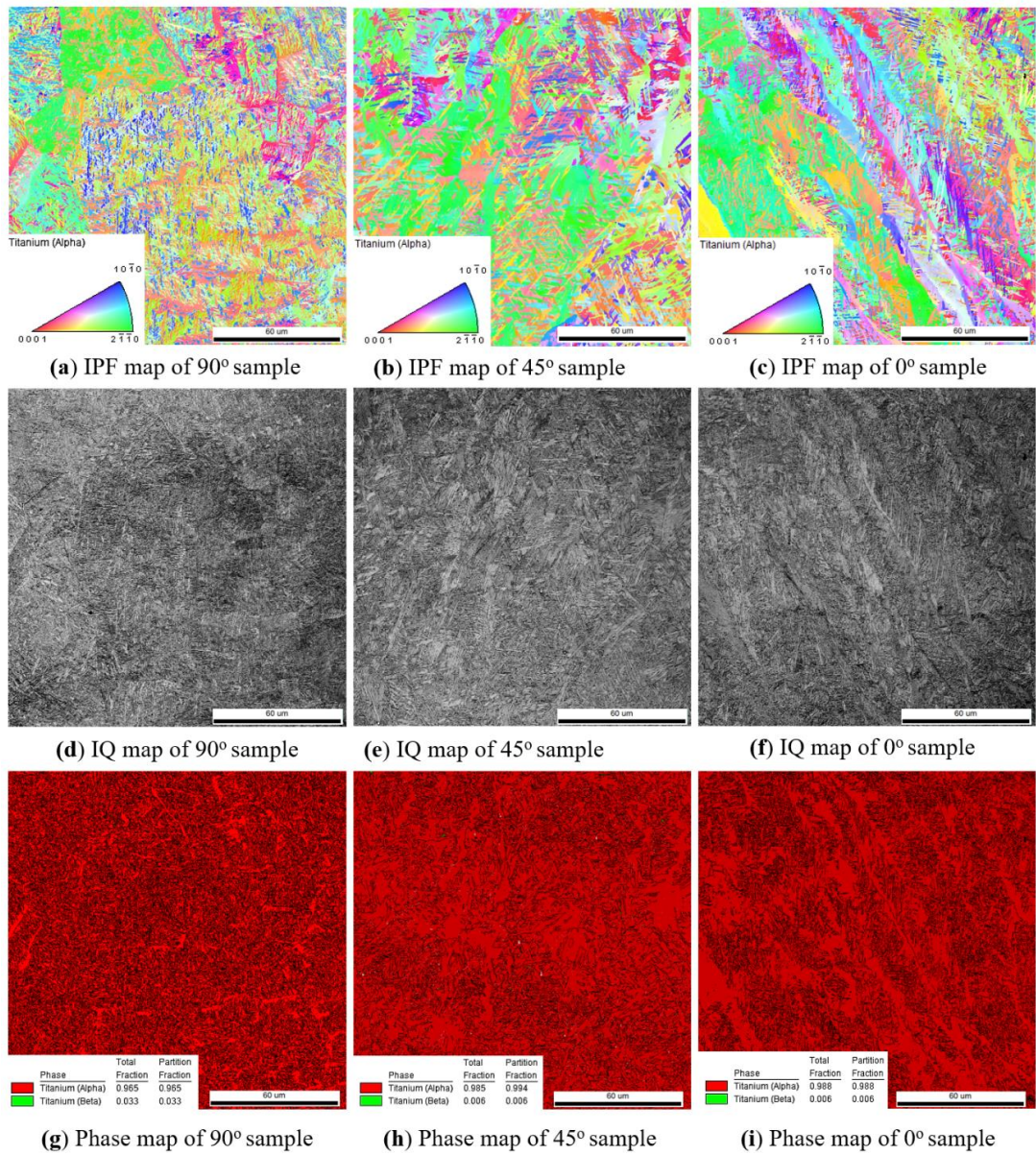
Figure 4.15. EBSD maps for the as-produced Ti-6Al-4V alloy produced by EBM at different angles; (a-c) IPF maps with respect to building direction, (d-f) IQ maps, (g-i) phase maps (transverse direction).

85

4.5.2. Hydrogenated Samples

In this section, the microstructures of the hydrogenated (at 650 °C for 1 h) Ti-6Al-4V alloy specimens produced by EBM at 90° were given. The as-produced microstructure, which consisted of α+β Widmanstätten/basket weave microstructure, changed with hydrogenation process. As it can be seen in Figures 4.16 and 4.17, needle-like structure was formed as a result of hydrogenation. According to XRD results (Figure 4.4 (c)), the new needle like phase was indexed as δ-phase. Moreover, the primary α phase on the grain boundary was disappeared partly, and instead of this, equiaxed α phase was formed between fine-needle like microstructure (gray colored round zones in Figures 4.17 (a) and (c)). The hydrogenated microstructure should be examined with High-Resolution Transmission Microscope (HR-TEM) to detect δ-phase formation exactly and correlate its presence with XRD results since optical microscope and SEM were not able to identify δ-phase formation clearly.
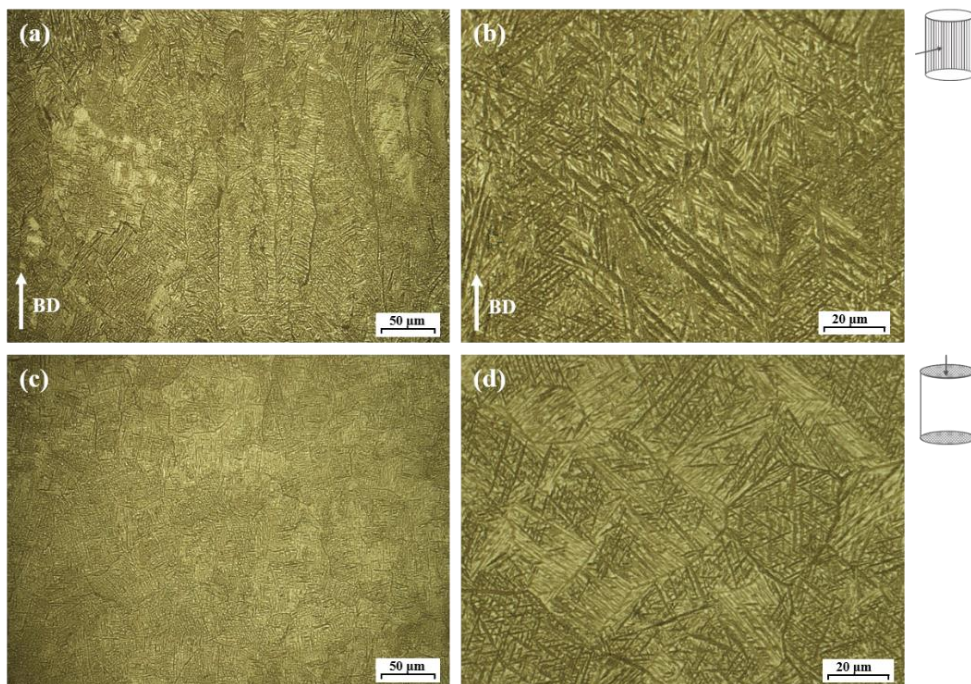
Figure 4.16. Optical micrographs of the hydrogenated at 650 °C for 1 h Ti-6Al-4V alloy produced by EBM in 90°, (a, b) longitudinal and (c, d) transverse directions.
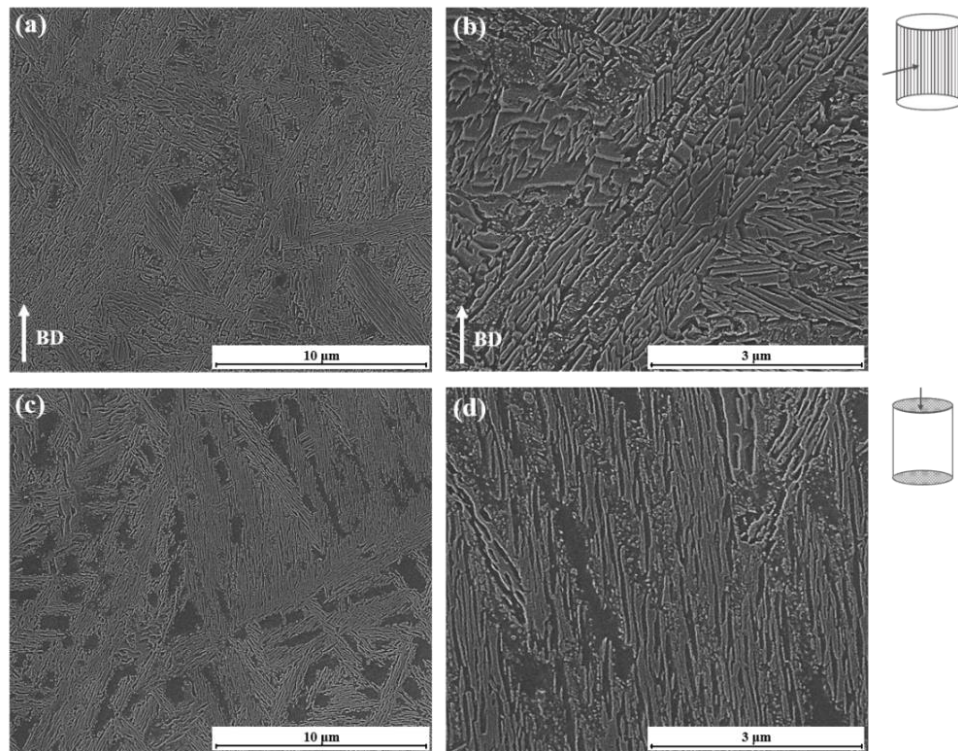
Figure 4.17. SEM images of the hydrogenated at 650 °C for 1 h Ti-6Al-4V alloy produced by EBM in 90° (a, b) longitudinal and (c, d) transverse directions.

4.5.3. Dehydrogenated Samples

In this part, the microstructures of dehydrogenated (700 °C for 18 h under 2×10^{-4} torr) samples, which were produced by EBM at 90°, are given. Dehydrogenation was applied to samples immediately after they had been hydrogenated at 650 °C for 1 h. Additionally, EBSD studies were done on dehydrogenated samples as well to see the effect THP process (hydrogenation-dehydrogenation). The aim of the dehydrogenation step in the THP was refining the microstructure by allowing δ-hydride phase to fine equilibrium α phase transformation via withdrawal of the hydrogen in the sample. The optical micrographs and SEM images of the dehydrogenated samples for longitudinal and transverse directions are given in Figures 4.18 and 4.19, respectively. After dehydrogenation step, the hydrogen content, which was 1.97 wt. % in hydrogenated sample, was reduced to 0.0008 wt. %, below

87

the maximum value (0.015 wt. %) defined by ASTM F2924-14 standard (Table 4.4). When the microstructures of the dehydrogenated samples were examined, it was seen that needle-like microstructure (belonging to δ-phase) formed after hydrogenation step (Figure 4.16) disappeared and relatively finer microstructure, comprised of α and β phase mixture, was formed as confirmed by XRD results (Figure 4.4). The δ-hydride phase lost its hydrogen during dehydrogenation step and transformed to fine α phase. In addition, hydrogen levels of α and β-phases in hydrogenated samples decreased as well. It was observed also that the α phase reformed along the grain boundaries as well as within the grains as a result of δ-hydride phase to α phase transformation.
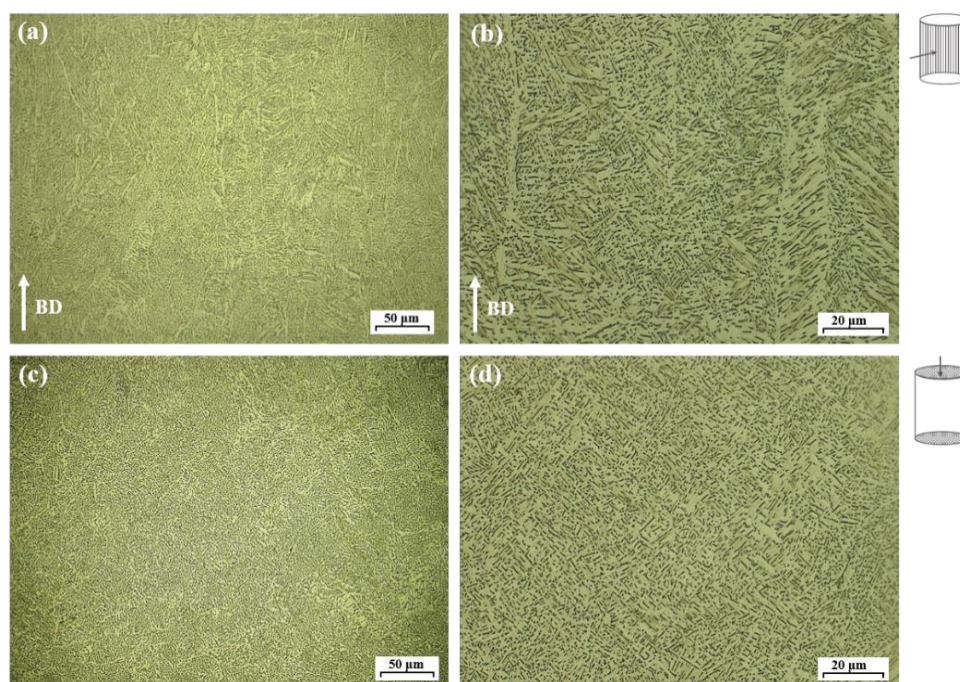
Figure 4.18. Optical micrographs of the dehydrogenated at 700 °C for 18 h Ti-6Al-4V alloy produced by EBM in 90° (a, b) longitudinal and (c, d) transverse directions.
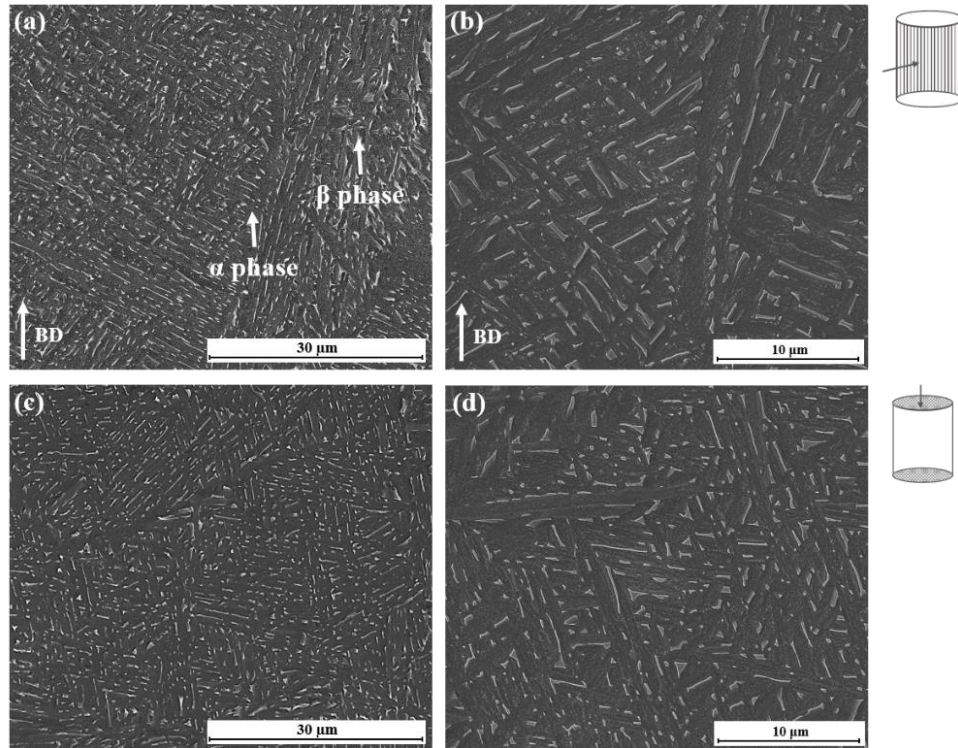
Figure 4.19. SEM images of the dehydrogenated at 700 °C for 18 h Ti-6Al-4V alloy produced by EBM in 90° (a, b) longitudinal and (c, d) transverse directions.

It was concluded that dehydrogenation cannot eliminate the grain boundary α present in the as-produced samples (Figure 4.6) since δ-hydride phase retransforms to α-phase again. Phase transformations and microstructural refinement during dehydrogenation can be seen clearly in SEM images given in Figure 4.19. Relatively coarse microstructure in hydrogenated sample (Figure 4.17) composed of δ-hydride transformed to lamellar structure containing α and β phases. Although it is difficult to distinguish from SEM images, microstructural refinement with respect to as-produced sample (Figures 4.10 and 4.12) was also evident. Continuous lamellas of β-phase in as-produced sample have been turned into short and discontinuous β-lamellas probably due to previously formed δ-hydride phases along the α and β phases interface region.

EBSD studies were carried out in longitudinal and transverse directions of the dehydrogenated samples produced at 90º are shown in Figure 4.20. The inverse pole figure (IPF) maps for the dehydrogenated samples are demonstrated in Figure 4.20 (a) (for longitudinal direction) and Figure 4.20 (b) (for transverse direction), and the image quality (IQ) maps are shown in Figure 4.20 (c) (for longitudinal direction) and Figure 4.20 (d) (for transverse direction). The columnar and equiaxed structures of previous β-grains along longitudinal and transverse directions, respectively, can be seen clearly in the IPF and IQ maps. The phase maps for α and β phases are shown in Figure 4.20 (e) (longitudinal direction) and Figure 4.20 (f) (transverse direction). Since the refined β phase in the dehydrogenated sample was so fine, it couldn't be detected exactly, and green color was not observed in phase maps. In addition, phase fractions of β phase shown in phase map indexes (Figure 4.20 (g)-(h)) are too low, e.g., 0.005 for 90º angle (longitudinal direction), which was 0.008 for as-produced sample at 90º.
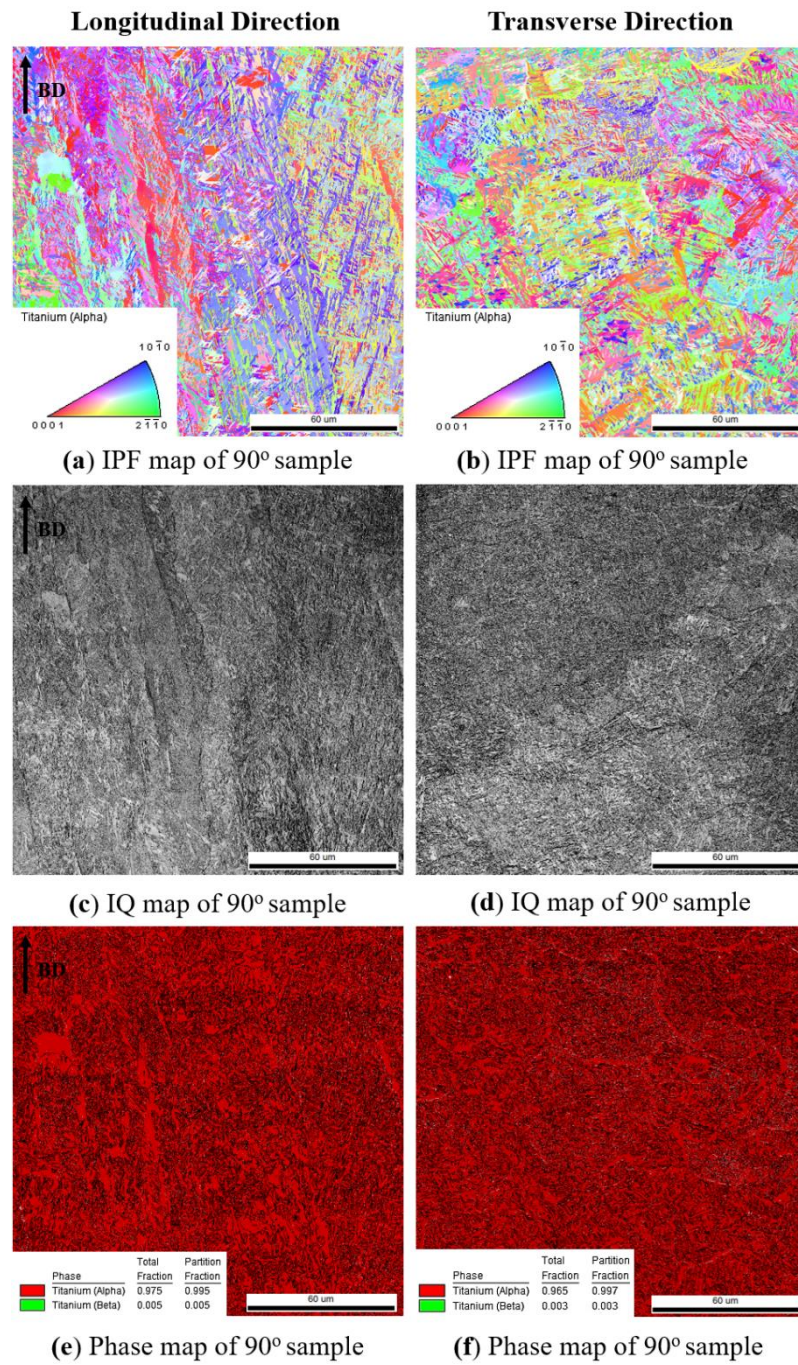
Figure 4.20. EBSD maps for the dehydrogenated Ti-6Al-4V alloy produced by EBM in 90°
(longitudinal and transverse directions): (a, b) IPF maps with respect to building direction, (c, d) IQ
maps, (e, f) phase maps.

91

4.5.4. Annealed Samples

The conventional annealing is a classical post heat treatment process applied to additively manufactured parts to change the microstructure and to get rid of residual stress formed due to rapid cooling of the parts during production. In this study, classical annealing treatment was applied to compare the effect of thermo-hydrogen treatment and annealing on final microstructure and mechanical properties of Ti-6Al-4V alloys. Samples produced at 90° were annealed at 840 °C for 2 h, and then they were cooled in the furnace under argon gas atmosphere. As it was expected, Widmanstätten/basket weave structure was preserved as a result of annealing; however, prior β grains were coarsened and phase thicknesses of α and β-phases became higher (Figures 4.21 and 4.22). Additionally, primary α phase on the grain boundaries became thicker with annealing process due to enhanced diffusion at high annealing temperatures.
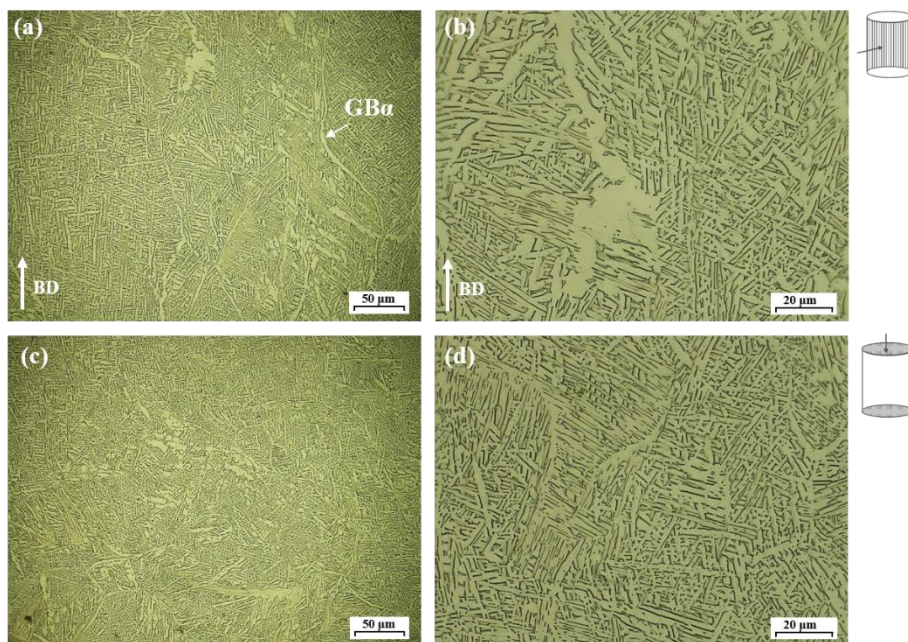
Figure 4.21. Optical micrographs of the annealed at 840 °C for 2 h Ti-6Al-4V alloy produced by EBM in 90° (a, b) longitudinal and (c, d) transverse directions.
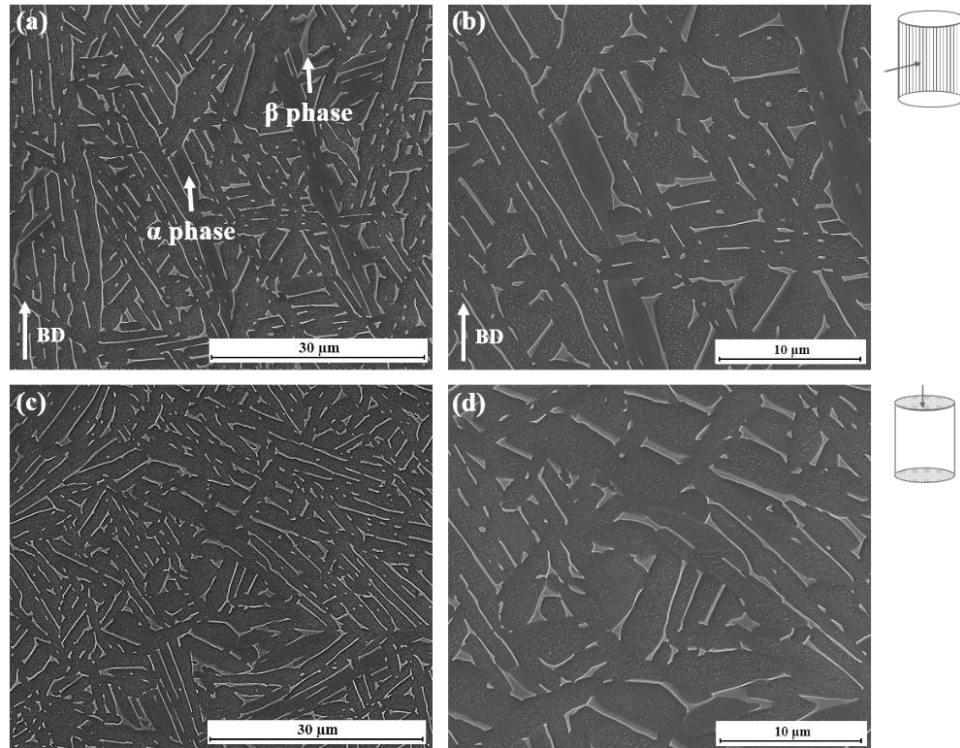
Figure 4.22. SEM images of the annealed at 840 ᵒC for 2 h Ti-6Al-4V alloy produced by EBM in 90ᵒ
(a, b) longitudinal and (c, d) transverse directions.

EBSD results for longitudinal and transverse directions of the annealed samples are shown in Figure 4.23. The inverse pole figure (IPF) maps are demonstrated in Figure 4.23 (a) (longitudinal direction) and Figure 4.23 (b) (transverse direction), and the image quality (IQ) maps are given in Figure 4.23 (c) (longitudinal direction) and Figure 4.23 (d) (transverse direction). The coarser columnar and equiaxed structures can be seen clearly in the IPF and IQ maps. The phase maps are shown in 4.23 (e) (longitudinal direction) and Figure 4.23 (f) (transverse direction). When the phase maps were examined, the phase fractions of β phase was seen as 0.016 for the sample produced at 90ᵒ (longitudinal direction), which was 0.008 for as-produced and 0.005 for THPed samples produced at the same angle. The increment in phase fraction was attributed to the microstructural coarsening.
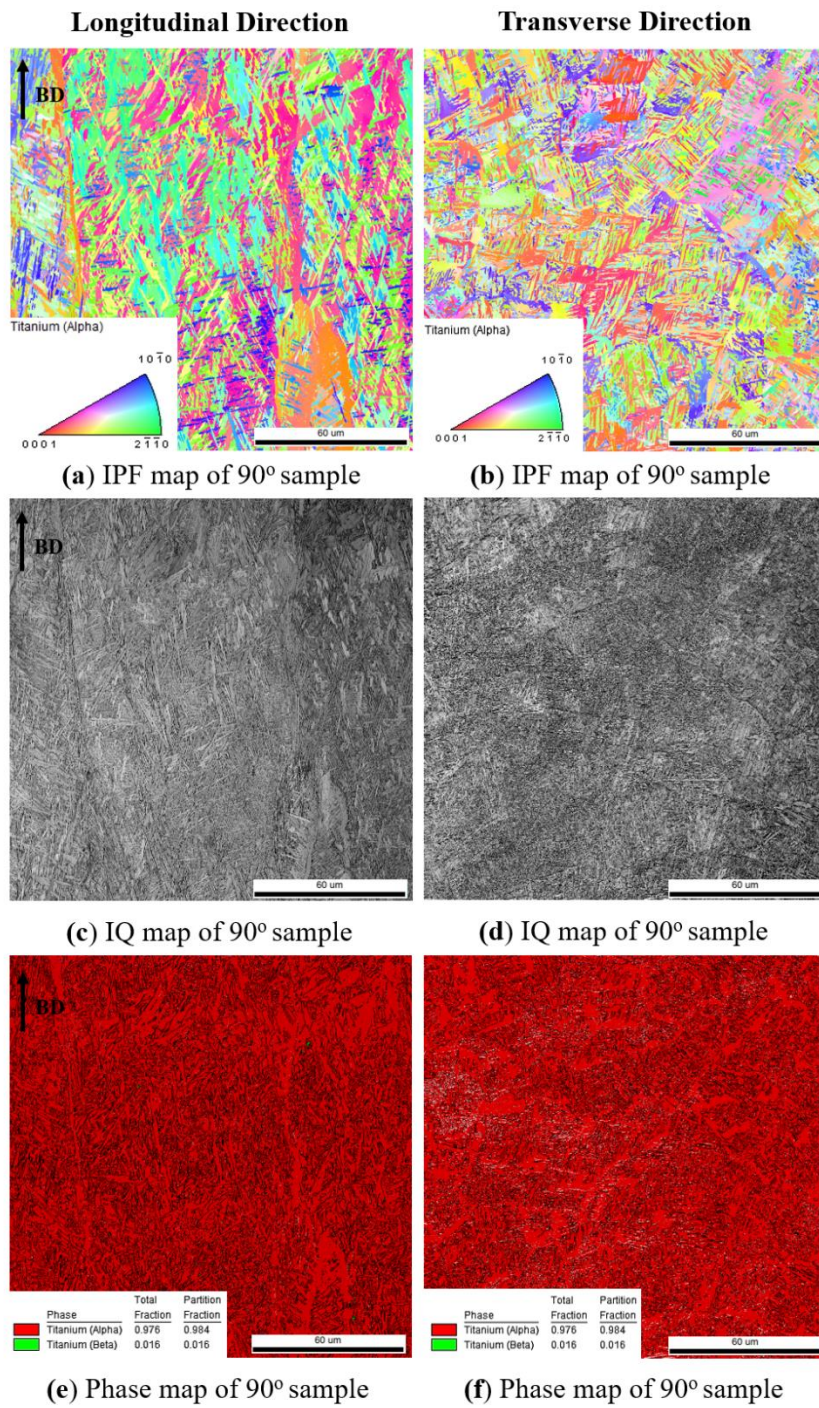
Figure 4.23. EBSD maps for the annealed Ti-6Al-4V alloy produced by EBM in 90º (longitudinal and transverse directions): (a, b) IPF maps with respect to building direction, (c, d) IQ maps, (e, f) phase maps.

4.5.5. The Texture Studies of As-produced and Post-Processed Ti-6Al-4V Alloys

In this section, the effect of building angle (0°, 45° and 90°) on texture formation of Ti-6Al-4V alloys was investigated by using EBSD technique. Additionally, by keeping the building direction constant at 90°, texture formation after various post processing, e.g. thermo-hydrogen treatment and annealing, was also examined.

4.5.5.1. The Effect of Building Angle

As it is known, the building direction in additive manufacturing affects the local texture formation thereby, causing anisotropic mechanical properties. The columnar prior β-grain structure which was parallel to building direction of the as-produced Ti-6Al-4V alloy was detected as seen in the similar studies [129–132] conducted on grain structure of EBM produced Ti-6Al-4V alloy. However, despite the several works conducted on the grain structure of the EBM produced Ti-6Al-4V alloys, the texture studies are quite limited.

In this part, the textures of the as-produced specimens fabricated by EBM at different angles (90°, 45° and 0°) were investigated using EBSD method. During the phase transformation from β phase to α phase, according to Burger's relationship $\{0001\}_\alpha$ // $\{110\}_\beta$ and $\langle 11\overline{2}0 \rangle_\alpha$ // $\langle 111 \rangle_\beta$, the α phase has 12 variants to precipitate within the columnar β grains so that the texture of the α phase is generally weak because one β grain can generate 12 different α grain because α phase has 12 different crystallographic orientations. In our study, textures were gathered parallel to building directions of the samples produced at different angles (90°, 45° and 0°).

The α-texture of the as-produced specimens fabricated by EBM at different angles (90°, 45°, and 0°) taken from the longitudinal direction are shown in IPFs maps (Figure 4.24) and pole figures (PFs) maps (Figure 4.25 (a, c, e)).

According to IPF, the texture of the α phase in the sample produced at 90° concentrated with the maximum intensity value of 3.217 in $(10\overline{1}0)$ (Figure 4.24 (a)), which is parallel to building direction, and also the other dominant texture component can be

described as "Basal planes (0001) rotated 30 degrees around the building direction". The texture of β phase in the sample produced at 90° concentrated with the maximum intensity value of 15.968 in (001)$_\beta$, which was parallel to building direction (Figure 4.25 (b)). This type of texture is the most favorable solidification orientation for cubic metals. Moreover, when the PFs of α and β phases in the as-produced 90° sample were examined, (0001)$_\alpha$ // (011)$_\beta$ relation was observed, which obeys Burger's relationship. Likewise, Al-Bermani et al. [130] studied the texture of the EBM produced Ti-6Al-4V alloy produced at 90° angle, and they reconstructed prior β phase by using Burger's relationship for the α-phase orientations. (001)$_\beta$ // building direction, which is typical solidification orientation for cubic metals, was also detected in their study for β phase, and also (0001)$_\alpha$ // (011)$_\beta$ relation can be deduced from their study.

Likewise, when the IPF of α texture in sample produced at 45° was examined, it was seen that the texture concentrated with the maximum intensity value of 3.196 in (10$\bar{1}$0) (Figure 4.24 (b)) which was parallel to again building direction. Also, basal planes (0001) rotated 30 degrees around the building direction texture was observed. The texture of β phase in the sample produced at 45° concentrated with the maximum intensity value of 13.222 in (001)$_\beta$ which was parallel to building direction (Figure 4.25 (d)). Moreover, when the PFs of α and β phases were examined, (0001)$_\alpha$ // (011)$_\beta$ relation was seen, which obeys Burger's relationship. Moreover, in this sample, additional texture was also observed between (0001) and (2$\bar{1}\bar{1}$0) planes.

Finally, according to IPF, the texture of the α phase in the sample produced at 0° concentrated with the maximum intensity value of 4.359 in (10$\bar{1}$0) (Figure 4.24 (c)) which was again parallel to building direction. Moreover, the texture of basal planes (0001) rotated 30 degrees around the building direction, and additional texture was also observed between (0001) and (2$\bar{1}\bar{1}$0) planes were observed. The texture of β phase in the sample produced at 0° concentrated with the maximum intensity value of 17.190 in (001)$_\beta$ which was parallel to building direction (Figure 4.25 (f)). Moreover, when the PFs of α and β phases were examined, (0001)$_\alpha$ // (011)$_\beta$ relation, which obeys Burger's relationship.

As a conclusion, regardless of the building angle, the prior β phase texture was composed of (001) // built or heat flow direction, and high temperature β phase transforms to α phase by fulfilling the burgers relationship.
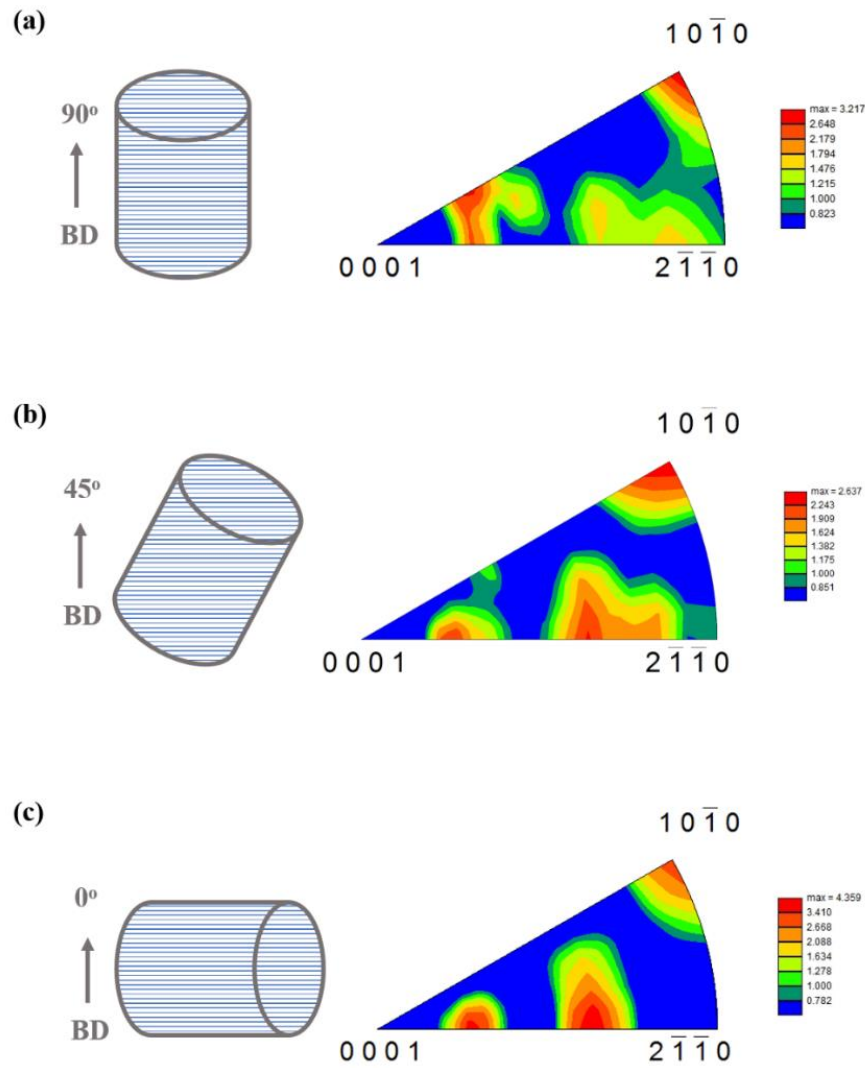
Figure 4.24. Inverse pole figures of the α-phase with respect to building direction for as-produced samples fabricated at different angles: (a) 90º, (b) 45º and (c) 0º taken from the longitudinal direction.
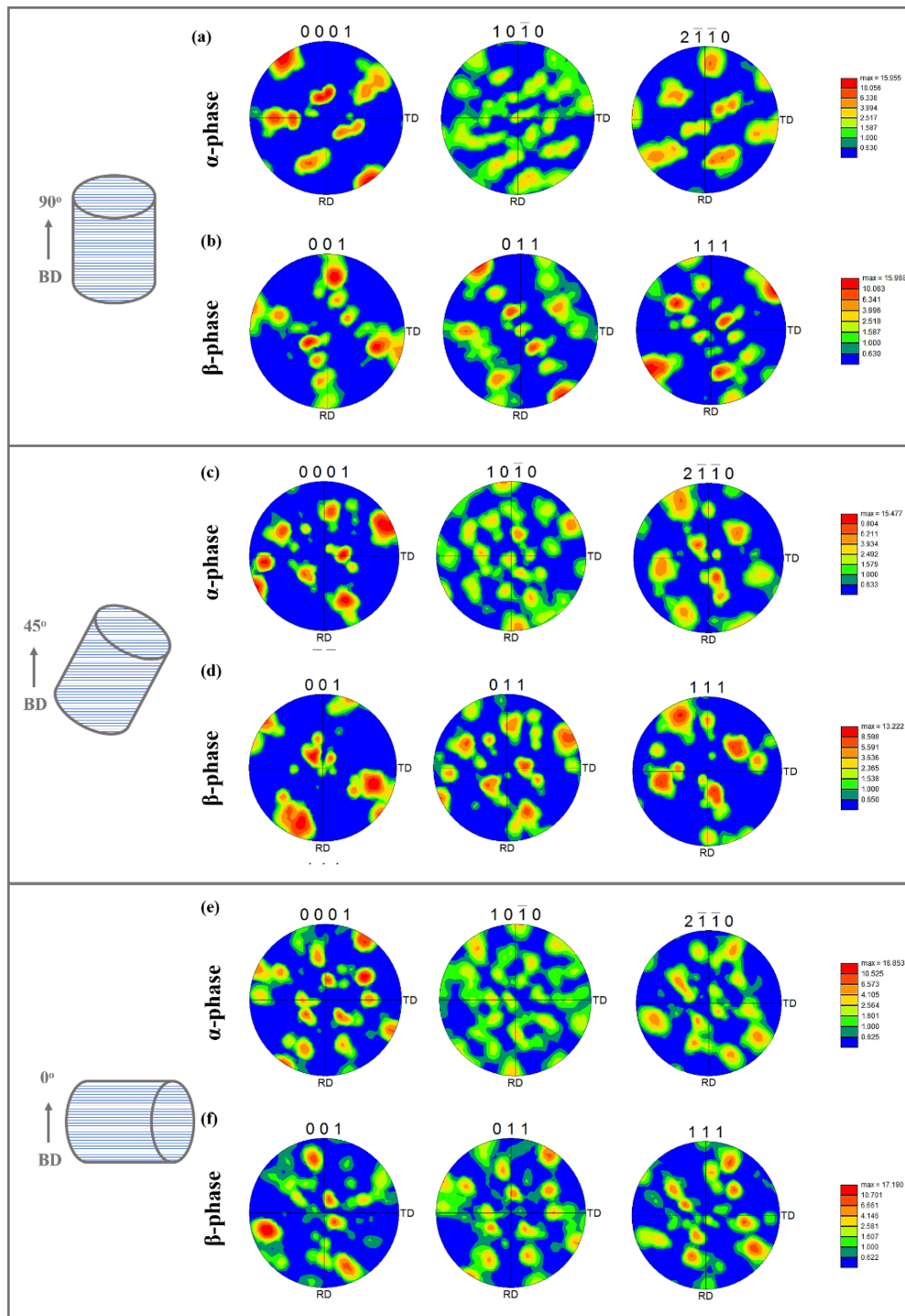
Figure 4.25. Pole figures of the α-phase (a, c, e) and β-phase (b, d, f) of the as-produced specimens fabricated by EBM in different angles (a) 90º, (b) 45º and (c) 0º taken from the longitudinal direction.

4.5.5.2. The Effect of Post Processing

In this part, the effect of heat-treatments (THP and conventional annealing) on the α and β phase textures in Ti-6Al-4V alloys produced at 90° was investigated. IPFs and PFs of the as-produced and heat treated specimens taken from the longitudinal directions are shown in Figures 4.26 and 4.27.

When IPF of the THP treated samples were examined, it was seen that the texture concentrated with the maximum intensity value of 5.084 in (0001), which meant (0001) was parallel to building direction (Figure 4.26 (b)). On the other hand, the texture of β phase in the same sample concentrated with the maximum intensity value of 13.919 in $(001)_\beta$ which was parallel to building direction (Figure 4.27 (d)). There was a random texture for thermo-hydrogen processed (THPed) sample, and it was thought that the phase transformation from α phase (hcp) to δ phase (fcc) during the hydrogenation step could be caused random distribution. Also, $(0001)_\alpha$ // $(011)_\beta$ relation was determined. It can be said that THP process affected both underlying microstructure and the texture of the EBM produced specimens.

The α phase texture in annealed specimen was detected close to basal planes (0001) rotated 30 degrees around building direction with the maximum intensity value of 5.972 as shown in Figure 4.26 (c). Additionally, the texture of β phase in the sample produced at 90° concentrated with the maximum intensity value of 34.940 in $(001)_\beta$ which is parallel to building direction (Figure 4.27 (f)).

In the literature [133], the texture such as (0001) // [building direction] is seen for the deformed hexagonal structured metals having lower c/a ratio than ideal. When the deformed materials are annealed, recovery, recrystallization and grain growth processes occur. If subgrain coarsening occurs for the recovery process, change in texture can be observed. For recrystallization step, large changes in texture can be observed or no texture change occurs (e.g. large second phase particle are present in large volume fractions).

Various parameters such as alloy composition, initial gain size, presence of precipitates, deformation mode, deformation temperature and strain affect the texture change in recrystallization step. Also, heating rate and temperature of annealing can affect the texture but they are less significant. Finally, important texture changes may occur in the grain growth step, and it can be due to abnormal grain growth. Additionally, normal grain growth can or cannot cause to change in texture [134]. Lu et al. [132] investigated the texture in EBM produced Ti-6Al-4V alloy before and after HIP (920 °C for 2 h under 100 MPa in argon). They concluded that during the heating stage of HIP, β phase coarsened and its volume fraction increased. Additionally, α phase can grow preferentially at the expense of other α variants during cooling from high temperature to room temperature, thereby, intensifying and changing the texture of specimen. In our study, annealing caused intensifying of α and β textures; however, THP changed the texture of the as-produced Ti-6Al-4V alloy.
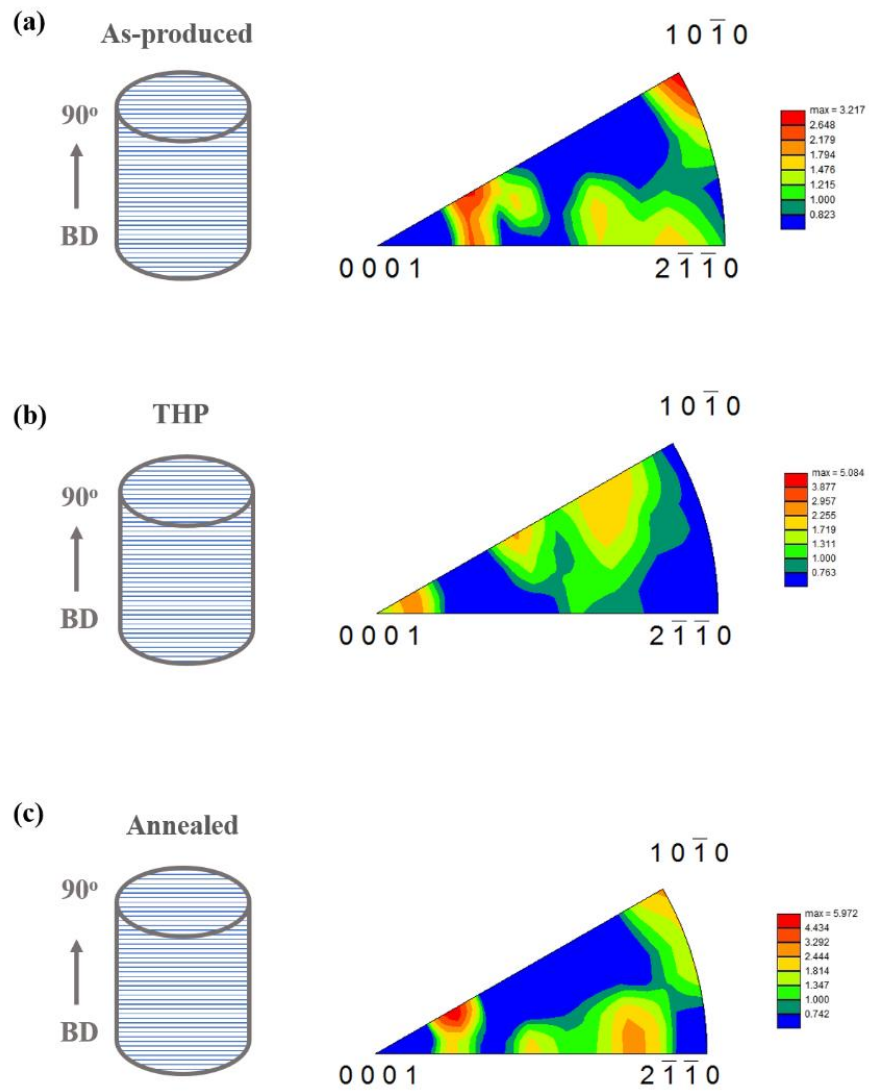
Figure 4.26. Inverse pole figures of the α-phase with respect to building direction for (a) as-produced, (b) THPed and (c) annealed specimens produced by EBM at 90° taken from the longitudinal direction.
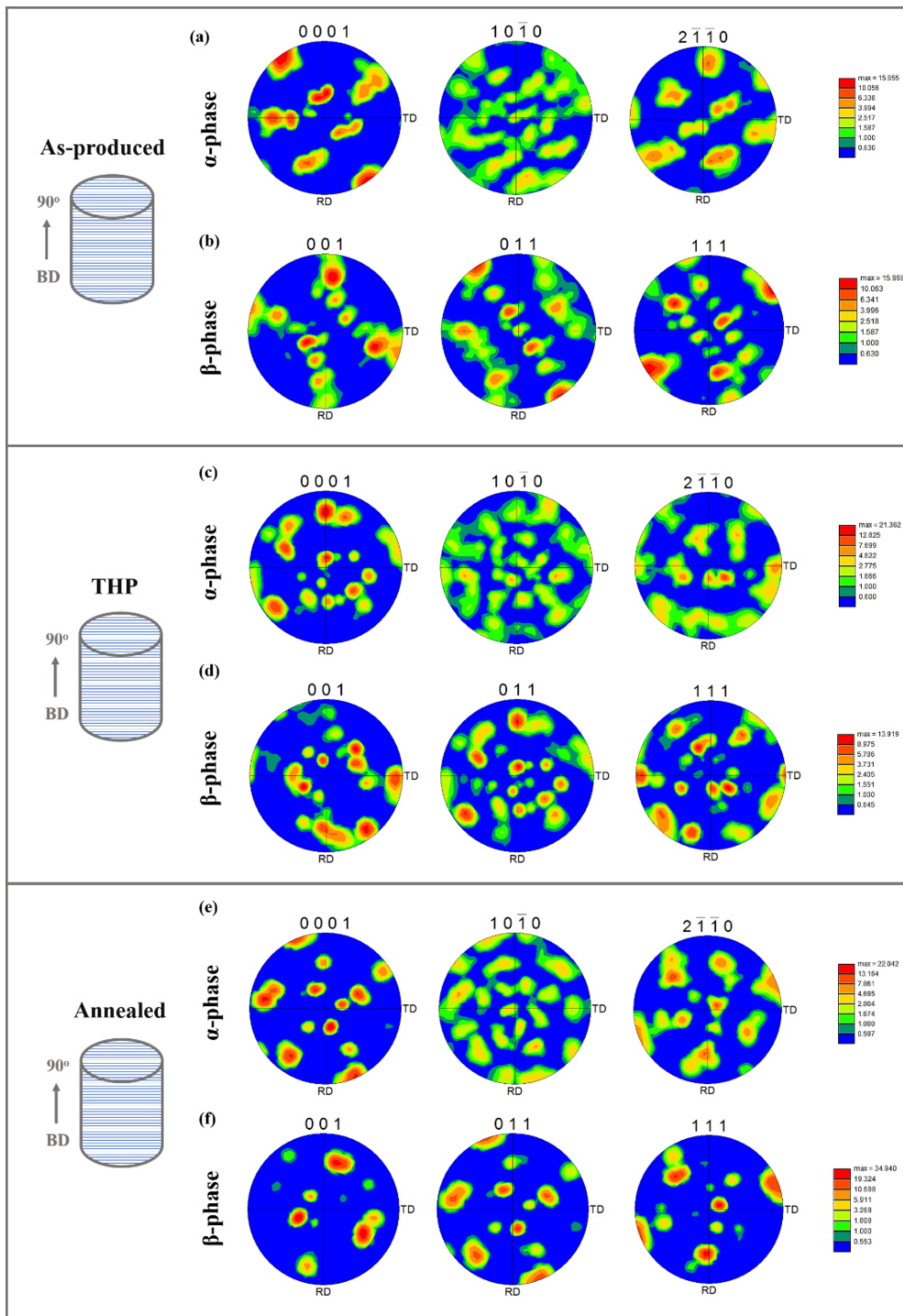
Figure 4.27. Pole figures of the α-phase (a, c, e) and β-phase (b, d, f) of the as-produced, THPed and annealed specimens fabricated by EBM at 90º taken from the longitudinal direction.

4.6. Mechanical Properties

4.6.1. Microhardness Measurements

In this part, firstly, the Vickers microhardness test results are given for the specimens produced at different angles and then, the effect of heat treatments (THP and annealing) on the microhardness is presented.

4.6.1.1. Specimens Produced at Different Angles

The hardness values of Ti-6Al-4V alloys produced at 90°, 45° and 0°, and additionally, hardness changes at three different locations (bottom, middle and top) within the same sample produced at 0° are shown in Figure 4.28. When the effect of production angle on the hardness values were examined, the highest hardness value (342.4 ± 2.8 HV) was found for the 90° specimen.
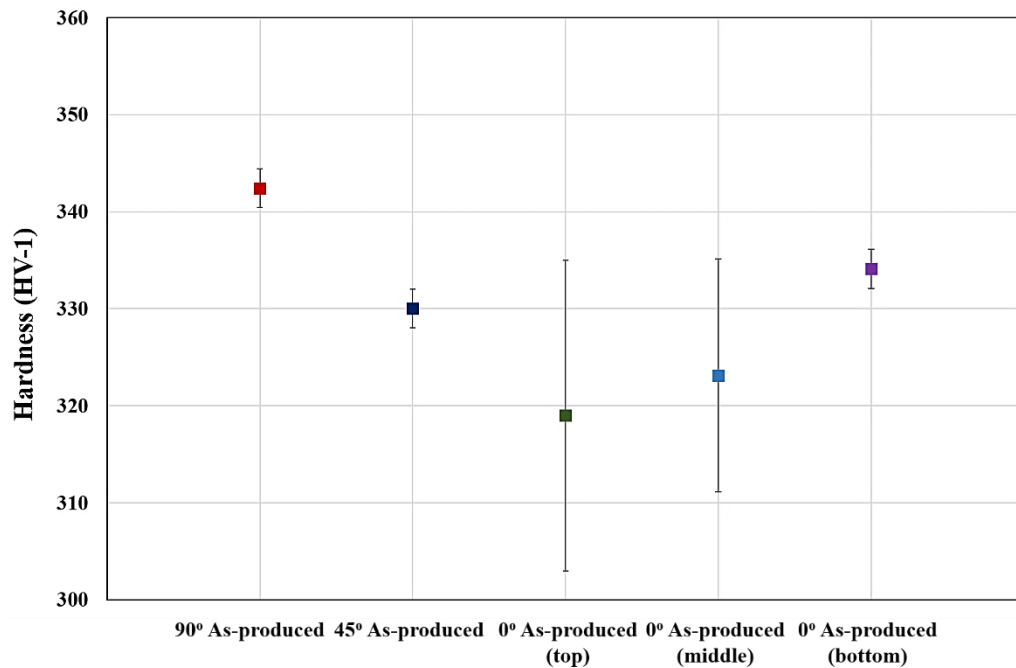
Figure 4.28. Hardness values of specimens produced by EBM in different angles; 90°, 45°, 0^o_{top}, 0^o_{middle} and 0^o_{bottom}.

On the other hand, hardness values of $0°$ and $45°$ specimens were relatively similar and smaller than $90°$ sample. As presented in Figures 4.6, 4.8, 4.10 and 4.12, the finest microstructure was observed in specimens produced at $90°$, while the other samples had relatively coarser microstructure with thicker α and β phases and larger amount of primary α along the prior β grain boundaries. Therefore, the highest hardness value was observed in specimen produced at $90°$ due to finer microstructure formed during relatively faster cooling of the sample. On the other hand, scanned cross-sectional area by e-beam was larger for other samples ($0°$ and $45°$) so that they exposed to high temperatures for longer durations, thereby, causing coarser microstructures. Apart from the production direction, the hardness values at different locations of the same sample were also different. For the sample produced at $0°$, the average hardness value was the lowest at the top portion of the specimen compared to other sections. The maximum hardness value was detected at the bottom section of the same sample, which was scanned and formed firstly during additive manufacturing. This section was exposed to high temperature for short duration, while the top section, which was the last scanned portion, stayed at high temperatures for longer durations and cooled at relatively slower cooling rate. Therefore, the microstructure at the top section was relatively coarser with respect to bottom sections (Figures 4.7 (a, c) and 4.9 (a, c)) which caused difference in average hardness values.

4.6.1.2. Post Processed Specimens

The effect of hydrogenation, combined hydrogenation and dehydrogenation treatment (THP), and post annealing treatment on hardness values of the specimens produced at $90°$ are given in Figure 4.28. About 15-20% hardness increase was observed as a result of hydrogenation treatment since hard δ phase was formed in the sample (Figures 4.4, 4.16 and 4.17). However, the hardness value of the specimen was decreased as a result of dehydrogenation applied just after hydrogenation step due to disappearance of δ phase (Figure 4.4). Although hardness decreased after dehydrogenation step, it was higher than that of starting as-produced sample. The hardness difference was very small since THP had limited refinement effect on microstructure.

On the other hand, the lowest hardness was observed in the annealed specimen since relatively coarser microstructure (Figures 4.21 and 4.22) was formed due to higher heat treatment temperatures and slower cooling rates.
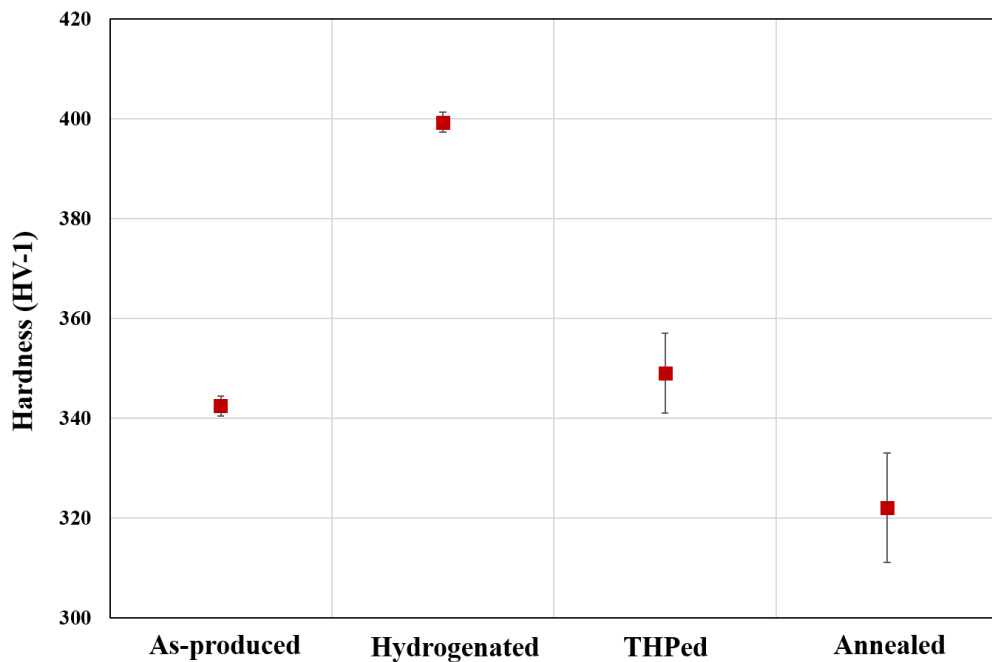
Figure 4.29. Hardness values of specimens produced at 90° by EBM; as-produced, hydrogenated, THPed and annealed samples.

4.6.2. Tensile Tests

The tensile tests were applied to dog-bone shaped specimens shown in Figure 3.7, and the results of the tensile tests were presented for both as-produced and chemically polished specimens produced at different angles and post-processed using different techniques. Surface condition of additively manufactured parts are crucial since it directly affects the mechanical properties because of notch effect due to presence of partially melted powders on the surface. Therefore, the parts' surfaces may need to be polished either mechanically or chemically.

4.6.2.1. Specimens Without Chemical Polishing

The stress-strain curves of as-produced samples at different angles are shown in Figure 4.30. As can be seen, all of the alloys produced at different angles exhibited a liner elastic region, strain hardening region, which was followed by necking and subsequent fracture. The ultimate tensile strength (UTS) and strain at fracture (%) values of the as-produced specimens produced at different angles and ASTM standard values are shown in Table 4.5. In the literature, the minimum and maximum UTS and ductility values for with or without surface treated Ti-6Al-4V alloys produced at different angles were presented as 811-1116 MPa and 2.1-17 % [31], respectively (Table 2.6). In this study, when the average tensile test results were examined, the specimen produced at 0° had the highest average UTS value (925.5 MPa), which meets ASTM F2924-14. The elongated columnar grains of prior β phase (parallel to building direction) in this sample was perpendicular to tensile axis (Figures 4.6 and 4.7) and they contained primary α phase along the grain boundaries. Therefore, lower ductility and tensile strength was expected since primary α perpendicular to tensile axis is expected to accelerate damage under tensile opening mode [135]. The observed higher tensile strength and comparatively high elongation in this specimen despite the improper alignment of grains and primary phases was attributed to its thermal history, which included exposure to high temperatures for longer durations due to its larger cross-sectional area in contact with e-beam. Because of that, parts with lower amount of porosities were attained (Table 4.1) due to better fusion of powder particles; however, relatively coarser microstructure was obtained (Figure 4.6). Accordingly, thermal history in this sample became dominant in determining the mechanical properties. On the other hand, lower average tensile strength (878.0 MPa) was measured in specimen produced at 90° compared to that of 0° specimen although the microstructure of 90° sample contained columnar grains of prior β phase parallel to tensile load direction (also parallel to building direction). On the other hand, the sample's ductility was close to that of 0° specimen.

As Carroll et al. [135] clarified, if samples contain defects such as lack of fusion, un-melted powders and gas voids, the results obtained from mechanical test can be opposite (0° samples may have higher strength). According to density measurement results, 90° sample had lower average density (contained higher porosity) (Table 4.1). The cross-sectional area under exposure of e-beam in this sample was comparatively lower so that the time of exposure of this cross-sectional area to high temperature was lower. Accordingly, lower tensile strength was obtained due to higher porosity although its underlying microstructure was finer than 0° specimen. Moreover, the surface roughness of the 0° sample was lower with respect to that of 90° sample (Figure 4.1). Therefore, possibility of failure at lower stress values in 90° sample was higher due to dominance of notch effect as well. On the other hand, both tensile strength and elongation values were the lowest in 45° sample since relative density of the specimen was lowest among all the specimens (Table 4.1).
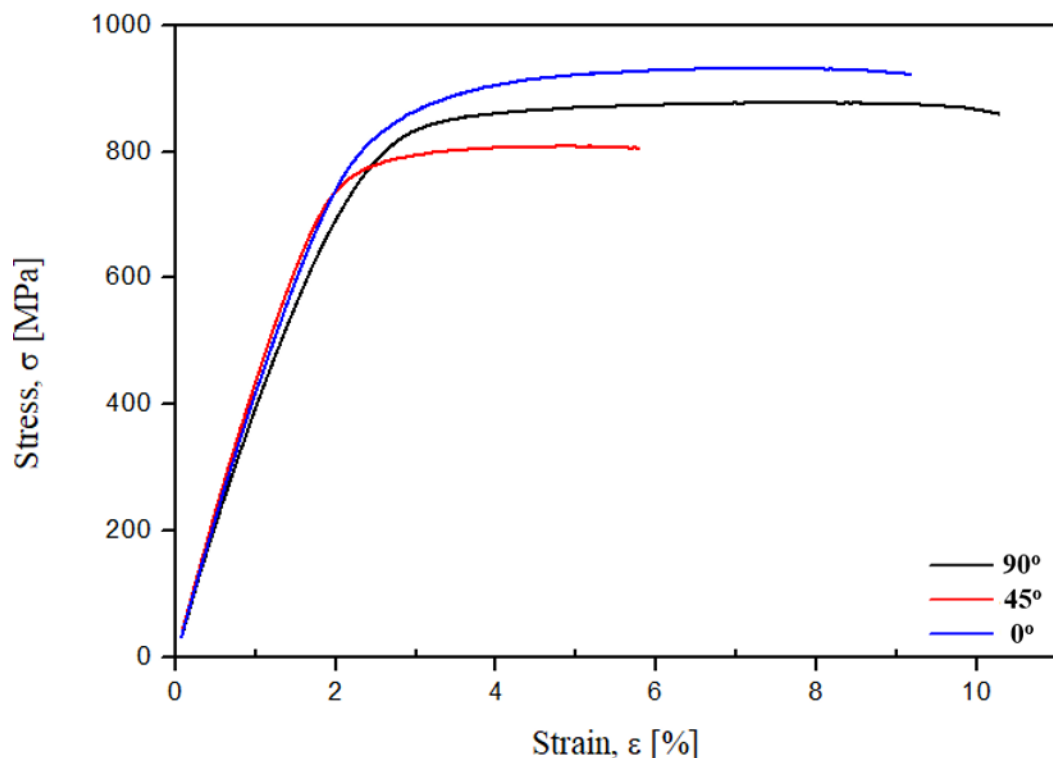
Figure 4.30. Stress-strain diagram of as-produced EBM samples at different angles; 90°, 45° and 0°.

Table 4.5. The average tensile test results of the as-produced specimens produced by EBM in different angles.

Sample	Ultimate Tensile Strength [MPa]	Strain at Fracture [%]
90° As-produced	878.0 ± 47.5	10.2 ± 1.6
45° As-produced	873.5 ± 118.7	5.7 ± 3.8
0° As-produced	925.5 ± 53.4	9.1 ± 1.0
ASTM F2924-14	895.0	10.0

The SEM images of the tensile test fracture surfaces of the specimens produced in different angles are shown in Figure 4.31. The information gathered from fracture surfaces was compatible with the average tensile test results presented in Table 4.5 such that there was direct correlation between mechanical properties and presence of defects, i.e. porosity and lack of fusion. According to SEM images, the 45° specimen had the largest amount of un-melted and unfused regions in the fracture surface, which resulted in larger void formation in central cross-section of the specimen and lower density. On the other hand, nearly no defects, like unfused regions and internal voids, were observed in the cross-section of 0° sample, which explains its higher strength and comparatively high elongation. 90° sample had also internal defects; however, relatively lower number of internal voids were observed compared to 45° sample. Therefore, the specimens' tensile properties were better with respect to 45° sample. According to tensile test results, it was concluded that the presence of defects in the samples was more critical than the fineness of the microstructure and the grain orientation when the mechanical properties are considered since defects (internal voids, surface roughness) play critical role during failure of the specimens. Therefore, scatter in the mechanical properties from sample to sample was attributed to the difference in size, distribution and locations of the defects. All of the samples displayed ductile fracture mode as revealed by equiaxed dimples on the fracture surfaces. The dimples on the fracture surface of the samples was observed to be different in size such that their size was directly dependent on the fineness of the microstructure. The size of the dimples was smallest in 90° specimen, which contained

finest lamellar structure made up of fine α and β phases (Figures 4.6 and 4.10). On the other hand, fracture surface of 0° specimen, which had the coarsest lamellar structure (Figures 4.6 and 4.10, was composed of coarse dimples. However, 45° specimen fracture surface was composed of dimples with size between those of 90° and 0° samples, which was again compatible with the fineness of the microstructure. Based on the dimple structures on the fracture surfaces, one can be expected highest strength in 90° specimen and highest ductility and lowest strength in 0° samples. However, there was no direct relationship between microstructure, dimple size and mechanical properties due to presence of different amounts of internal and external defects in the samples as discussed previously. For example, fracture surface of 45° specimen composed of internal voids in addition to dimples. Voids were also observed in 90° specimen: however, they rarely observed in fracture surface. On the other hand, nearly no voids were observed in the fracture surface of 0° specimen although it contained relatively coarse dimples. Therefore, 0° specimen possessed the highest strength with relatively high ductility.
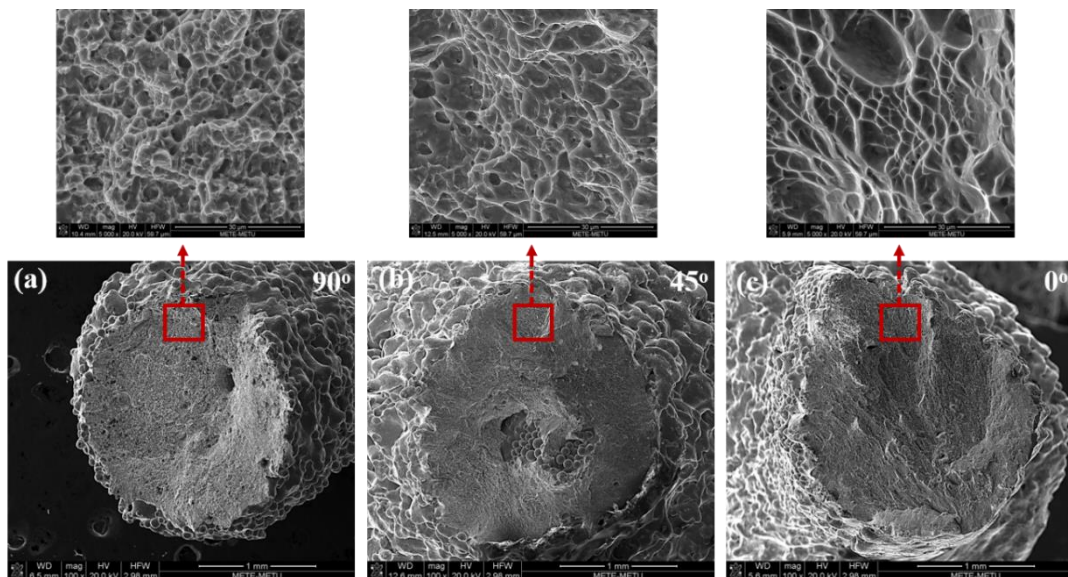
Figure 4.31. SEM images of the fracture surfaces of tensile test specimens produced in different angles; (a) 90°, (b) 45° and (c) 0°.

In addition to building direction, underlying microstructure and relieving of the residual stress in additively manufactured samples affect the mechanical properties. Therefore, the effect of thermo-hydrogen and annealing treatment on microstructure and mechanical properties were also investigated by keeping the building direction constant at 90º as well as the defect concentration constant. Similar to as-produced specimens, post-processed specimens' stress-strain curves (Figure 4.32) contained linear and strain hardening regions followed by ductile fracture subsequent to necking. Table 4.6 demonstrates the average tensile test results of the as-produced and heat treated (THP (hydrogenated + dehydrogenated) and conventional annealing) specimens produced by EBM at 90º. It was clear that THP increased average UTS value of the as-produced specimens up to 895.0 MPa and made the sample's UTS value compatible with the ASTM F2924-14 standard. Increase in the strength was also verified by relatively smaller dimples in fracture surface shown in Figure 4.33 (b) and finer underlying microstructure (Figures 4.18 and 4.19). However, about 25% reduction was observed in ductility level although THP treatment conducted at high temperature and acted also as a stress-relieving heat treatment. Decrease in the ductility level as a result of THP was attributed to slight oxidation of samples and microstructural refinement. When the average UTS results of the annealed specimen were investigated, UTS value were observed to decrease as it was expected due to microstructural coarsening (Figures 4.21 and 4.22); however, the ductility decreased although an increase was expected. Similar to THP treated samples, oxidation, which could occur during the heat treatments, was considered to be main reason for low ductility in annealed specimens.
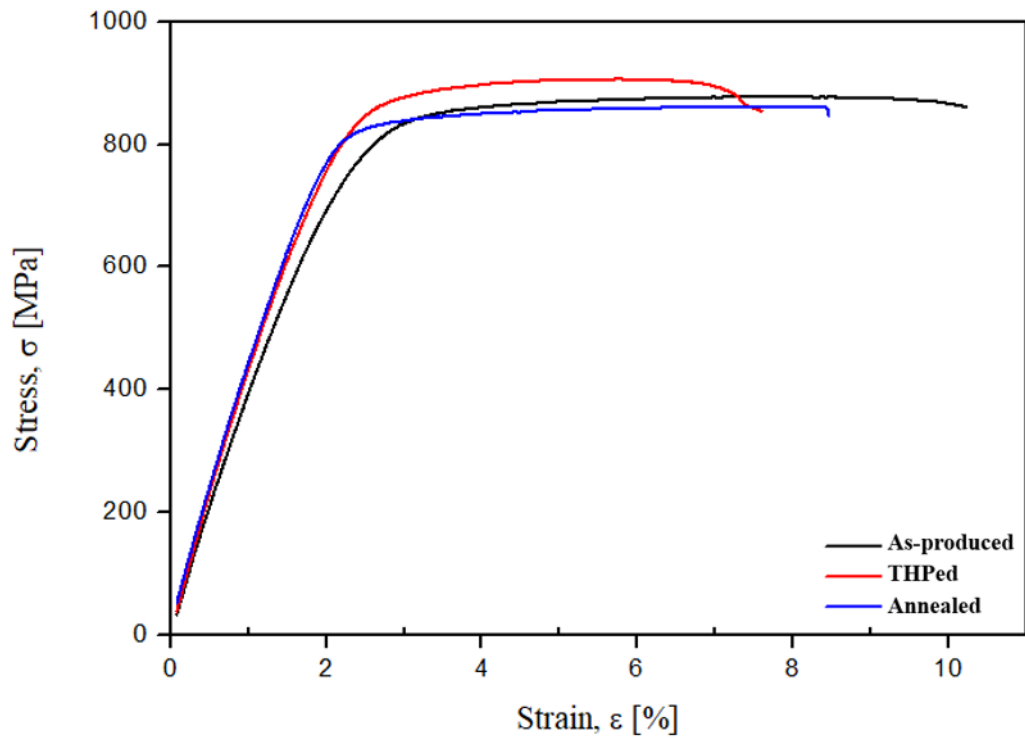
Figure 4.32. Stress-strain diagram of the as-produced and heat treated (THPed and annealed) specimens produced by EBM in 90º.

Table 4.6. The average tensile test results of the as-produced and heat treated specimens produced by EBM in 90º.

Sample	Ultimate Tensile Strength [MPa]	Strain at Fracture [%]
90º As-produced	878.0 ± 47.5	10.2 ± 1.6
90º THP	895.0 ± 21.2	7.6 ± 0.3
90º Annealed	862.0 ± 41.0	8.2 ± 0.3
ASTM F2924-14	895.0	10.0
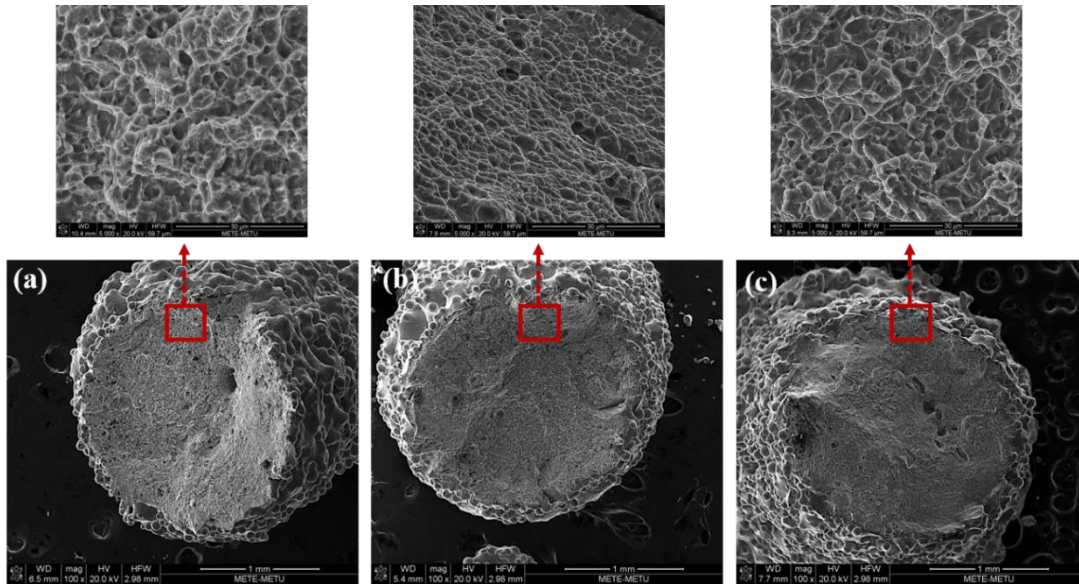
Figure 4.33. SEM images of the fracture surfaces of tensile test specimens produced in 90°; (a) as-produced, (b) post-THPed and (c) post-annealed.

4.6.2.2. Surface Polished Samples

In this part, the average tensile test results are given for the samples produced at 90°, which were chemically polished with 1% HF for 30 minutes in as-produced, THPed and annealed conditions (Figure 4.34 and Table 4.7). The main purpose was to decrease surface roughness, thereby, eliminating the notch effect caused by partially melted powders on the samples' surfaces. As can be seen in Figure 4.2, chemical polishing with HF acid solution reduced the surface roughness; however, mechanical properties were degraded. Although the same trend was observed in mechanical properties of post-processed specimens as in the case of untreated specimens, strength and ductility of all specimens (except THPed samples) decreased as a result of etching in HF acid solution. It is known that when titanium reacts with HF acid, Ti (III) fluoride and hydrogen gas is produced according to reaction 4.1.

$$Ti + 3HF \rightarrow TiF_3 + \frac{3}{2}H_2 \qquad (4.1)$$

112
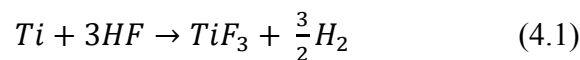
In addition to formation of hydrogen gas and TiF$_3$, higher concentrations of HF result in oxidation on the surface, which is white colored and difficult to remove [136]. Moreover, since titanium has high affinity for hydrogen, hydrogen can be absorbed in titanium when immersed in HF acid solutions for prolonged time. Therefore, hydrogen embrittlement may occur [137]. Accordingly, nitric acid should be added to reduce hydrogen absorption and hydrogen embrittlement. Therefore, lower ductility observed in samples after chemical polishing was attributed to dissolved hydrogen. Additionally, higher amount of defects (internal voids due to unfused powders) shown in Figure 4.35 was also thought to be another reason of lower strength and ductility. Powders used in the production of polished samples were the powders which were recycled 17 times. Because of the higher degree of oxidation of powders in each recycling stage, melting and fusion of powders became difficult when they were used after several recycling stages.
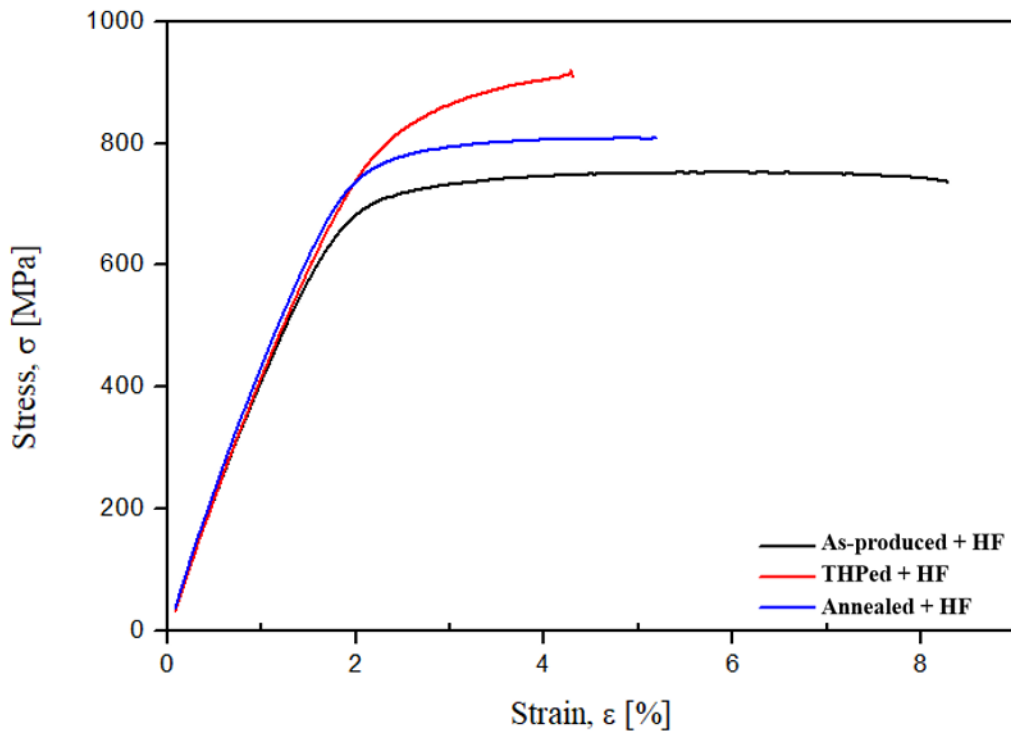
Figure 4.34. Stress-strain diagram of the as-produced and heat treated (THPed and annealed) specimens produced by EBM in 90° after chemically polished with HF.

Table 4.7. The average tensile test results of the chemically polished specimens in as-produced and heat treated conditions.

Sample	Ultimate Tensile Strength [MPa]	Strain at Fracture [%]
90º As-produced+ HF	779.4 $\pm$ 30.0	8.3 $\pm$ 4.5
90º THP + HF	945.1 $\pm$ 49.5	4.1 $\pm$ 1.6
90º Annealed + HF	804.4 $\pm$ 31.5	5.1 $\pm$ 1.0
ASTM F2924-14	895.0	10.0
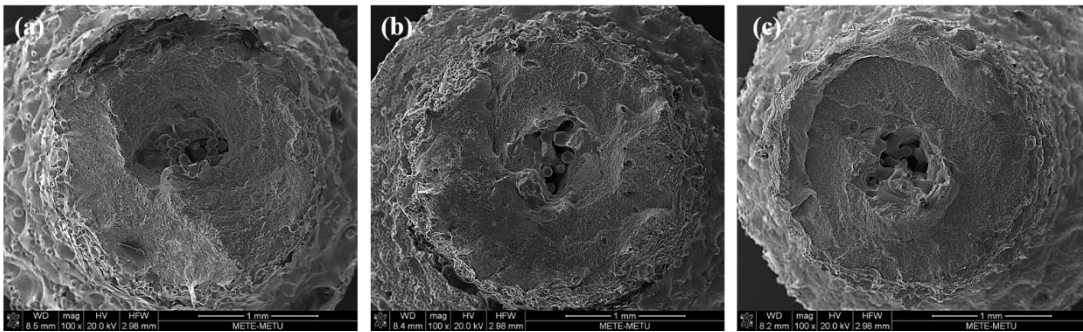
Figure 4.35. SEM images of the fracture surfaces of tensile test specimens produced in 90º chemically polished with 1% HF for 30 min; (a) as-produced, (b) THPed and (c) annealed.

4.6.3. Fatigue Tests

Specimens for rotating-bending fatigue tests were produced in dog-bone shape as shown in Figure 3.7 (b). The effects of building angle, surface polishing and post-heat treatment on fatigue life and strength were investigated. Unfortunately, since the specimens couldn't be produced in the same building batch, too much scatter was observed in fatigue data for the samples produced using the same variables.

4.6.3.1. Specimens Produced at Different Angles

The rotating bending fatigue test was initially carried out for the Ti-6Al-4V alloy specimens without polishing, which were produced by EBM in different angles (90º, 45º and 0º) and tested between the stress amplitudes approximately 170-350 MPa. S-N curves of the specimens are shown in Figure 4.36.

Unfortunately, the number of the specimens were quite low, therefore, only 1 or 2 samples for each group could be tested in the determined stress range, therefore, endurance limits couldn't be determined exactly. Among the specimens, 0º specimens had relatively higher fatigue life at any stress level compared to those produced at 90º and 45º. As previously mentioned, the specimens produced in three different angles had similar defects such as void and un-melted powders; however, defect density and surface roughness were different in each sample. Since the density of 0º specimens was the highest and their surface roughness was relatively lower (Table 4.1 and Figure 4.1), the highest fatigue life was obtained in these samples. Similar relationship between surface roughness, density and fatigue life was obtained for other samples. Fatigue life of the specimens produced at 90º was slightly higher than that of specimens produced at 45º in the same stress interval because of the higher density. It is known that the surface roughness of the samples is more effective on fatigue life and strength of the components compared to internal defects. For this reason, in similar works, the fatigue test is generally performed on the machined samples [89,97,138]. However, in this study, fatigue life was directly dependent on the surface roughness. Persenot et al. [138] reported fatigue life of the as-built Ti-6Al-4V alloy produced by EBM at three angles (90º, 45º and 0º), and the highest and lowest fatigue life belonged to those produced at 0º and 90º, respectively, which was directly related with the surface roughness of the samples. The fatigue life was found as 50000, 155000, and 250000 cycles for 90º, 45º and 0º, respectively, at a stress level 290 MPa, according to their study, and they found fatigue life of as-built 90º samples as 20000-25000 cycles at a stress level around 350 MPa. On the other hand, in our study, fatigue life was found as 26400, 22300, and 90500 cycles for as-produced samples at 90º, 45º and 0º, respectively, at a stress level 340 MPa. The fatigue life of the 90º samples was comparable that of found in the study of Persenot et al. [138]. Chastand et al. [89] found that fatigue life of the EBM produced Ti-6Al-4V alloy samples at 90º around 20000 and 40000 cycles for stress levels 400 MPa and 250 MPa, respectively.

In addition to these studies, recently, Chern et al. [97] reviewed that fatigue behavior of EBM produced Ti-6Al-4V alloy samples (90° and 0° angles) in different conditions such as as-built, HIPed, machined etc., and they concluded that as-built 0° samples had higher fatigue life compared to as-built 90° samples because of the higher surface roughness seen in the 90° samples. The fracture surfaces of the as-produced fatigue samples for three different angles are demonstrated in Figure 4.37. As can be seen, more than one crack initiation points were observed in all of the samples. However, 0° fatigue samples had relatively less crack initiation points, and uniform crack initiation regions compared to other angles. In general, rough surfaces consisting of partially sintered powders triggered the onset of fracture at different points in all samples. Similar to fracture surfaces of the tensile test samples, gas porosities and brittle fracture regions caused by inhomogeneous chemical composition or oxidation were observed on the fracture surfaces of the fatigue samples.
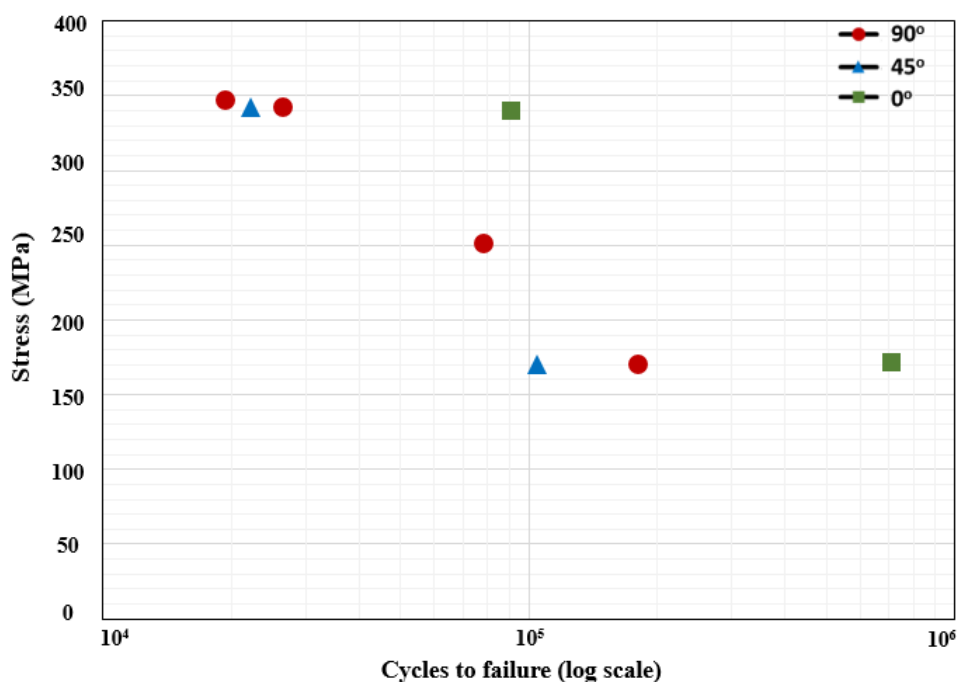
Figure 4.36. S-N curves of as-produced fatigue samples produced by EBM in different angles; 90°, 45°, and 0°.

116
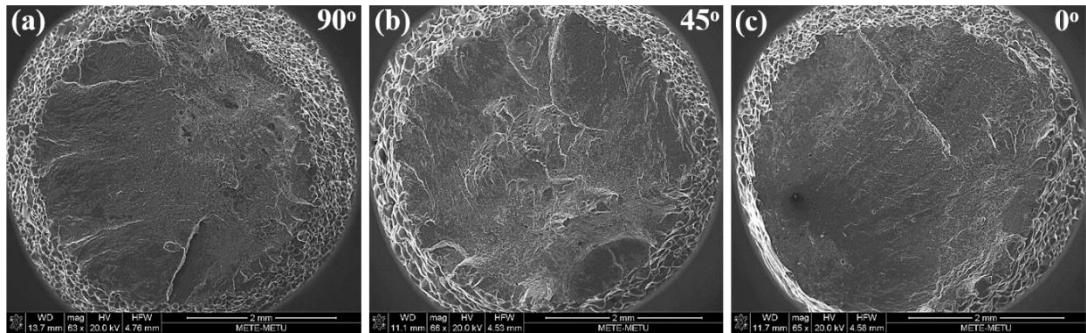
Figure 4.37. SEM images of the fracture surfaces of the as-produced fatigue specimens in (a) 90°, (b) 45° and (c) 0°.

4.6.3.2. Post-Processed and Surface Polished Specimens

In this part, the rotating bending fatigue test was applied to surface polished and unpolished samples of as-produced, THPed, annealed specimens by keeping the production angle at 90°. The S-N curves, which were obtained by testing the samples between the stress amplitudes of 85-350 MPa, are shown in Figure 4.38.

The same situation observed in tensile test samples were also detected in fatigue tests such that the effect of post-heat treatment on fatigue life couldn't be determined exactly due to presence of partially melted powders on the surface which acted as crack initiation points when samples exposed to cyclic loading. Therefore, as-produced samples, THP treated and annealed samples (without surface polishing) exhibited similar fatigue life, i.e. $\sim 2 \times 10^4$ cycles at 350 MPa and $\sim 1-2 \times 10^5$ cycles at 170 MPa.

On the other hand, chemical polishing applied with HF solution was observed to detrimental for fatigue strength and life in any type of sample although it reduced surface roughness. For example, the fatigue life measured at 70 MPa for post-annealed specimen was reduced from 2×10^5 cycles to 7×10^4 cycles. Similar tendency was also observed in all other samples as well. As previously discussed, polishing with HF acid solution may result in absorption of hydrogen in the sample which results in hydrogen embrittlement although HF treatment reduces the surface roughness.

117

As a result, the effects of THP and conventional annealing on the fatigue life of the polished and unpolished samples couldn't be detected since the surface roughness and the internal defects were the dominant factors during fatigue testing. Additionally, oxidation of the samples during heat treatments could reduce fatigue life, so the effects of microstructural changes on the fatigue life were not detected exactly. Figure 4.39 shows the fatigue fracture surfaces of the as-produced, THPed and annealed samples in chemically polished condition after they have been tested at 90 MPa and 170 MPa. Since there were too many external and internal defects in the samples, the effects of post-processing couldn't be determined precisely.

Therefore, samples may be machined to investigate the effect of post-processing on mechanical properties clearly. Moreover, the number of powder recycling should be decreased to increase the powder fusion and reduce internal defects.
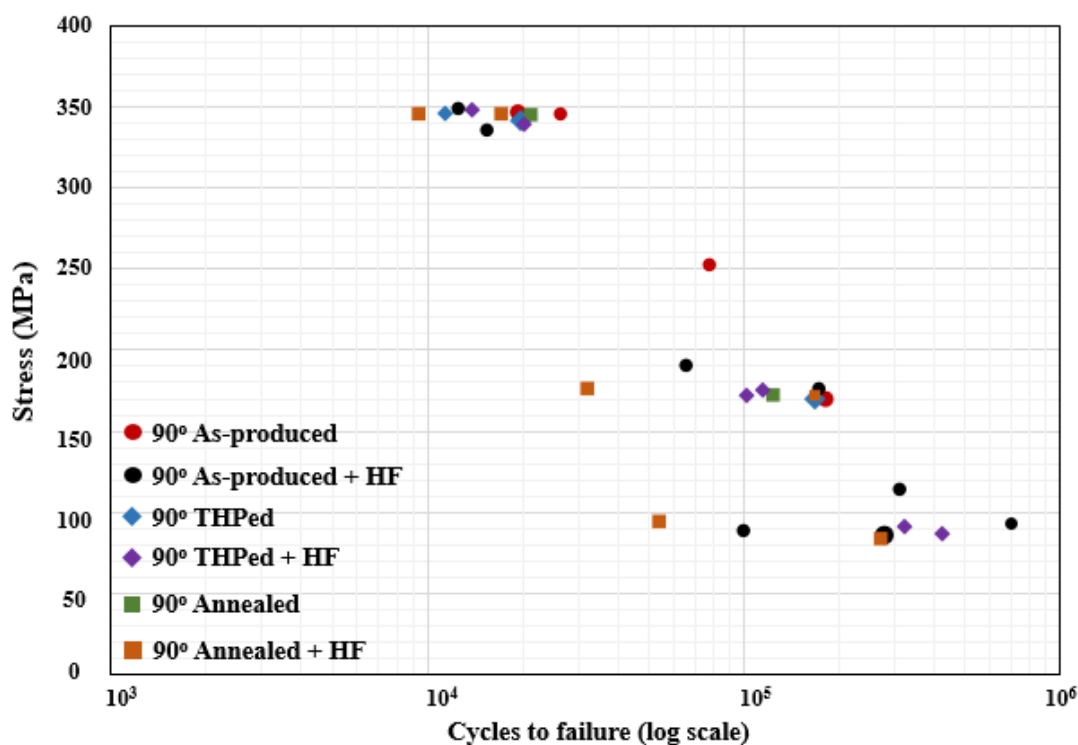
Figure 4.38. S-N curves for 90º fatigue samples produced by EBM; as-produced, as-produced and polished, THPed, THPed and polished, annealed, annealed and polished.

118
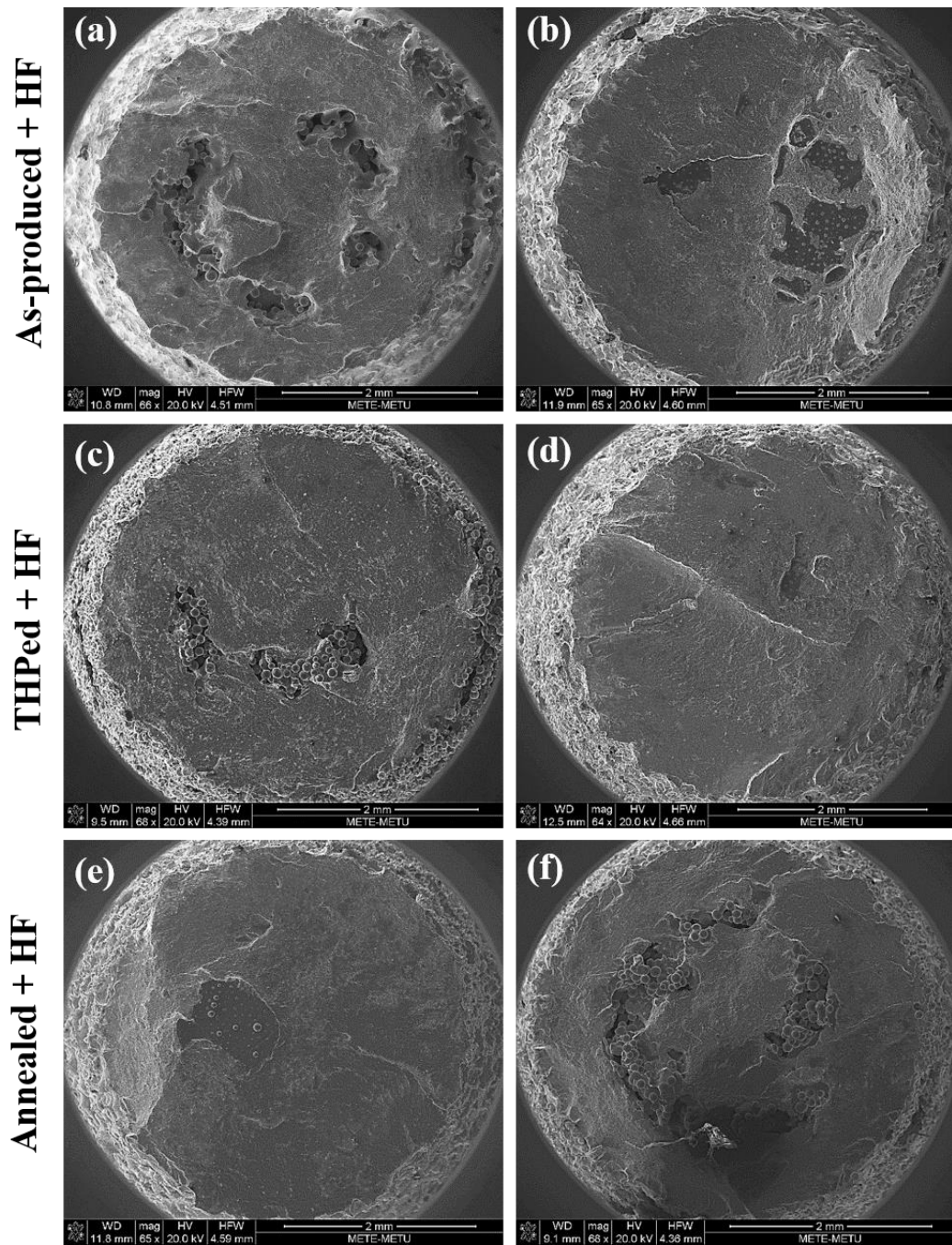
Figure 4.39. Representative SEM images of the fatigue fracture surfaces of samples (90º) after chemically polishing (a, c, e) 90 MPa and (b, d, f) 170 MPa.

CHAPTER 5

CONCLUSIONS

1. The relative densities of the EBM produced Ti-6Al-4V alloy parts were observed to be dependent on building direction. Highest relative density around 98.1% was obtained from the sample produced at 0°, while the samples produced at 45° possessed the lowest relative density around 97.8%. It was concluded that the relatively higher cross-sectional area under the exposure of e-beam enabled higher heat input in 0° samples, thereby, resulting higher density by nearly fully melting of powders.

2. The production angle was also effective on surface roughness. Samples produced at 90° had the highest surface roughness, while the lowest surface roughness was seen in the samples produced at 0° in which the heat input was higher.

3. It has been found that the number of samples at each batch and their relative positions along the z-axis (production direction) on building volume were also effective on the final density and microstructure. For example, higher number of samples in each batch increases the cooling rate and makes the microstructure finer. On the other hand, samples produced at top portion of the production volume had higher density but coarser microstructure because of higher heat input.

4. Microstructural examination revealed gas voids and un-melted powders both on the surface and interior parts of the samples. Gas voids were attributed to the evaporation of water, which occurred due to moisture present in starting

powders. On the other hand, there was partial melting and lack of fusion between the powders mainly due to the oxidation and agglomeration of the powders because of repeated recycling of powders.

5. Unlike SLM produced Ti-6Al-4V alloy samples with martensitic microstructures, EBM samples produced at any direction and position of the production volume contained lamellar Widmanstätten/basket-weave microstructure containing α plates and β laths in primary β-grains surrounded primary-α phase. Application of preheating by e-beam before each scan increased the layer temperature above martensite start temperature of the alloy and prevented martensitic transformation during cooling.

6. The primary-α phase, which is detrimental to mechanical properties, cannot be eliminated by EBM technique; however, the thickness of the phase may be decreased by lowering the preheating temperature.

7. Hydrogenated samples at 650 $^\circ$C for 1 h under high purity hydrogen atmosphere were observed to contain 1.97 wt.% hydrogen and δ (TiH$_2$) phase as revealed by XRD patterns. However, it was difficult to distinguish of δ-phase in optical or scanning electron microscope images.

8. Although there was still primary-α along the prior β-grain boundaries at the end of dehydrogenation process, the process enabled microstructural refinement by transformation of δ-phase to fine α-phase. At the end of the process, hydrogen contents of the samples decreased down to 0.0008 wt.%, lower than the maximum value defined by ASTM standard F2924-14.

9. Hydrogenation increased the hardness of the as-produced samples due to formation of harder δ-phase in α+β microstructure. Despite the hardness decrease observed as a result of subsequent dehydrogenation, hardness was

122

still higher than that of as-produced sample due to microstructural refinement. On the other hand, classical annealing heat treatment decreased the as-produced samples' hardness because of microstructural coarsening.

10. Samples produced at 0° displayed highest UTS and relatively high ductility around 926.0 MPa and 9.1 %, respectively. Tensile strengths of the samples produce at different angles were correlated with densities of samples. Therefore, lowest tensile strength and ductility values were observed in samples produced at 45°, which had lowest density and highest porosity inside. Additionally, surface roughness created by partially melted powders on the surfaces had influence on mechanical properties due to notch effect existed during tensile loading. For example, samples produced at 0° had the lowest surface roughness and thus, exhibited highest tensile strength.

11. THP increased the average UTS values of the as-produced specimens up to 895.0 MPa due to refinement of the microstructure. However, about 25% reduction was observed in ductility level, which was attributed to oxidation of samples slightly and microstructural refinement. As expected, annealing heat treatment decreased UTS values of as-produced samples due to coarsening effect. However, surface roughness was more effective on tensile properties than underlying microstructure created by different heat treatments. Because, the values obtained by different heat treatments were close to each other, therefore, the effect of different heat treatments on mechanical properties couldn't be determined precisely.

12. The rotating-bending fatigue test applied to samples produced at different angles (90°, 45° and 0°) revealed different fatigue life under the same stress. The sample produced at 0°, with low surface roughness and high density (with low defects), had the highest fatigue life. On the other hand, the effect of heat treatments (THP and annealing) on fatigue life couldn't be determined exactly

123

and the same number of cycles were obtained for each specimen. Therefore, the presence of defects and surfaces roughness were more dominant on fatigue life than different microstructures obtained by various heat treatments.

13. Although chemical polishing with 1% HF for 30 minutes reduced surface roughness by eliminating partially melted powders on the surface, fatigue life of the samples decreased surprisingly. Decrease in fatigue life was attributed to dissolution of hydrogen in samples due to prolonged immersion in HF solution.

14. Similar texture formation were observed in as-produced samples at different angles; the α phase texture was concentrated in $(10\bar{1}0)$ which was parallel to building direction and the other dominant texture component can be described as "Basal planes (0001) rotated 30 degrees around the building direction". Additional texture formation with low intensity was also observed between (0001) and $(2\bar{1}\bar{1}0)$ for the sample produced at 45º and 0º. Regardless of the building angle, the prior β phase texture was concentrated in (001) which is parallel to build or heat flow direction, and high temperature β phase transformed to α phase by fulfilling the Burger's relationship.

15. THP changed the texture of the as-produced Ti-6Al-4V alloy fabricated by EBM. α phase texture in THPed specimen was concentrated in (0001), which was parallel to building direction. Additional texture formation between (0001) and $(10\bar{1}0)$ were also observed in the same sample after THP. On the other hand, the α phase texture in annealed specimen was detected close to basal planes (0001) rotated 30 degrees around the building direction.

Future studies:

- Since EBM samples possess high surface roughness, chemical polishing procedures should be optimized to minimize surface roughness by minimization weight loss. Nitric acid may be added to HF solution to decrease hydrogen dissolution in the samples and prevent subsequent embrittlement. Additionally, machining can be applied to reduce surface roughness.

- In order to prevent formation of the primary α phase at the grain boundaries, preheating temperature in building chamber should be decreased and steps of THP should be modified.

- Crack propagation rates of the samples before and after THP should be investigated to understand the effect of microstructural refinement on fatigue properties of Ti-6Al-4V alloys.

- Transmission electron microscopy (TEM) should be used to understand microstructural refinement mechanism which is formed by δ to α phase transformation during THP.

REFERENCES

[1]   M. Peters, J. Hemptenmacher, J. Kumpfert, C. Leyens, Structure and Properties of Titanium and Titanium Alloys, 2003.

[2]   J. Karlsson, A. Snis, H. Engqvist, J. Lausmaa, Characterization and comparison of materials produced by Electron Beam Melting (EBM) of two different Ti-6Al-4V powder fractions, J. Mater. Process. Technol. 213 (2013) 2109–2118. doi:10.1016/j.jmatprotec.2013.06.010.

[3]   M. Peters, J. Kumpfert, C.H. Ward, C. Leyens, Titanium Alloys for Aerospace Applications, (2003) 333–350.

[4]   J. Breme, E. Eisenbarth, V. Biehl, Titanium and its Alloys for Medical Applications, Titan. Titan. Alloy. (2005) 423–451. doi:10.1002/3527602119.ch16.

[5]   K. Vanmeensel, K. Lietaert, B. Vrancken, S. Dadbakhsh, X. Li, J.-P. Kruth, P. Krakhmalev, I. Yadroitsev, J. Van Humbeeck, Additively manufactured metals for medical applications, in: Addit. Manuf., Elsevier Inc., 2018: pp. 261–309. doi:10.1016/b978-0-12-812155-9.00008-6.

[6]   G.C. Obasi, S. Birosca, J. Quinta Da Fonseca, M. Preuss, Effect of β grain growth on variant selection and texture memory effect during α → β → α phase transformation in Ti-6 Al-4 v, Acta Mater. 60 (2012) 1048–1058. doi:10.1016/j.actamat.2011.10.038.

[7]   R. Pederson, Microstructure and Phase Transformation of Ti-6Al-4V, 2002. doi:LTU-LIC-0230-SE.

[8]   H. Beladi, Q. Chao, G.S. Rohrer, Variant selection and intervariant crystallographic planes distribution in martensite in a Ti-6Al-4V alloy, Acta Mater. (2014). doi:10.1016/j.actamat.2014.06.064.

[9]   F. Froes, Titanium and titanium alloys, Kirk-Othmer Encycl. Chem. Technol. (1970) 1–30.

[10]   J.C. Williams, G. Lütjering, Titanium: Second Edition, (2007) 449. http://onlinelibrary.wiley.com/doi/10.1002/cbdv.200490137/abstract.

[11]   RTI, Titanium Alloy Guide, (2013) 43–74. www.smt.sandvik.com.

[12] M.J. Donachie, Titanium - A Techinacal Guide, 2000. doi:10.5772/1844.

[13] H.L. Freese, M.G. Volas, J.R. Wood, Metallurgy and Technological Properties of Titanium and Titanium Alloys, (2011) 25–51. doi:10.1007/978-3-642-56486-4_3.

[14] G. Terlinde, G. Fischer, O.F. Metallwerke, Beta Titanium Alloys, (2003).

[15] S. Materials, Standard Specification for Titanium-6Aluminum-4Vanadium Alloy Castings for Surgical, New York. (2004) 1–5. doi:10.1520/F1108-14.2.

[16] G. Lütjering, Influence of processing on microstructure and mechanical properties of (α+β) titanium alloys, Mater. Sci. Eng. A. 243 (2002) 32–45. doi:10.1016/s0921-5093(97)00778-8.

[17] M. Benedetti, V. Fontanari, The effect of bi-modal and lamellar microstructures of Ti-6Al-4V on the behaviour of fatigue cracks emanating from edge-notches, Fatigue Fract. Eng. Mater. Struct. (2004). doi:10.1111/j.1460-2695.2004.00825.x.

[18] C. Leyens, M. Peters, Titanium an Titanium Alloys, 2003. doi:10.1002/3527602119.

[19] F.J. Gil, M.P. Ginebra, J.M. Manero, J.A. Planell, Formation of α-Widmanstätten structure: Effects of grain size and cooling rate on the Widmanstätten morphologies and on the mechanical properties in Ti6Al4V alloy, J. Alloys Compd. 329 (2001) 142–152. doi:10.1016/S0925-8388(01)01571-7.

[20] J. Sieniawski, W. Ziaja, K. Kubiak, M. Motyk, Microstructure and Mechanical Properties of High Strength Two-Phase Titanium Alloys, in: Titan. Alloy. - Adv. Prop. Control, 2013. doi:10.5772/56197.

[21] X. Zhao, S. Li, M. Zhang, Y. Liu, T.B. Sercombe, S. Wang, Y. Hao, R. Yang, L.E. Murr, Comparison of the microstructures and mechanical properties of Ti-6Al-4V fabricated by selective laser melting and electron beam melting, Mater. Des. 95 (2016) 21–31. doi:10.1016/j.matdes.2015.12.135.

[22] Y. Fan, W. Tian, Y. Guo, Z. Sun, J. Xu, Relationships among the Microstructure, Mechanical Properties, and Fatigue Behavior in Thin Ti6Al4V, Adv. Mater. Sci. Eng. 2016 (2016). doi:10.1155/2016/7278267.

[23] J.C.M. Li, G. Lütjering, J.C. Williams, A. Gysler, Microstructure and Mechanical Properties of Titanium Alloys, in: Microstruct. Prop. Mater., 2000. doi:10.1142/9789812793959_0001.

[24] G. Lütjering, J.C. Williams, A. Gysler, Microstructure and Mechanical Properties of Titn, 2 (2000) 1–77.

[25] M. Peters, C. Leyens, Fabrication of Titanium Alloys, Titan. Titan. Alloy. (2005) 245–261. doi:10.1002/3527602119.ch8.

[26] H. Bikas, P. Stavropoulos, G. Chryssolouris, Additive manufacturing methods and modeling approaches: A critical review, Int. J. Adv. Manuf. Technol. 83 (2016) 389–405. doi:10.1007/s00170-015-7576-2.

[27] B. Wysocki, P. Maj, R. Sitek, J. Buhagiar, K. Kurzydłowski, W. Święszkowski, Laser and Electron Beam Additive Manufacturing Methods of Fabricating Titanium Bone Implants, Appl. Sci. 7 (2017) 657. doi:10.3390/app7070657.

[28] StandardTerminology for Additive Manufacturing Technologies, ASTM Stand. (n.d.) 1–3. doi:10.1520/F2792-12A.2.

[29] Y. Zhang, W. Jarosinski, Additive manufacturing processes and equipment, Elsevier Inc., 2018. doi:10.1016/B978-0-12-812155-9.00002-5.

[30] W.J. Sames, F.A. List, S. Pannala, R.R. Dehoff, S.S. Babu, The metallurgy and processing science of metal additive manufacturing, Int. Mater. Rev. (2016). doi:10.1080/09506608.2015.1116649.

[31] S. Liu, Y.C. Shin, Additive manufacturing of Ti6Al4V alloy: A review, Mater. Des. 164 (2019) 107552. doi:10.1016/j.matdes.2018.107552.

[32] W.E. Frazier, Metal additive manufacturing: A review, J. Mater. Eng. Perform. 23 (2014) 1917–1928. doi:10.1007/s11665-014-0958-z.

[33] M. Namatollahi, A. Jahadakbar, M.J. Mahtabi, M. Elahinia, Additive manufacturing (AM), 2nd ed., Elsevier Ltd., 2019. doi:10.1016/B978-0-08-102666-3.00012-2.

[34] D.C. Ackland, D. Robinson, M. Redhead, P.V.S. Lee, A. Moskaljuk, G. Dimitroulis, A personalized 3D-printed prosthetic joint replacement for the human temporomandibular joint: From implant design to implantation., J. Mech. Behav. Biomed. Mater. 69 (2017) 404–411. doi:10.1016/j.jmbbm.2017.01.048.

[35] R.K. Chen, Y. an Jin, J. Wensman, A. Shih, Additive manufacturing of custom orthoses and prostheses-A review, Addit. Manuf. 12 (2016) 77–89. doi:10.1016/j.addma.2016.04.002.

[36] T.D. Ngo, A. Kashani, G. Imbalzano, K.T.Q. Nguyen, D. Hui, Additive manufacturing (3D printing): A review of materials, methods, applications and challenges, Compos. Part B Eng. 143 (2018) 172–196. doi:10.1016/j.compositesb.2018.02.012.

[37] L. Jyothish Kumar, C.G. Krishnadas Nair, Current trends of additive manufacturing in the aerospace industry, in: Adv. 3D Print. Addit. Manuf. Technol., 2016. doi:10.1007/978-981-10-0812-2_4.

[38] M.M. Cotteleer, Mark, Jonathan Holdowsky, J. Coykendall, 3D opportunity in a erospace and defense, A Deloitte Ser. Addit. Manuf. (2014).

[39] Y. Bai, C.B. Williams, An exploration of binder jetting of copper, Rapid Prototyp. J. (2015). doi:10.1108/RPJ-12-2014-0180.

[40] A. Sova, S. Grigoriev, A. Okunkova, I. Smurov, Potential of cold gas dynamic spray as additive manufacturing technology, Int. J. Adv. Manuf. Technol. (2013). doi:10.1007/s00170-013-5166-8.

[41] D. Herzog, V. Seyda, E. Wycisk, C. Emmelmann, Additive manufacturing of metals, Acta Mater. (2016). doi:10.1016/j.actamat.2016.07.019.

[42] A.G. Demir, B. Previtali, Additive manufacturing of cardiovascular CoCr stents by selective laser melting, Mater. Des. (2017). doi:10.1016/j.matdes.2017.01.091.

[43] C. Brice, R. Shenoy, M. Kral, K. Buchannan, Precipitation behavior of aluminum alloy 2139 fabricated using additive manufacturing, Mater. Sci. Eng. A. (2015). doi:10.1016/j.msea.2015.08.088.

[44] S. Singh, S. Ramakrishna, R. Singh, Material issues in additive manufacturing: A review, J. Manuf. Process. 25 (2017) 185–200. doi:10.1016/j.jmapro.2016.11.006.

[45] M.L. Griffith, D.M. Keicher, C.L. Atwood, J.A. Romero, J.E. Smugeresky, L.D. Harwell, D.L. Greene, Free Form Fabrication of Metallic Components Using Laser Engineered Net Shaping (LENS^{TM}), Proc. 7th Solid Free. Fabr. Symp. Austin, TX. (1996). doi:10.4028/www.scientific.net/AMR.15-17.175.

[46] M. Zenou, L. Grainger, 3 - Additive manufacturing of metallic materials, in: Addit. Manuf., 2018. doi:https://doi.org/10.1016/B978-0-12-812155-9.00003-7.

[47] I. Gibson, D. Rosen, B. Stucker, Directed Energy Deposition Process: Additive Manufacturing Technologies, 2015. doi:10.2495/SDP-V9-N5-658-668.

[48] M.S. Domack, K.M. Taminger, M. Begley, Metallurgical Mechanisms Controlling Mechanical Properties of Aluminium Alloy 2219 Produced by Electron Beam Freeform Fabrication, Mater. Sci. Forum. (2009). doi:10.4028/www.scientific.net/msf.519-521.1291.

[49] R.P. Mudge, N.R. Wald, Laser engineered net shaping advances additive manufacturing and repair, Weld. Journal-New York-. (2007).

[50] W.. Hofmeister, D.. Nelson, C.. Robino, M.. Ensz, M.. Baldwin, L.. Harwell, M.. Schlienger, M. Essien, J.. Smugeresky, M.. Oliver, M.. Griffith, M.. Wert, J. Brooks, Understanding thermal behavior in the LENS process, Mater. Des. (1999).

[51] S. Bontha, N.W. Klingbeil, P.A. Kobryn, H.L. Fraser, Effects of process variables and size-scale on solidification microstructure in beam-based fabrication of bulky 3D structures, Mater. Sci. Eng. A. (2009). doi:10.1016/j.msea.2009.02.019.

[52] R. Banerjee, P.C. Collins, A. Genç, H.L. Fraser, Direct laser deposition of in situ Ti-6Al-4V-TiB composites, Mater. Sci. Eng. A. (2003). doi:10.1016/S0921-5093(03)00299-5.

[53] N. Shamsaei, A. Yadollahi, L. Bian, S.M. Thompson, An overview of Direct Laser Deposition for additive manufacturing; Part II: Mechanical behavior, process parameter optimization and control, Addit. Manuf. (2015). doi:10.1016/j.addma.2015.07.002.

[54] B. Utela, D. Storti, R. Anderson, M. Ganter, A review of process development steps for new material systems in three dimensional printing (3DP), J. Manuf. Process. (2008). doi:10.1016/j.jmapro.2009.03.002.

[55] X. Wu, A review of laser fabrication of metallic engineering components and of materials, Mater. Sci. Technol. (2007). doi:10.1179/174328407x179593.

[56]   S. Sun, M. Brandt, M. Easton, 2 - Powder bed fusion processes: An overview BT - Laser Additive Manufacturing, in: Woodhead Publ. Ser. Electron. Opt. Mater., 2017. doi:http://dx.doi.org/10.1016/B978-0-08-100433-3.00002-6.

[57]   W.S.W. Harun, N.S. Manam, M.S.I.N. Kamariah, S. Sharif, A.H. Zulkifly, I. Ahmad, H. Miura, A review of powdered additive manufacturing techniques for Ti-6al-4v biomedical applications, Powder Technol. 331 (2018) 74–97. doi:10.1016/j.powtec.2018.03.010.

[58]   Güney Mert BİLGİN, Optimization of the Mechanical Properties of Ti-6Al-4V Alloy Produced by Three Dimensional Additive Manufacturing Using Termochemical Processes, 2017.

[59]   M. Fousová, D. Vojtěch, K. Doubrava, M. Daniel, C.F. Lin, Influence of inherent surface and internal defects on mechanical properties of additively manufactured Ti6Al4V alloy: Comparison between selective laser melting and electron beam melting, Materials (Basel). 11 (2018). doi:10.3390/ma11040537.

[60]   H.K. Rafi, N. V. Karthik, H. Gong, T.L. Starr, B.E. Stucker, Microstructures and mechanical properties of Ti6Al4V parts fabricated by selective laser melting and electron beam melting, J. Mater. Eng. Perform. 22 (2013) 3872–3883. doi:10.1007/s11665-013-0658-0.

[61]   A. Safdar, H.Z. He, L.Y. Wei, A. Snis, L.E. Chavez De Paz, Effect of process parameters settings and thickness on surface roughness of EBM produced Ti-6Al-4V, Rapid Prototyp. J. 18 (2012) 401–408. doi:10.1108/13552541211250391.

[62]   A. Safdar, Microstructures and surface roughness of EBM produced Ti-6Al-4V, 2010.

[63]   J. Tong, C.R. Bowen, J. Persson, A. Plummer, Mechanical properties of titanium-based Ti–6Al–4V alloys manufactured by powder bed additive manufacture, Mater. Sci. Technol. (United Kingdom). 33 (2017) 138–148. doi:10.1080/02670836.2016.1172787.

[64]   Q.C. Liu, J. Elambasseril, S.J. Sun, M. Leary, M. Brandt, P.K. Sharp, The Effect of Manufacturing Defects on the Fatigue Behaviour of Ti-6Al-4V Specimens Fabricated Using Selective Laser Melting, Adv. Mater. Res. (2014). doi:10.4028/www.scientific.net/amr.891-892.1519.

[65] V. Manvatkar, A. De, T. DebRoy, Spatial variation of melt pool geometry, peak temperature and solidification parameters during laser assisted additive manufacturing process, Mater. Sci. Technol. (2014). doi:10.1179/1743284714y.0000000701.

[66] H. Gong, K. Rafi, H. Gu, G.D. Janaki Ram, T. Starr, B. Stucker, Influence of defects on mechanical properties of Ti-6Al-4V components produced by selective laser melting and electron beam melting, Mater. Des. 86 (2015) 545–554. doi:10.1016/j.matdes.2015.07.147.

[67] C. Cui, B.M. Hu, L. Zhao, S. Liu, Titanium alloy production technology, market prospects and industry development, Mater. Des. (2011). doi:10.1016/j.matdes.2010.09.011.

[68] R.R. Boyer, An overview on the use of titanium in the aerospace industry, Mater. Sci. Eng. A. (1996). doi:10.1016/0921-5093(96)10233-1.

[69] N.A. Waterman, P. Dickens, Rapid product development in the USA, Europe and Japan, World Cl. Des. to Manuf. (1994). doi:10.1108/09642369210056629.

[70] C. Emmelmann, P. Scheinemann, M. Munsch, V. Seyda, Laser additive manufacturing of modified implant surfaces with osseointegrative characteristics, in: Phys. Procedia, 2011. doi:10.1016/j.phpro.2011.03.048.

[71] J. Giannatsis, V. Dedoussis, Additive fabrication technologies applied to medicine and health care: A review, Int. J. Adv. Manuf. Technol. (2009). doi:10.1007/s00170-007-1308-1.

[72] L.E. Murr, S.M. Gaytan, Electron Beam Melting, in: Compr. Mater. Process., 2014. doi:10.1016/B978-0-08-096532-1.01004-9.

[73] Arcam EBM, (n.d.). http://www.arcam.com/wp-content/uploads/arcamebm-corp-brochure-fnlv3.pdf.

[74] Arcam AB, Electron Beam Melting - EBM Process, Additive Manufacturing | Arcam AB, ArcamEBM. (2017).

[75] C.K. Chua, K.F. Leong, C.S. Lim, Rapid prototyping: Principles and applications, third edition, 2010. doi:10.1142/6665.

[76]   D. Cormier, O. Harrysson, H. West, Characterization of H13 steel produced via electron beam melting, in: Rapid Prototyp. J., 2004. doi:10.1108/13552540410512516.

[77]   S.M. Gaytan, L.E. Murr, F. Medina, E. Martinez, M.I. Lopez, R.B. Wicker, Advanced metal powder based manufacturing of complex components by electron beam melting, Mater. Technol. 24 (2013) 180–190. doi:10.1179/106678509x12475882446133.

[78]   M. Galati, L. Iuliano, A literature review of powder-based electron beam melting focusing on numerical simulations, Addit. Manuf. 19 (2018) 1–20. doi:10.1016/j.addma.2017.11.001.

[79]   L.E. Murr, E. V. Esquivel, S.A. Quinones, S.M. Gaytan, M.I. Lopez, E.Y. Martinez, F. Medina, D.H. Hernandez, E. Martinez, J.L. Martinez, S.W. Stafford, D.K. Brown, T. Hoppe, W. Meyers, U. Lindhe, R.B. Wicker, Microstructures and mechanical properties of electron beam-rapid manufactured Ti-6Al-4V biomedical prototypes compared to wrought Ti-6Al-4V, Mater. Charact. (2009). doi:10.1016/j.matchar.2008.07.006.

[80]   L.E. Murr, Metallurgy of additive manufacturing: Examples from electron beam melting, Addit. Manuf. (2015). doi:10.1016/j.addma.2014.12.002.

[81]   L. Facchini, E. Magalini, P. Robotti, A. Molinari, Microstructure and mechanical properties of Ti-6Al-4V produced by electron beam melting of pre-alloyed powders, Rapid Prototyp. J. 15 (2009) 171–178. doi:10.1108/13552540910960262.

[82]   A.N. Kalinyuk, N.P. Trigub, V.N. Zamkov, O.M. Ivasishin, P.E. Markovsky, R. V. Teliovich, S.L. Semiatin, Microstructure, texture, and mehanical properties of electron-beam melted Ti-6Al-4V, Mater. Sci. Eng. A. (2003). doi:10.1016/S0921-5093(02)00518-X.

[83]   A. Safdar, L.Y. Wei, A. Snis, Z. Lai, Evaluation of microstructural development in electron beam melted Ti-6Al-4V, Mater. Charact. 65 (2012) 8–15. doi:10.1016/j.matchar.2011.12.008.

[84]   S. Requirements, M. Containing, L. Than, T. Percent, C. Titanium, Standard Specification for Additive Manufacturing Titanium-6 Aluminum-4 Vanadium with Powder Bed Fusion 1, i (2018) 1–9. doi:10.1520/F2924-14.2.

[85] B.E. Carroll, T.A. Palmer, A.M. Beese, Anisotropic tensile behavior of Ti-6Al-4V components fabricated with directed energy deposition additive manufacturing, Acta Mater. (2015). doi:10.1016/j.actamat.2014.12.054.

[86] S. Wolff, T. Lee, E. Faierson, K. Ehmann, J. Cao, Anisotropic properties of directed energy deposition (DED)-processed Ti–6Al–4V, J. Manuf. Process. (2016). doi:10.1016/j.jmapro.2016.06.020.

[87] P. Edwards, A. O'Conner, M. Ramulu, Electron Beam Additive Manufacturing of Titanium Components: Properties and Performance, J. Manuf. Sci. Eng. (2013). doi:10.1115/1.4025773.

[88] N. Hrabe, T. Quinn, Effects of processing on microstructure and mechanical properties of a titanium alloy (Ti-6Al-4V) fabricated using electron beam melting (EBM), Part 2: Energy input, orientation, and location, Mater. Sci. Eng. A. 573 (2013) 271–277. doi:10.1016/j.msea.2013.02.065.

[89] V. Chastand, P. Quaegebeur, W. Maia, E. Charkaluk, Comparative study of fatigue properties of Ti-6Al-4V specimens built by electron beam melting (EBM) and selective laser melting (SLM), Mater. Charact. 143 (2018) 76–81. doi:10.1016/j.matchar.2018.03.028.

[90] Y. Zhai, H. Galarraga, D.A. Lados, Microstructure Evolution, Tensile Properties, and Fatigue Damage Mechanisms in Ti-6Al-4V Alloys Fabricated by Two Additive Manufacturing Techniques, Procedia Eng. 114 (2015) 658–666. doi:10.1016/j.proeng.2015.08.007.

[91] M. Koike, P. Greer, K. Owen, G. Lilly, L.E. Murr, S.M. Gaytan, E. Martinez, T. Okabe, Evaluation of titanium alloys fabricated using rapid prototyping technologies-electron beam melting and laser beam melting, Materials (Basel). (2011). doi:10.3390/ma4101776.

[92] B.J. Hayes, B.W. Martin, B. Welk, S.J. Kuhr, T.K. Ales, D.A. Brice, I. Ghamarian, A.H. Baker, C. V. Haden, D.G. Harlow, H.L. Fraser, P.C. Collins, Predicting tensile properties of Ti-6Al-4V produced via directed energy deposition, Acta Mater. (2017). doi:10.1016/j.actamat.2017.05.025.

[93] C.Y. Yap, C.K. Chua, Z.L. Dong, Z.H. Liu, D.Q. Zhang, L.E. Loh, S.L. Sing, Review of selective laser melting: Materials and applications, Appl. Phys. Rev. (2015). doi:10.1063/1.4935926.

[94] G.M. Bilgin, Z. Esen, Ş.K. Akın, A.F. Dericioglu, Optimization of the mechanical properties of Ti-6Al-4V alloy fabricated by selective laser melting using thermohydrogen processes, Mater. Sci. Eng. A. 700 (2017) 574–582. doi:10.1016/j.msea.2017.06.016.

[95] G. Kasperovich, J. Hausmann, Improvement of fatigue resistance and ductility of TiAl6V4 processed by selective laser melting, J. Mater. Process. Technol. (2015). doi:10.1016/j.jmatprotec.2015.01.025.

[96] P. Edwards, M. Ramulu, Fatigue performance evaluation of selective laser melted Ti-6Al-4V, Mater. Sci. Eng. A. (2014). doi:10.1016/j.msea.2014.01.041.

[97] A.H. Chern, P. Nandwana, T. Yuan, M.M. Kirka, R.R. Dehoff, P.K. Liaw, C.E. Duty, A review on the fatigue behavior of Ti-6Al-4V fabricated by electron beam melting additive manufacturing, Int. J. Fatigue. 119 (2019) 173–184. doi:10.1016/j.ijfatigue.2018.09.022.

[98] N. Hrabe, T. Gnäupel-Herold, T. Quinn, Fatigue properties of a titanium alloy (Ti–6Al–4V) fabricated via electron beam melting (EBM): Effects of internal defects and residual stress, Int. J. Fatigue. 94 (2017) 202–210. doi:10.1016/j.ijfatigue.2016.04.022.

[99] H. Galarraga, D.A. Lados, R.R. Dehoff, M.M. Kirka, P. Nandwana, Effects of the microstructure and porosity on properties of Ti-6Al-4V ELI alloy fabricated by electron beam melting (EBM), Addit. Manuf. 10 (2016) 47–57. doi:10.1016/j.addma.2016.02.003.

[100] Y.C. Wu, C.N. Kuo, Y.C. Chung, C.H. Ng, J.C. Huang, Effects of electropolishing on mechanical properties and bio-corrosion of Ti6Al4V fabricated by electron beam melting additive manufacturing, Materials (Basel). (2019). doi:10.3390/ma12091466.

[101] S. Bagehorns, T. Mertens, D. Greitemeier, L. Carton, A. Schoberth, Surface finishing of additive manufactured Ti-6Al-4V - a comparison of electrochemical and mechanical treatments, Eucass 2015. (2015).

[102] G.A. Longhitano, M.A. Larosa, A.L.J. Munhoz, C.A. de C. Zavaglia, M.C.F. Ierardi, Surface Finishes for Ti-6Al-4V Alloy Produced by Direct Metal Laser Sintering, Mater. Res. 18 (2015) 838–842. doi:10.1590/1516-1439.014415.

[103] M. Qian, W. Xu, M. Brandt, H.P. Tang, Additive manufacturing and postprocessing of Ti-6Al-4V for superior mechanical properties, (2016). doi:10.1557/mrs.2016.215.

[104] B. Wysocki, J. Idaszek, K. Szlazak, K. Strzelczyk, T. Brynk, K.J. Kurzydłowski, W. Święszkowski, Post processing and biological evaluation of the titanium scaffolds for bone tissue engineering, Materials (Basel). 9 (2016). doi:10.3390/ma9030197.

[105] H. Galarraga, R.J. Warren, D.A. Lados, R.R. Dehoff, M.M. Kirka, P. Nandwana, Effects of heat treatments on microstructure and properties of Ti-6Al-4V ELI alloy fabricated by electron beam melting (EBM), Mater. Sci. Eng. A. 685 (2017) 417–428. doi:10.1016/j.msea.2017.01.019.

[106] O. Senkov, Thermohydrogen processing of titanium alloys, Int. J. Hydrogen Energy. 24 (1999) 565–576. doi:10.1016/s0360-3199(98)00112-8.

[107] Y. Zong, K. Wu, Thermo hydrogen treatment for microstructure refinement and mechanical properties improvement of Ti-6Al-4V alloy, Mater. Sci. Eng. A. 703 (2017) 430–437. doi:10.1016/j.msea.2017.07.076.

[108] F.H. Froes, O.N. Senkov, J.I. Qazi, Hydrogen as a temporary alloying element in titanium alloys: thermohydrogen processing, Int. Mater. Rev. 49 (2004) 227–245. doi:10.1179/095066004225010550.

[109] J.I. Qazi, O.N. Senkov, J. Rahim, A. Genc, F.H.S.A.M. Froes, Phase Transformations in Ti-6Al-4V − x H Alloys, 32 (2001) 2453–2463.

[110] D. Eliezer, T.H. Böllinghaus, Hydrogen effects in titanium alloys, in: Gaseous Hydrog. Embrittlement Mater. Energy Technol. Probl. Its Characterisation Eff. Part. Alloy Classes, 2012. doi:10.1533/9780857093899.3.668.

[111] A. San-Martin, F.D. Manchester, The H−Ti (Hydrogen-Titanium) system, Bull. Alloy Phase Diagrams. 8 (1987) 30–42. doi:10.1007/bf02868888.

[112] O.N. Senkov, J.J. Jonas, F.H. Froes, Recent advances in the thermohydrogen processing of titanium alloys, JOM. (1996). doi:10.1007/BF03222997.

[113] Y. Baoguo, W. Yujie, Z. Yubin, G. Longqing, Hydrogenation Behavior of Ti6Al4V Alloy, Rare Met. Mater. Eng. 46 (2017) 1486–1490. doi:10.1016/s1875-5372(17)30151-0.

[114] Y. Zhang, S.Q. Zhang, Hydrogenation characteristics of Ti6Al4V cast alloy and its microstructural modification by hydrogen treatment, Int. J. Hydrogen Energy. 22 (1997) 161–168. doi:10.1016/s0360-3199(96)00167-x.

[115] N. Pushilina, A. Panin, M. Syrtanov, E. Kashkarov, V. Kudiiarov, O. Perevalova, R. Laptev, A. Lider, A. Koptyug, Hydrogen-Induced Phase Transformation and Microstructure Evolution for Ti-6Al-4V Parts Produced by Electron Beam Melting, Metals (Basel). 8 (2018) 301. doi:10.3390/met8050301.

[116] J. W. Zhao, H. Ding, W. J. Zhao, X. F. Tian, H. L. Hou, Y. Q. Wang, Influence of hydrogenation on microstructures and microhardness of Ti6Al4V alloy, Trans. Nonferrous Met. Soc. China (English Ed. (2008). doi:10.1016/S1003-6326(08)60089-8.

[117] W.R. Kerr, The effect of hydrogen as a temporary alloying element on the microstructure and tensile properties of Ti-6Al-4V, Metall. Trans. A. (1985). doi:10.1007/BF02811677.

[118] A.A. Ilynn, B. Kolachev, A. Mamonov, Phase and structure transformations in titanium alloys under thermohydrogenous treatment, Titan. 92 Sci. Technol. 1 (1993) 941–947.

[119] T.Y. Fang, W.H. Wang, Microstructural features of thermochemical processing in a Ti-6Al-4V alloy, Mater. Chem. Phys. 56 (1998) 35–47. doi:10.1016/S0254-0584(98)00137-0.

[120] J. Zhao, H. Ding, Y. Zhong, C.S. Lee, Effect of thermo hydrogen treatment on lattice defects and microstructure refinement of Ti6Al4V alloy, Int. J. Hydrogen Energy. 35 (2010) 6448–6454. doi:10.1016/j.ijhydene.2010.03.109.

[121] A. Guitar, G. Vigna, M.I. Luppo, Microstructure and tensile properties after thermohydrogen processing of Ti-6Al-4V, J. Mech. Behav. Biomed. Mater. 2 (2009) 156–163. doi:10.1016/j.jmbbm.2008.06.002.

[122] D.B. Shan, Y.Y. Zong, Y. Lv, B. Guo, The effect of hydrogen on the strengthening and softening of Ti-6Al-4V alloy, Scr. Mater. (2008). doi:10.1016/j.scriptamat.2007.10.047.

[123] ASTM International, Astm F2924-14, Stand. Specif. Addit. Manuf. Titanium-6 Aluminum-4 Vanadium with Powder Bed Fusion. (2014). doi:10.1520.F2924.

138

[124] A.B. Spierings, M. Schneider, R. Eggenberger, Comparison of density measurement techniques for additive manufactured metallic parts, Rapid Prototyp. J. 17 (2011) 380–386. doi:10.1108/13552541111156504.

[125] J.A. Slotwinski, E.J. Garboczi, K.M. Hebenstreit, Porosity Measurements and Analysis for Metal Additive Manufacturing Process Control, J. Res. Natl. Inst. Stand. Technol. (2014). doi:10.6028/jres.119.019.

[126] S. Leuders, M. Thöne, A. Riemer, T. Niendorf, T. Tröster, H.A. Richard, H.J. Maier, On the mechanical behaviour of titanium alloy TiAl6V4 manufactured by selective laser melting: Fatigue resistance and crack growth performance, Int. J. Fatigue. (2013). doi:10.1016/j.ijfatigue.2012.11.011.

[127] H. Gong, K. Rafi, H. Gu, T. Starr, B. Stucker, Analysis of defect generation in Ti-6Al-4V parts made using powder bed fusion additive manufacturing processes, Addit. Manuf. 1 (2014) 87–98. doi:10.1016/j.addma.2014.08.002.

[128] X. Wang, K. Chou, EBSD study of beam speed effects on Ti-6Al-4V alloy by powder bed electron beam additive manufacturing, J. Alloys Compd. 748 (2018) 236–244. doi:10.1016/j.jallcom.2018.03.173.

[129] A.A. Antonysamy, J. Meyer, P.B. Prangnell, Effect of build geometry on the β-grain structure and texture in additive manufacture of Ti6Al4V by selective electron beam melting, Mater. Charact. 84 (2013) 153–168. doi:10.1016/j.matchar.2013.07.012.

[130] S.S. Al-Bermani, M.L. Blackmore, W. Zhang, I. Todd, The origin of microstructural diversity, texture, and mechanical properties in electron beam melted Ti-6Al-4V, Metall. Mater. Trans. A Phys. Metall. Mater. Sci. 41 (2010) 3422–3434. doi:10.1007/s11661-010-0397-x.

[131] C. de Formanoir, S. Michotte, O. Rigo, L. Germain, S. Godet, Electron beam melted Ti-6Al-4V: Microstructure, texture and mechanical behavior of the as-built and heat-treated material, Mater. Sci. Eng. A. 652 (2016) 105–119. doi:10.1016/j.msea.2015.11.052.

[132] S.L. Lu, H.P. Tang, S.M.L. Nai, Y.Y. Sun, P. Wang, J. Wei, M. Qian, Intensified texture in selective electron beam melted Ti-6Al-4V thin plates by hot isostatic pressing and its fundamental influence on tensile fracture and properties, Mater. Charact. 152 (2019) 162–168. doi:10.1016/j.matchar.2019.04.019.

[133] O. Engler, V. Randle, Introduction to Texture Analysis: Macrotexture, Microtexture and Orientation Mapping, 2010. doi:interface shear stre.

[134] Annealing Textures, Encycl. Mater. Sci. Technol. (2001) 318–322.

[135] B.E. Carroll, T.A. Palmer, A.M. Beese, Anisotropic tensile behavior of Ti-6Al-4V components fabricated with directed energy deposition additive manufacturing, Acta Mater. 87 (2015) 309–320. doi:10.1016/j.actamat.2014.12.054.

[136] A. V. Balyakin, A.N. Shvetcov, E.I. Zhuchenko, Chemical polishing of samples obtained by selective laser melting from titanium alloy Ti6Al4V, in: MATEC Web Conf., 2018. doi:10.1051/matecconf/201822401031.

[137] A. Labak, Alternatives to Hydrofluoric Acid Etching At Wyman Gordon Company, Worcester Polytechnic Institute, 2010.

[138] T. Persenot, A. Burr, G. Martin, J.Y. Buffiere, R. Dendievel, E. Maire, Effect of build orientation on the fatigue properties of as-built Electron Beam Melted Ti-6Al-4V alloy, Int. J. Fatigue. 118 (2019) 65–76. doi:10.1016/j.ijfatigue.2018.08.006.

CURRICULUM VITAE

PERSONAL INFORMATION

Surname, Name	: Doğu, Merve Nur
Nationality	: Turkish (TC)
Date and Place of Birth	: 11 March 1993, Ankara
Phone	: +90 505 698 5371
E-mail	: merve.dogu@metu.edu.tr

EDUCATION

Degree	Institution	Year of Graduation
BS	Materials Science and Engineering, Çankaya University, Ankara	2011
High School	Polatlı Anatolian High School, Ankara	2007

WORK EXPERIENCE

Year	Place	Enrollment
2017-Present	Atılım University	Research Assistant
2015 July	Tübitak MAM	Intern Engineering Student
2014 July	MKE Gazi Fişek Fabrikası	Intern Engineering Student

FOREIGN LANGUAGES

Upper-intermediate English.

CONGRESSES AND SYMPOSIUMS

1. Ziya Esen, Merve Nur Doğu, Güney Mert Bilgin, Arcan F. Dericioğlu, Designing thermochemical processes for Ti-alloys produced by additive manufacturing techniques, 4th Additive Manufacturing Congress, 11-14 April 2019, Antalya Turkey.

2. Merve Nur Doğu, Ziya Esen, Evren Tan, Berkay Gümüş, Arcan F. Dericioğlu, Production of Ti-6Al-4V Alloy by 3D Electron Beam Melting Technique and Development of Its Post Treatments, TMS 2019, 148th Annual Meeting & Exhibition March 10-14, 2019 • San Antonio, Texas, USA.

3. Merve Nur Doğu, Ziya Esen, Evren Tan, Berkay Gümüş, Arcan F. Dericioğlu, Property Development of EBM Processed Ti-6Al-4V Alloys through Hydrogen Treatments, 19th International Metallurgy and Materials Congress, 25-27 Oct. 2018, İstanbul Turkey.

4. Merve Nur Doğu, Güney Mert Bilgin, Ziya Esen, Evren Tan, Berkay Gümüş, Arcan F. Dericioğlu, Elektron Demeti ile Ergitme ve Seçmeli Lazer ile Ergitme Yöntemleri ile Üretilen Ti-6Al-4V Alaşımının Mekanik Özelliklerinin Termohidrojenleme İşlemiyle Optimize Edilmesi, Aselsan 3. Malzeme Teknolojileri Çalıştayı, 10-11 Mayıs 2018, Ankara Türkiye.

5. Ezgi Bütev, Aydın Albayrak, Hande Bircan, Merve Nur Doğu, Pelin Gündoğmuş, Buse Kahyaoğlu, Ziya Esen. "Structural and Functional Characterization of Surface Treated Biomedical Ti6al7nb Alloy Foams" PPM 2015 International Porous Powder Materials, 15-18 September 2015, Çeşme, İzmir, TURKEY.